Investigation and Design of Broadband and High-Output Power Uni-Traveling-Carrier Photodiodes

Peng Zhang

A Thesis
in
The Department
of
Electrical and Computer Engineering

Presented in Partial Fulfillment of the Requirements

For the Degree of Master of Applied Science at

Concordia University

Montréal, Québec, Canada

November 2014

© Peng Zhang, 2014

CONCORDIA UNIVERSITY
SCHOOL OF GRADUATE STUDIES

This is to certify that the thesis prepared

By: Peng Zhang

Entitled: "Investigation and Design of Broadband and High-Output Power Uni-Traveling-Carrier Photodiodes"

and submitted in partial fulfillment of the requirements for the degree of

Master of Applied Science

complies with the regulations of this University and meets the accepted standards with respect to originality and quality.

Signed by the final examining committee:

____ Chair
Dr. S. Hashtrudi Zad

____ Examiner, External
Dr. P. Bianucci (Physics) To the Program

____ Examiner
Dr. M. Kahrizi

____ Supervisor
Dr. X. Zhang

Approved by: ____
Dr. W. E. Lynch, Chair
Department of Electrical and Computer Engineering

____________20_____ ______________________________________
Dr. Amir Asif, Dean
Faculty of Engineering and Computer Science

Abstract

Investigation and Design of Broadband and High-Output Power Uni-Traveling-Carrier Photodiodes

Peng Zhang

Uni-traveling-carrier photodiode (UTC-PD) is very attractive for future fiber-optic systems, since it has exhibited high-speed and high-power performance. In this thesis, the bandwidth and saturation current of UTC-PD is investigated by using physics-based modeling. To further improve the performance, novel device structures are proposed.

On the one hand, a graded bandgap structure is employed in the absorption layer. It is shown that, similar to the effect of graded doping method, the electric field in the absorption layer is increased, and thus the bandwidth is improved. Moreover, both the graded doping and graded bandgap structure are optimized. It is found that, for the considered UTC-PD, combining use of the graded doping and graded bandgap in the absorption layer leads to an improvement of 39.4% in bandwidth.

On the other hand, linear doping profile and Gaussian doping profile are considered to be used in the collection layer. It is shown that, the distribution of electric field in the depletion region is improved, which leads to the better saturation performance. For the

considered UTC-PD, by using optimized linear doping profile and Gaussian doping profile, the improvement in saturation current is 18.7% and 25.8% respectively.

Additionally, two types of epitaxial structure have been grown. Both of them are predicted to exhibit excellent broadband and high-output power performance. The benefit of the proposed graded bandgap absorption layer is further verified. Moreover, the major steps of fabrication process flow are described.

Acknowledgements

I would like to express my sincere gratitude to my supervisor Dr. X. Zhang for his guidance, advice and financial support for me to finish this thesis.

I thank my colleagues in the iPhotonics research group: especially to Dr. R. Zhang, Jie Xu and Jing Zhang, for many fruitful discussions regarding the investigations described in the thesis.

Last, but not least, I am very grateful to my parents and my girlfriend for their love and support.

Table of Contents

List of Figures x

List of Tables xvi

Chapter 1 Introduction 1

1.1 Introduction 1

1.2 Figures of merit 7

1.2.1 Bandwidth 7

1.2.2 Output RF power 10

1.3 Motivation of this research 11

1.3.1 Literature review 11

1.3.2 Motivation 13

1.4 Thesis organisation 13

Chapter 2 Physics-Based UTC-PD Modeling 15

2.1 Device structure 17

2.2 Definition of material parameters and models 19

2.2.1 Energy gaps and heterojunction band offsets setting 20

2.2.2 Defining optical properties of materials 25

2.2.3 The energy balance transport model 27

2.2.4 Mobility models....................29
2.2.4.1 Concentration dependent mobility model....................29
2.2.4.2 Parallel electric field dependent mobility model....................30
2.2.4.3 Energy dependent mobility model....................32
2.2.5 Recombination models....................33
2.2.5.1 Shockley-Read-Hall (SRH) concentration dependent lifetime model....................34
2.2.5.2 Standard Auger model....................37
2.3 Basic equations....................37
2.3.1 Poisson's equation....................38
2.3.2 Carrier continuity equations....................39
2.3.3 The transport equations....................39
2.4 Physical modeling verification....................40
2.5 Summary....................42
Chapter 3 Graded Absorption Layer Design....................43
3.1 Investigation of graded doping effects in absorption layer....................44
3.2 Design of graded bandgap absorption layer structure....................46
3.3 Optimization of graded structure....................51

3.3.1 Optimization of graded doping structure..55

3.3.2 Optimization of graded bandgap structure 59

3.4 Combined graded absorption layer structure 63

3.5 Summary 65

Chapter 4 Investigation and Design of Collection Layer Doping Profile......................67

4.1 Space-charge effect in UTC-PDs 68

4.2 Charge compensation by using uniform doping profile in the collector..............72

4.3 Design of collection layer based on linear doping profile 77

4.3.1 Linearly doped collection layer design...78

4.3.2 Optimization of linearly doped collection layer 82

4.4 Design of collection layer based on Gaussian doping profile 87

4.5 Discussion and summary...97

Chapter 5 Design and Fabrication of High-Speed and High-Power UTC-PDs...........101

5.1 Device structure..101

5.2 Device characterization 105

5.3 Device fabrication 107

5.3.1 P-type contact metalization 108

5.3.2 P-mesa formation...110

5.3.3 N-type contact metalization..112

5.3.4 N-mesa formation 114

5.3.5 Mesa passivation and via hole opening 115

5.3.6 Planarization and via hole opening...118

5.3.7 Deposition of GSG contact pads 121

5.4 Summary 123

Chapter 6 Conclusions and Future Work...124

6.1 Conclusions 124

6.2 Future work 127

References..128

List of Figures

Figure 1.1 Band diagram of pin-PD [3]. 2

Figure 1.2 (a) Band diagram of UTC-PD [3], (b) schematic of the epi-structure of UTC-PD. 5

Figure 2.1 Conduction and valence band offsets for heterojunctions presented in UTC-PD and used in the numerical modeling. 24

Figure 2.2 Real and imaginary parts of the refractive index for InGaAs versus .. 27

Figure 2.3 Electron velocity field characteristics for InGaAs, GaAs and InP [40]. 30

Figure 2.4 Electron lifetime in p-type InGaAs as a function of doping concentration. The solid line is calculated by using Conklin's empirical model [43]. The dashed line is the fitting result of CONSRH model. 36

Figure 2.5 Simulated modulation response of device with active area of 20 and 80 μm^2 at -2 V bias voltage and the reported bandwidth in [6] and [31]. 41

Figure 3.1 Distribution of electric field in the absorption layer of PD_{80} with uniformly and linearly doped absorption layer. 45

Figure 3.2 Simulated modulation response for PD_{80} with uniformly and linearly doped absorption layer. 46

Figure 3.3 Band diagram of the absorption layer of PD_{80} with original design [6] and with graded bandgap design. 49

Figure 3.4 Distribution of electric field in the absorption layer of PD_{80} with original design [6] and with graded bandgap design..49

Figure 3.5 Simulated modulation response for PD_{80} with original design [6] and with graded bandgap design. 50

Figure 3.6 Schematic diagram of the graded structure optimization method. The left side is the blocking layer side. 55

Figure 3.7 Simulated 3-dB bandwidth versus W_{GD}. 58

Figure 3.8 Distribution of electric field in the absorption layer versus depth for the four cases marked in Fig. 3.7. 58

Figure 3.9 Band diagram of the absorption layer versus depth for the four cases.59

Figure 3.10 Simulated 3-dB bandwidth versus W_{GB}..62

Figure 3.11 Distribution of electric field in the absorption layer versus depth for the four cases marked in Fig. 3.10. 62

Figure 3.12 Band diagram of the absorption layer versus depth for the four cases. 63

Figure 3.13 Distribution of electric field in the absorption layer for PD_{80} with different absorption layer structure. 64

Figure 3.14 Simulated modulation response of PD_{80} with different absorption layer structure. 65

Figure 4.1 Electron concentration profiles of PD_{80} at various light intensity levels. 70

Figure 4.2 Distribution of electric field in the depletion region of PD_{80} at various light intensity levels. 71

Figure 4.3 Band diagram of PD_{80} at various light intensity levels. 71

Figure 4.4 Simulated DC photocurrent versus light intensity for PD_{80} at various collector doping levels. 75

Figure 4.5 Distribution of electric field in the depletion region of PD_{80} at various collector doping levels without light injection. 75

Figure 4.6 Distribution of electric field in the depletion region of PD_{80} at various collector doping levels under $2x10^6$ W/cm^2 light injection. 76

Figure 4.7 Band diagram of PD_{80} at various collector doping levels. 76

Figure 4.8 Simulated 3-dB bandwidth versus photocurrent for PD_{80} with different uniform doping level in the collection layer. 77

Figure 4.9 Distribution of electric field in the depletion region of the device with different collection layer structure under $2x10^6$ W/cm^2 light injection. Inset is the enlarged view at the input end of collector. 81

Figure 4.10 Electron concentration profiles in the absorption layer for the device with different collection layer structure under $2.4x10^6$ W/cm^2 light injection. .81

Figure 4.11 Simulated DC photocurrent versus light intensity for the device with different collection layer structure. 82

Figure 4.12 Schematic diagram of the linear doping profile optimization method. The left side is the cliff layer side. 85

Figure 4.13 Simulated DC saturation current versus W_{CD} / W_C at D=$2x10^{16}$ cm^{-3}. 86

Figure 4.14 Distribution of electric field at the input end of collector under $2x10^6$ W/cm^2 light intensity for the four cases marked in Fig. 4.13. 86

Figure 4.15 Simulated DC saturation current versus the depth location of the peak doping at Y.CHAR=0.05 μm and D=$2x10^{16}$ cm^{-3}. 92

Figure 4.16 Gaussian doping profile in the collection layer for the cases marked in Fig. 4.15..92

Figure 4.17 Distribution of electric field at the input end of collector under $2x10^6$ W/cm^2 light intensity for the three cases marked in Fig. 4.15. 93

Figure 4.18 Simulated DC saturation current versus Y.CHAR at PEAK = 0.39 µm 95

Figure 4.19 Gaussian doping profile in the collection layer for the cases marked in Fig. 4.18..96

Figure 4.20 Distribution of electric field at the input end of collector under $2x10^6$ W/cm^2 light intensity for the three cases marked in Fig. 4.18. 96

Figure 4.21 Different doping profile in the collection layer. Noted: the y-axis scale is log10. 99

Figure 4.22 Distribution of electric field near the input end of collector under $2x10^6$ W/cm^2 light intensity for PD_{80} with different collector doping profile. 99

Figure 4.23 Simulated DC photocurrent versus light intensity for PD_{80} with different collector doping profile. 100

Figure 5.1 Simulated modulation response of PD_A and PD_B. 106

Figure 5.2 Distribution of electric field in the absorption layer of PD_A and PD_B. 106

Figure 5.3 Simulated DC photocurrent versus light intensity of PD_A and PD_B.. 107

Figure 5.4 (a) Schematic diagram of the wafer after p-type contact metalization, (b) the cross-sectional view. 110

Figure 5.5 (a) Schematic diagram of the wafer after p-mesa formation, (b) the cross-sectional view. 112

Figure 5.6 (a) Schematic diagram of the wafer after n-type contact metalization, (b) the cross-sectional view. 113

Figure 5.7 (a) Schematic diagram of the wafer after n-mesa formation, (b) the cross-sectional view. 115

Figure 5.8 (a) Schematic diagram of the wafer after passivation, (b) the cross-sectional view. 117

Figure 5.9 (a) Schematic diagram of the wafer after planarization, (b) the cross-sectional view. 121

Figure 5.10 (a) Schematic diagram of finished device, (b) the cross-sectional view. 122

Figure 5.11 Suggested device dimensions. 123

List of Tables

Table 2.1 Epitaxial layers of the UTC-PD reported in [6]. 19

Table 4.1 N.PEAK at various values of PEAK, when Y.CHAR=0.05 µm. 90

Table 4.2 N.PEAK at various values of Y.CHAR, when PEAK=0.39 µm. 94

Table 5.1 Epitaxial layers of PD_A. 104

Table 5.2 Epitaxial layers of PD_B...104

Chapter 1 Introduction

1.1 Introduction

In recent years, research on exploring broadband and high-efficiency fiber-optic communication systems and wireless communications has been increasing. Photodiodes (PDs), which convert broadband optical signal to electrical signal with high-efficiency, serve as the key components in these systems. They can be employed in a digital optical front end to provide a distortion-free electrical output signal [1]; and also used to generate millimeter and sub-millimeter waves for RF transmitters [2]. For practical applications, PDs with large bandwidth and high output current are desired.

Various types of PD structures have been developed to achieve broad bandwidth and high output power. Among them, pin-PD is widely used, because it has simple structure and relatively high responsivity. Band diagram of the pin-PD is schematically shown in Fig. 1.1 [3]. It consists of a lightly doped intrinsic region, sandwiched between highly doped n+ and p+ regions. The intrinsic region is much wider than the n+ and p+ regions to absorb large number of photons and to achieve high quantum efficiency. Electron-hole pairs are generated in the intrinsic region. At operation bias voltage, the intrinsic region is entirely depleted, and thus the electric field in this region is high. Then, the generated

electron-hole pairs can be quickly separated by the electric field and drift towards the n and p contacts respectively, as illustrated in Fig. 1.1 [3]. At proper electric field, the carriers can drift at their saturation velocity to across the absorption layer, which leads to minimum carrier transit time. Moreover, in the linearity range of pin-PD, the output photocurrent is proportional to the optical intensity and electron-hole pairs generation rate.

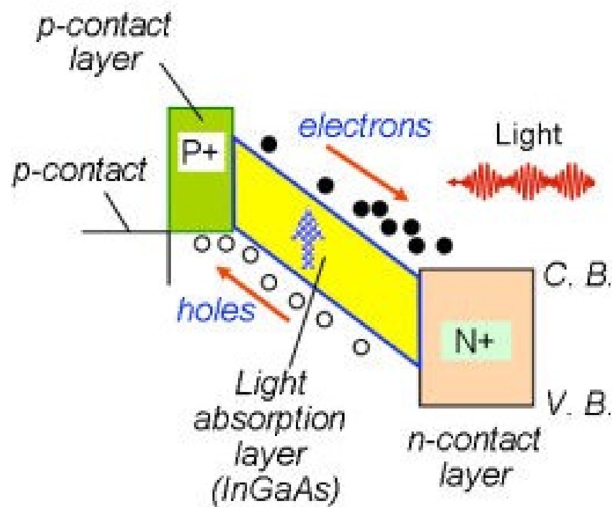

Figure 1.1 Band diagram of pin-PD [3].

However, the bandwidth and output current performance of pin-PD are limited. On the one hand, this structure leads to several constraints on bandwidth performance. The bandwidth of pin-PD is determined by the carrier transit time and RC-time constant. The 3-dB frequency f_{3dB} can be expressed as [4]

$$\frac{1}{f_{3dB}^2} = \frac{1}{f_{tr}^2} + \frac{1}{f_{RC}^2}, \tag{1.1}$$

in which, f_{tr} is the transit time limited bandwidth, f_{RC} is the RC-time constant limited bandwidth. They are given by [4]

$$f_{tr} = \frac{3.5v}{2\pi d}, \quad \frac{1}{v^4} = \frac{1}{2}\left(\frac{1}{v_e^4} + \frac{1}{v_h^4}\right), \tag{1.2}$$

$$f_{RC} = \frac{1}{2\pi R_{tot} C_{pd}} = \frac{d}{2\pi (R_S + R_L)\varepsilon A}. \tag{1.3}$$

Here, v is the average carrier drift velocity of electron velocity v_e and hole velocity v_h, d is the intrinsic region thickness, R_{tot} is the total resistance including series resistance R_S and load resistance R_L, and C_{pd} is the junction capacitance which is related to the permittivity ε of the depletion region, the active region area A and the intrinsic region thickness. According to Eq. (1.2), we can see that, for pin-PD, the transit time bandwidth is mainly limited by the hole velocity, since the hole velocity is much lower than that of electron. The transit time can be reduced by decreasing the intrinsic region thickness d. However, according to Eq. (1.3), shorter d results in lower RC-time constant limited bandwidth. Moreover, the efficiency drops with shorter intrinsic region thickness. On the other hand, pin-PD is hard to operate at high optical injection level, and thus limiting the output current. This is mainly due to the space-charge effect [5]. Since electrons drift faster than holes, under high illumination power, holes accumulate in the depleted intrinsic region near the i-n interface. The accumulated space charge results in the

degradation of the electric field near the n-contact layer side. Thus, as the electric field decreases, the carrier velocity drops which leads to lower bandwidth and the output current saturation.

In order to reduce the constraints to improve the bandwidth and saturation performance, a modified structure, which is referred to UTC-PD, is demonstrated by T. Ishibashi et al. [6]-[9]. The band diagram of the UTC-PD is shown in Fig. 1.2 (a) [3], and the schematic of its epi-structure is illustrated in Fig. 1.2 (b). Different from the intrinsic absorption depletion region for the conventional pin-PD, for UTC-PD, the light absorption region and the depleted collection region are separated. UTC-PD employs a thicker p-type highly doped narrow bandgap InGaAs layer as the light absorption layer and utilizes an undoped (or lightly n-type doped) wide bandgap InP layer instead of the intrinsic layer. Since the energy gap of the InP is larger than the photon energy, it is transparent to the incident light. Thus, the electron-hole pairs are only generated in the heavily p-doped InGaAs absorption layer. Moreover, since the holes are the majority carriers in the absorption layer, the photogenerated holes respond in a very fast dielectric relaxation time. Therefore, for UTC-PD, the role of holes as the active carriers is eliminated, and thus only the transportation of the photogenerated high speed electrons determines the device performance. This is a crucial difference from the conventional

pin-PD. This feature leads to significant improvement in bandwidth and saturation performance.

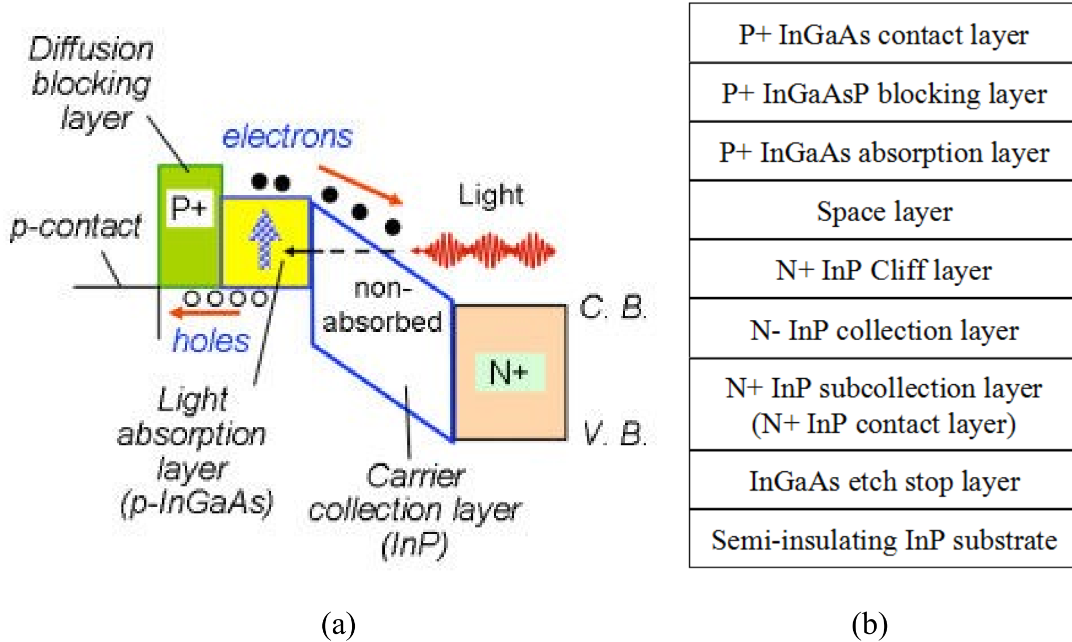

Figure 1.2 (a) Band diagram of UTC-PD [3], (b) schematic of the epi-structure of UTC-PD.

On the one hand, UTC-PD provides higher operation speed than pin-PD. The advantages can be seen from both the bandwidth limitation factors, namely the carrier transit time and RC-time constant, which have been mentioned above. Obviously, the carrier traveling time in the depletion layer is considerably reduced. Because it has been observed experimentally that the electron can move at overshoot velocity in the InP collection layer of UTC-PD, which is much higher than the saturation velocity of holes in the pin-PD. Moreover, for a typical UTC-PD structure, since the electron diffusion velocity is considered to be smaller than its drift velocity, the total transit time is mainly

determined by the electron diffusion time in the absorption layer. Due to the high mobility of minority electrons in p-type InGaAs, the electrons diffusion velocity in the UTC-PD can be higher than the hole saturation velocity in the pin-PD [6]. Accordingly, the carrier transit time is improved by using UTC-PD structure. In addition, for UTC-PD, the absorption layer and collection layer are independent of each other. Thus, the thickness of absorption layer can be shrinked to reduce the carrier transit time without increasing the RC-time constant. While, for pin-PD, although thinner absorption layer leads to shorter carrier transit time, the RC-time constant becomes larger. This trade-off limits the bandwidth performance of pin-PD.

On the other hand, since only the high speed electrons transport in depletion region of the UTC-PD, the space charge effect is significantly suppressed, and thus the saturation performance is improved. The space charge effect in UTC-PD is different from the situation in pin-PD. For UTC-PD, at high optical power, the photo-generated electrons starts to accumulate at the output side of absorption layer. This leads to the electric field drops at the input side of collection layer. When this field becomes lower than a critical value, the electron velocity is considerably reduced, which results in saturation. For pin-PD, saturation is caused by the accumulated holes in the depleted intrinsic region. The reduction of electrons velocity occurs at a relatively low electric

field, while the reduction of holes velocity occurs at a relatively high electric field. Therefore, the output for the UTC-PD does not saturate until the electric field in the depletion region becomes much lower than that for the pin-PD. This implies that UTC-PD can be operated at higher optical injection level, and thus higher output current can be achieved.

1.2 Figures of merit

There are several figures of merit to assess the performance of PDs, such as bandwidth, saturation current, RF power, responsivity and quantum efficiency. For different applications, different evaluation criteria are required. For the applications in fiber-optic communication systems, broad bandwidth and high output power photodiodes are necessary. The UTC-PDs to be discussed in this work will be characterized based on these two major performance parameters.

1.2.1 Bandwidth

The bandwidth is defined as the frequency at which the output RF power decreases half or 3 dB relative to its DC power. The bandwidth is related to the response time. For UTC-PD, the response time is determined by the carrier transit time τ_{tr} and RC-time

constant τ_{RC}. Then, the 3-dB bandwidth f_{3dB} can be approximately expressed as Eq. (1.4). In order to improve the bandwidth performance, both τ_{tr} and τ_{RC} should be decreased.

$$f_{3dB} = \frac{1}{2\pi\sqrt{\tau_{tr}^2 + \tau_{RC}^2}} . \tag{1.4}$$

For a typical UTC-PD, the carrier transit time τ_{tr} includes the carrier diffusion time τ_A in the low electric field absorption layer, and the carrier drift time τ_C in the high electric field depleted collection layer. The diffusion time τ_A can be given by [6]

$$\tau_A = \frac{W_A^2}{3D_e} + \frac{W_A}{v_{th}} , \tag{1.5}$$

where W_A is the absorption layer thickness, D_e is the diffusion coefficient of electrons in the absorption layer and v_{th} is the electron thermionic emission velocity. The drift time can be expressed as [6]

$$\tau_C = \frac{W_C}{v_{os}} , \tag{1.6}$$

where W_C is the collection layer thickness and v_{os} is the overshoot velocity of the electrons. The carrier transit time can be reduced by reducing the thickness of absorption and collection layers. Additionally, a built-in electric field can be constructed in the absorption layer to accelerate the electrons, and thus shorten the transit time. When the thickness of absorption layer is similar to that of the collection layer, the carrier transit time τ_{tr} is primarily limited by the carrier traveling time τ_A in absorption layer, since the

electron diffusion velocity is much slower than the electron drift velocity. Thus, τ_{tr} can be approximated as follows,

$$\tau_{tr} = \tau_A + \tau_C \approx \tau_A = \frac{W_A^2}{3D_e} + \frac{W_A}{v_{th}} . \tag{1.7}$$

On the other hand, the RC-time constant τ_{RC} can be expressed as [10]

$$\tau_{RC} = R_{tot}C_{pd} = \frac{(R_S + R_L)\varepsilon A}{W} , \tag{1.8}$$

where R_{tot} is the total resistance including series resistance R_S and load resistance R_L. C_{pd} is the junction capacitance, which is determined by the thickness W of depletion region and the area A of the active region. And ε is the permittivity of the depletion region. The RC-time constant τ_{RC} can be minimized by decreasing the area of active region or increasing the thickness of depletion region. However, the contact resistance is inversely proportional to the contact area, and a thicker depletion region leads to a longer transit time, therefore trade-offs exist in these aspects.

The 3-dB frequency f_{3dB} can be extracted by using two different methods. The first method is to obtain the 3-dB frequency from the Fourier transform of the pulse response. The other method is that, the bandwidth of the device can be evaluated from the frequency response to a modulated optical signal. In this work, the second method is used to analyze the bandwidth performance.

1.2.2 Output RF power

The output RF power of the UTC-PD refers to the power delivered to load resistance, which can be expressed as follows [9][10],

$$P_{RF}(f) = \frac{R_L r^2 P_{op}^2 ML}{2[1+(2\pi f \tau_{tr})^2][1+(2\pi f \tau_{RC})^2]}. \tag{1.9}$$

Here, f is the frequency, R_L is the load resistance, r is responsivity, P_{op} is the input optical power, M is a factor related to the optical modulation index, and L is a factor related to optical and electrical losses. Due to the development of the optical fiber amplifier, it is desired to place the the optical fiber amplifier directly in front of the photodiode to eliminate the costly post-amplifier. This is because, as the frequency increases, a photoreceiver consisting of an optical pre-amplifier and a high-power photodiode can produce better characteristics than a conventional photoreceiver with electrical post-amplifiers, and the system configuration can be simplified as well [6]. Thereby, high-speed and high-output power photodiodes with high-power handling capability are required.

According to Eq. (1.9), the output power decreases as the frequency increases, since the carrier transit time and RC-time constant limitations become significant. On the other hand, the output power rises with increasing input optical power. However, as the input

optical power grows, the space-charge effect becomes significant. Due to the space charge, the electric field in the front part of depletion region drops, and thus the carrier velocity is reduced, which in turn causes the degradation of bandwidth and output power. The output power saturation occurs when the input optical power is high enough. At high optical injection level, owing to the space-charge effect, the high-speed performance of UTC-PD is limited, which results in the output power decreases more rapidly with increasing frequency. The space-charge effect can be weakened by increasing the reverse bias voltage. However, this may cause the thermal failure.

In this work, the output RF power performance is evaluated from the DC photocurrent response to the optical source. This is because, the current is related to the output power, and they are closely affected by the space-charge effect. Both of them increase linearly with the incident optical power, and then deviate from the linear response, which effectively indicates the saturation occurs.

1.3 Motivation of this research

1.3.1 Literature review

In the past decade, there has been an increasing interest in UTC-PD due to its excellent speed and saturation current performance. Various improvements, in terms of

layer structure, optical coupling and packaging, have been achieved. As the UTC-PD reported in [11], the most straightforward way to enhance the speed performance is to scale down the thickness of absorption layer. However, thin absorption layer seriously reduces the responsivity of the device. It has been experimentally demonstrated that the bandwidth performance of UTC-PD can be improved by incorporating a step-like doping profile in the photoabsorption layer, since the introduced built-in electric field can help electrons transport more rapidly into the collector [12]. The modified UTC-PD (MUTC-PD) structures, which employ partially depleted absorption layer to improve the bandwidth and the quantum efficiency, have been achieved [13]-[15]. Besides, the saturation current performance of the MUTC-PD can be enhanced by inserting a cliff layer before the collector [16]. A non-uniformly doped collector was designed to relax the space-charge effect, and thus the saturation current can be enhanced [17]. Superior bandwidth and output power performance of Near-ballistic UTC-PD (NBUTC-PD) has been demonstrated [18]-[19]. Moreover, different methods of optical coupling have been developed [20]-[23]. For instance, an edge-coupled waveguide UTC-PD was demonstrated to show improved performance [24]. Additionally, in terms of fabrication process improvements, well-designed packaging techniques, which are used to effectively manage the heat sinking problem, have been implemented [25]-[27]. By

flip-chip bonding the UTC-PDs on submounts with high thermal conductivity, the power handling capability of PDs can be increased, and thus the high-power performance is greatly improved [28].

1.3.2 Motivation

In this thesis, in order to improve the bandwidth and saturation performance of UTC-PD, we developed novel absorption layer and collection layer structures. And the effects of these structures are investigated by using a numerical device simulator.

1.4 Thesis organisation

The rest of the thesis is organized as follows.

Chapter 2 describes the device structure and the physics-based modeling of the considered UTC-PD. It is noted that hot carrier transport equations are enabled in our simulation. The simulation results are compared with the reported results to ensure the accuracy of the physical modeling. Then, in the following chapters, the UTC-PDs are investigated and designed by using physics-based modeling.

In chapter 3, the bandwidth performance of the considered UTC-PD is investigated and enhanced. First of all, the effect of widely used linearly graded doping absorption

layer is studied. Then, the function of graded bandgap absorption layer is investigated. Moreover, both the methods are optimized by using partially graded structure. Finally, the benefits of proposed combined graded absorption layer are presented.

In chapter 4, the saturation performance of the considered UTC-PD is investigated and improved. Firstly, the space-charge effect and charge compensation effect is studied. Then, a collection layer with linear doping profile is proposed and optimized, a better saturation performance is predicted. Furthermore, a Gaussian doping profile is proposed, which can further improve the saturation performance.

Chapter 5 presents two the epitaxial layer structures of designed UTC-PDs. Their bandwidth and saturation performance is simulated. Additionally, the major steps of the fabrication process are described.

Chapter 6 presents the conclusions and suggestions for future work.

Chapter 2 Physics-Based UTC-PD Modeling

The performance of the UTC-PD can be predicted by using the physics-based modeling. One of the advantages of the physics-based simulation method is that, the device can be studied in detail without costly experiments. Appropriate physical models must be incorporated to ensure the accuracy of the modeling. The drift-diffusion model is widely used to describe the carrier transport. However, the drift-diffusion approximation becomes less accurate in the simulation of submicron devices. The non-local effects, such as velocity overshoot, which has been observed experimentally in UTC-PDs [29], is not considered in this model. Therefore, in this work, a more appropriate energy balance transport model is employed in the device modeling. Then, different device structures are studied and designed based on the simulation results, which are obtained by solving hot carrier transport equations.

A commercial physics-based device simulator ATLAS, by Silvaco International, is used in this work. ATLAS provides general capabilities for physics-based two (2D) and three-dimensional (3D) simulation of semiconductor devices [30]. It contains a comprehensive set of physical models, including drift-diffusion transport models, energy balance and hydrodynamic transport models, concentration, electric field and temperature

dependent mobility models, carrier generation and recombination models, etc. And it employs powerful numerical techniques, such as Gummel, Newton, and block-Newton nonlinear iteration strategies. In ATLAS, semiconductor device can be modeled by a set of coupled and non-linear partial differential equations, which are derived from Maxwell's laws [30]. After defining a fine meshed physical structure and setting reasonable parameters, by using the provided numerical methods, numerical solutions of these equations can be obtained on every grid points within the device structure. Based on these results, the electric field can be obtained at any position within the device, and the diffusion and drift current, as well as terminal current and voltage, can be calculated. Furthermore, the performance of the device can be achieved in DC, AC small signal or transient modes of operation under different bias conditions. Thus, the transport phenomena within the device can be analyzed and the characteristics can be predicted as well.

In this chapter, we first describe the basic device structure which will be considered in this chapter and next two chapters. Subsequently, we present some important material properties and physical models which are employed for device simulation. Moreover, several important equations which are solved inside the simulator are introduced. Finally,

in order to verify the accuracy of our physical modeling, we compared the simulation results with the experimental results in [6] and the simulated results in [31].

2.1 Device structure

In this and next chapter, we will consider a basic UTC-PD device structure which is reported by T. Ishibashi et al. [6]. The epitaxial layers are shown in Table 2.1. In addition to the absorption layer and the collection layer, the other layers are used as electrical contact layers or are added for improving performance. The topmost layer is the p-type InGaAs contact layer, which contacts with the anode metal. In order to form a good ohmic contact, this layer is heavily doped. It is followed by a wide bandgap p-type InGaAsP blocking layer which is lattice matched to InP. Since the energy gap of the blocking layer is 0.85 eV, and the energy gap of the following p-type InGaAs absorption layer is 0.737 eV, a conduction band offset ΔE_c is formed at the blocking layer and absorption layer interface, which serves as a diffusion barrier for the electrons in the absorption layer. Thus, the role of the blocking layer is to promote the electrons generated in the absorption layer to move towards the InP collection layer and to prevent the diffusion of the electrons to the anode, while allowing the holes pass through. Followed is a typical uniformly doped p-type InGaAs layer that is used as the absorption

layer. It is highly doped to $1x10^{18}$ cm^{-3} and the thickness is 220 nm. Corresponding to the optical wavelength of 1.55 μm, which is equivalent to photon energy of 0.8 eV, the energy gap of this absorption layer is designed to be 0.737 eV to ensure the electrons can be excited from the valence band to the conduction band. Relatively, in order to avoid optical absorption, a n-type InP layer which has a wide energy gap of 1.35 eV is adopted as the collection layer. It is uniformly doped to $1x10^{16}$ cm^{-3} for charge compensation. Moreover, the doping concentration is very low to ensure this region can be completely depleted at normal device operation bias. Since there is an abrupt conduction band barrier at the InGaAs and InP heterojunction interface, which may block the electrons and lead to degradation of the sensitivity and photocurrent, undoped InGaAs, InGaAsP and InP space layers are employed to form a smooth connection between the absorption layer and collection layer. The energy gap of the inserted InGaAsP space layer is 1.0 eV. Additionally, a n-type thin InP cliff layer is added between the undoped InP spacer layer and the lightly doped InP collection layer. This cliff layer, which is highly doped to $1x10^{18}$ cm^{-3}, is used to enhance the electric field in the depleted region near the absorption layer and collection layer interface. Finally, similar to the p-type contact layer, the cathode metal is connected to the n-type InP subcollection layer, which is heavily doped to reduce the contact resistance.

Table 2.1 Epitaxial layers of the UTC-PD reported in [6].

Layer	Thickness (nm)	Doping (cm^{-3})/Type	Band gap E_g (eV)
p++InGaAs contact	50	3×10^{19}/P	0.737
p++InGaAsP blocking	20	2×10^{19}/P	0.85
p+ InGaAs absorption	220	1×10^{18}/P	0.737
i-InGaAs space	8	--	0.737
i-InGaAsP space	16	--	1.0
i-InP space	6	--	1.35
n+ InP cliff	7	1×10^{18}/N	1.35
n- InP collection	263	1×10^{16}/N	1.35
n+ InP subcollection-2	50	5×10^{18}/N	1.35
n+ InGaAs etch stop	10	1.5×10^{19}/N	0.737
n+ InP subcolleciton-1	500	1.5×10^{19}/N	1.35
i-InGaAs etch stop	10	--	0.737

(S. I. InP Sub)

2.2 Definition of material parameters and models

In order to simulate the UTC-PD as described above, the following basic steps are performed in ATLAS. First of all, we need to define the device structure as listed in Table 2.1, for example, specifying regions and electrodes, as well as the doping profiles. Secondly, we should specify the mesh of structure, which generates a suitable grid to ensure the accuracy of the simulation. Once we define the device structure and the mesh, we can set the material parameters. For commonly used conventional materials, such as InP, we adopt the default parameters contained in the simulator. For unusual materials, the essential parameters are obtained from the reported literatures and website [32]. Then,

we need to specify reasonable physical models. Subsequently, the optical source should be defined. After these steps, we choose suitable numerical methods to calculate the solutions to the specified device problems. Finally, DC, AC small signal and transient simulations can be obtained at different bias, light intensity and frequency conditions as we specified. In the following sections, we present some important parameters that need to be defined in ATLAS. For instance, the composition fractions x and y of $In_{1-x}Ga_xAs_yP_{1-y}$ which have a marked impact on the energy bandgap and band offsets distribution, as well as the optical parameters which we obtained from the reported literature and employed in ATLAS. Moreover, the physical models, which we used for UTC-PD simulation, are described.

2.2.1 Energy gaps and heterojunction band offsets setting

As mentioned above, for the UTC-PD reported by T. Ishibashi et al. [6], there are two different layers constituted by a quaternary material InGaAsP. One of them is the InGaAsP blocking layer, which is used to promote the electrons generated in the absorption layer move towards the InP collection layer and to prevent the diffusion of the electrons to the anode, while allowing the holes pass through. The other one is the InGaAsP space layer which is inserted between the absorption layer and collection layer

and acts as a intermediate layer to flatten the conduction band barrier and facilitate electrons to transport into the InP collection layer. The functions of these two different layers are realized by specifying different energy gaps. And the energy bandgap of the $In_{1-x}Ga_xAs_yP_{1-y}$ quaternary material is determined by its composition fractions x and y. Thus, the setting of values of the composition fractions is very important when we initially define the device structure.

The default energy gap for the InP lattice matched $In_{1-x}Ga_xAs_yP_{1-y}$ system used in the simulator is given by [30]

$$\begin{aligned} E_g(\mathrm{In_{1\text{-}x}Ga_xAs_yP_{1-y}}) = 1.35 + (0.642 + 0.758x)x + (0.101y - 1.101)y \\ -(0.28x - 0.109y + 0.159)xy \end{aligned} \quad (2.1)$$

Since this $In_{1-x}Ga_xAs_yP_{1-y}$ material must be lattice matched to InP, the relationship between x and y that satisfy this condition is given by [33]

$$x = \frac{0.1896y}{0.4176 - 0.0125y}. \quad (2.2)$$

According to these two equations, we can obtain the values of the composition fractions for the $In_{1-x}Ga_xAs_yP_{1-y}$ layers which are employed in the considered UTC-PD. For the blocking layer which is designed to have an energy gap of 0.85 eV, the corresponding values of composition fractions are calculated as x=0.351, y=0.755. For the space layer which has an energy gap of 1.0 eV, the composition fractions are given by x=0.230, y=0.499.

Once we set the composition fractions for every layer in the UTC-PD, the energy gap of each layer is determined. Then, the conduction and valence band discontinuities are formed by the difference between the energy gaps of two adjacent materials. Since the distribution of energy gap between the conduction and valence bands has a large impact on the charge transport, it is very important to properly define the conduction band offset ΔE_c and the valence band offset ΔE_v at each heterojunction interface. Thereby, the energy gap of each layer should be properly aligned [34]. In the simulator, one of the methods that defines the conduction band alignment for a heterointerface is to manually adjust the material affinities by specifying the AFFINITY parameter in the MATERIAL statement. The procedure for aligning heterojunctions using this method is described as follows.

First of all, the electron affinity of $In_{0.53}Ga_{0.47}As$ is set to 4.58 eV [33]. For the $In_{1-x}Ga_xAs_yP_{1-y}$ and $In_{0.53}Ga_{0.47}As$ heterojunction system that is lattice matched to InP, the conduction band offset ΔE_c and the valence band offset ΔE_v can be expressed mathematically in terms of the composition of the quaternary as follows [33],

$$\Delta E_c(y) = 0.271 - 0.268y + 0.003y^2, \tag{2.3}$$

$$\Delta E_v(y) = 0.35 - 0.502y + 0.152y^2. \tag{2.4}$$

Accordingly, at the above described $In_{0.649}Ga_{0.351}As_{0.755}P_{0.245}$ blocking layer and $In_{0.53}Ga_{0.47}As$ absorption layer heterojunction interface, we can obtain that ΔE_c=0.07 eV and ΔE_v=0.058 eV. Then, the electron affinity of the $In_{0.649}Ga_{0.351}As_{0.755}P_{0.245}$ blocking layer can be derived from the conduction band offsets ΔE_c and the specified electron affinity of $In_{0.53}Ga_{0.47}As$. Accordingly, the electron affinity of the wide energy gap blocking layer is adjusted to 4.58-0.07=4.51 eV to ensure the desired conduction band offset at the heterojunction interface. Similarly, at the $In_{0.53}Ga_{0.47}As$ and $In_{0.77}Ga_{0.23}As_{0.499}P_{0.501}$ space layer heterojunction interface, the corresponding conduction band offset ΔE_c is 0.138 eV and the valence band offset ΔE_v is 0.137 eV. Thereby, the electron affinity of the $In_{0.77}Ga_{0.23}As_{0.499}P_{0.501}$ space layer should be modified to 4.58-0.138=4.442 eV. Subsequently, for the following lattice matched $In_{1-x}Ga_xAs_yP_{1-y}$ and InP heterojunction system, the equations to calculate the band offsets are given by [33]

$$\Delta E_c = 0.268y + 0.003y^2, \tag{2.5}$$

$$\Delta E_v = 0.502y - 0.152y^2. \tag{2.6}$$

According to the above equations, the band offsets at the $In_{0.77}Ga_{0.23}As_{0.499}P_{0.501}$ and InP space layer interface can be calculated as ΔE_c=0.134 eV and ΔE_v=0.213 eV respectively. Therefore, we need to set the AFFINITY parameter of InP to 4.442-0.134=4.308 eV.

The distribution of the band offsets of the considered UTC-PD is illustrated in Fig. 2.1. We can seen that, as we expect, a conduction band barrier is formed at the blocking and absorption layer interface, which is used to prevent the optically generated electrons from diffusing to the anode. Furthermore, the inserted $In_{0.77}Ga_{0.23}As_{0.499}P_{0.501}$ space layer divide the 272 meV conduction band discontinuity into two smaller steps, which effectively mitigates the blocking effect between the InGaAs absorption layer and InP collection layer.

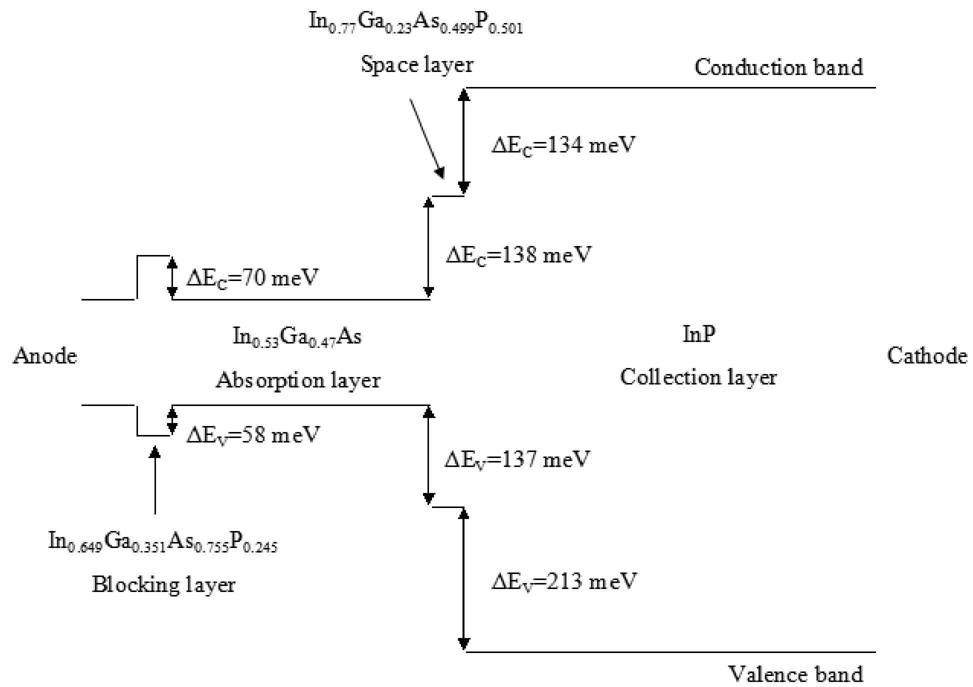

Figure 2.1 Conduction and valence band offsets for heterojunctions presented in UTC-PD and used in the numerical modeling.

2.2.2 Defining optical properties of materials

Since UTC-PD is an optoelectronic device, the optical properties of the materials are crucial for device simulation. One of the most important optical parameters is the complex index of refraction $\tilde{n} = n + i\kappa$. Here, the real part of the refractive index n indicates the phase velocity, while the imaginary part κ indicates the amount of absorption loss when the electromagnetic wave propagates through the material [35]. In the absorption layer of UTC-PD, the incident light intensity at a distance z into the absorption layer decays exponentially from the surface. It can be expressed as

$$P(y) = P_0 \exp(-\alpha z), \tag{2.7}$$

where P_0 is the intensity of the incident radiation and α is the absorption coefficient. Then, based on this expression, the generation rate formula can be derived. In ATLAS, the generation rate formula is given by [30]

$$G = \eta_0 \frac{P\lambda}{\hbar c} \alpha \exp(-\alpha z), \tag{2.8}$$

where P is the ray intensity factor, which contains the cumulative effects of reflections, transmissions, and loss due to absorption over the ray path, η_0 is the internal quantum efficiency, z is a relative distance for the ray, ħ is Planck's constant, c is the speed of light, λ is the wavelength and α is the absorption coefficient. The generation associated with

each grid point can be calculated by integration of the generation rate formula. In addition, for ATLAS, the absorption coefficient α is obtained from the imaginary part κ of the complex index of refraction, according to the following Eq. (2.9) [30],

$$\alpha = \frac{4\pi}{\lambda}\kappa . \tag{2.9}$$

Hence, absorption or photogeneration is related to the imaginary component of refractive index. On the other hand, for the simulator, optical ray tracing model uses the real component of refractive index to calculate the optical intensity at each grid point [30]. Therefore, taking all these descriptions, we must carefully specify the complex index of refraction of the specific regions in the device structure.

For the considered UTC-PD, InGaAs is the material used for photoabsorption. And the device is designed to operate at the optical wavelength of 1.55 μm, which is equivalent to photon energy of 0.8 eV. The following Fig. 2.2, which is reported by S. Adachi [33], shows the experimental data of n and κ for InGaAs at 300K. According to Fig. 2.2, we can find the values of n and κ at the photon energy of 0.8 eV, which are 3.595 and 0.057 respectively. Then, we specify the real and imaginary part of refractive index for the InGaAs absorption layer by using the REAL.INDEX and IMAG.INDEX parameters of the MATERIAL statement in ATLAS. Additionally, since we study the back-illuminated device, we assume the InGaAsP space layer and InP collection layer are

transparent at the optical wavelength of 1.55 μm. Thereby, for these transparent layers, we set the imaginary part κ of refractive index to zero. For InP, the real part of refractive index n is specified as 3.165 [36]. And for $In_{1-x}Ga_xAs_yP_{1-y}$, we can define its real part of refractive index according to the relation n=3.1+0.46y [37].

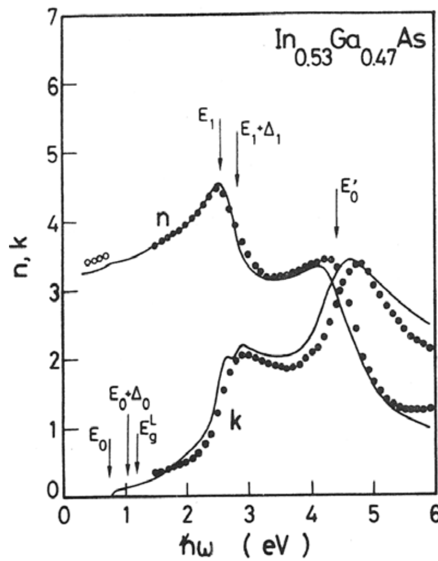

Figure 2.2 Real and imaginary parts of the refractive index for InGaAs versus photon energy [33].

2.2.3 The energy balance transport model

The conventional drift-diffusion model is the simplest charge transport model. It is useful for most of the common devices. However, as the sizes of the devices become smaller, this drift-diffusion approximation is less accurate, since it neglects non-local effects such as velocity overshoot, diffusion associated with the carrier temperature and the dependence of impact ionization rates on carrier energy distributions. These non-local

effects are considered very important in the simulation of submicron devices. In addition, electron velocity overshoot has been observed experimentally in UTC-PDs [29]. The electron velocity plays a significant role in determining the performance of UTC-PD. Therefore, in order to ensure the accuracy of the simulation for the studied UTC-PD, the non-local model of charge transport is required.

In ATLAS, these effects can be modeled by using the energy balance transport model. The energy balance transport model follows the derivation by Stratton [38]-[39], which is derived starting from the Boltzmann transport equation. The energy balance equations are given by [30]

$$\nabla \cdot S_n = \frac{1}{q} J_n \cdot E - W_n - \frac{3k}{2} \frac{\partial}{\partial t} (\lambda_n^* n T_n), \tag{2.10}$$

$$\nabla \cdot S_p = \frac{1}{q} J_p \cdot E - W_p - \frac{3k}{2} \frac{\partial}{\partial t} (\lambda_p^* p T_p), \tag{2.11}$$

in which J_n and J_p are the current densities, S_n and S_p are the energy flux densities from the carrier to the lattice. They can be expressed as [30]

$$J_n = qD_n \nabla n - q\mu_n n \nabla \psi + qnD_n^T \nabla T_n, \tag{2.12}$$

$$J_p = -qD_p \nabla p - q\mu_p p \nabla \psi - qpD_p^T \nabla T_p, \tag{2.13}$$

$$S_n = -K_n \nabla T_n - \left(\frac{k\delta_n}{q} \right) J_n T_n, \tag{2.14}$$

$$S_p = -K_p \nabla T_p - \left(\frac{k\delta_p}{q} \right) J_p T_p. \tag{2.15}$$

Here, T_n and T_p are the temperature of electrons and holes, W_n and W_p are the energy density loss rates for electrons and holes, D_n and D_p are the thermal diffusivities for electrons and holes, and K_n and K_p are the thermal conductivities of electrons and holes. For our simulation, in order to take into account the electron velocity overshoot effect, we specified HCTE.EL parameter in the MODELS statement to activate the hot carrier transport equations for electrons only.

2.2.4 Mobility models

Carrier mobilities are the functions of the doping concentration, local electric field, lattice temperature, and so on. The simulator ATLAS provides several models to account for these effects. For the studied UTC-PD, we need to consider carriers mobilities in low-field behavior and high-field behavior. Suitable mobility models are employed for the simulation. They will be presented as follows.

2.2.4.1 Concentration dependent mobility model

For the low-field condition, the carrier mobility is affected by impurity scattering. The mobilities of holes and electrons decrease with increasing doping concentration.

Thus, the CONMOB model is employed. It provides empirical data for the doping dependent low-field mobilities of electrons and holes [30].

2.2.4.2 Parallel electric field dependent mobility model

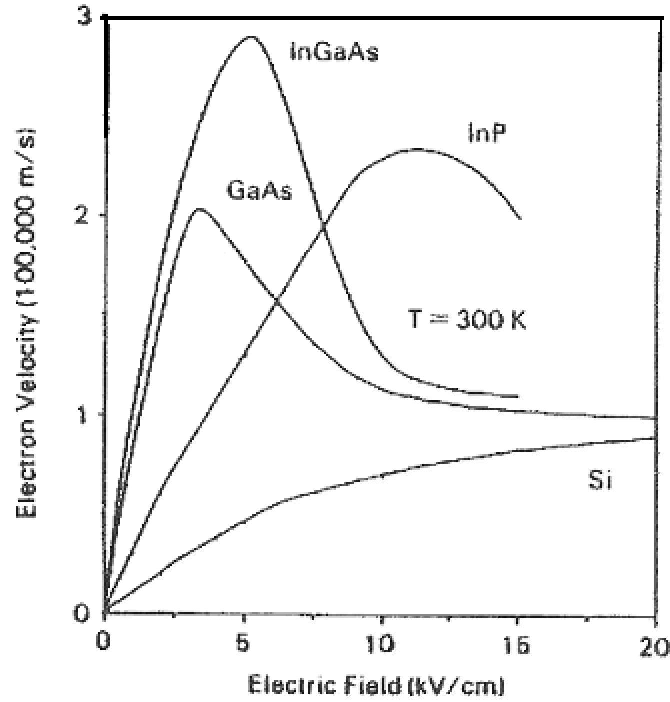

Figure 2.3 Electron velocity field characteristics for InGaAs, GaAs and InP [40].

Fig. 2.3 shows the electric field dependence of the electron drift velocity for InGaAs and InP (materials used in the studied UTC-PD) [40]. We can see that, at low-field region, the electron drift velocity v_d increases proportionally with the electric field. It can be expressed as

$$v_d = \mu E , \tag{2.16}$$

where E is the electric field, μ is the carrier mobility. While, at high electric field, drift velocity no longer increases linearly with increasing electric field, and eventually, it tends to saturation. This is because the carrier energy obtained from electric field is transferred to lattice during the scattering processes. Since the magnitude of the drift velocity is the product of the mobility and the electric field, at high electric field, the effective mobility need to be reduced. In ATLAS, this field dependent mobility can be modeled by using parallel electric field mobility model FLDMOB. This model employ the following Caughey and Thomas expression [41] (Eq. (2.17) and Eq. (2.18)) to implement a field dependent mobility. Thereby, a smooth transition between low-field and high-field behavior is achieved.

$$\mu_n(E) = \mu_{n0}\left[\frac{1}{1+\left(\frac{\mu_{n0}E}{v_{satn}}\right)^{\beta_n}}\right]^{\frac{1}{\beta_n}}. \tag{2.17}$$

$$\mu_p(E) = \mu_{p0}\left[\frac{1}{1+\left(\frac{\mu_{p0}E}{v_{satp}}\right)^{\beta_p}}\right]^{\frac{1}{\beta_p}}. \tag{2.18}$$

Here, μ_{n0} and μ_{p0} are the low-field electron and hole mobilities respectively, v_{satn} and v_{satp} are the saturation velocities of electron and hole respectively and β_n and β_p are user-definable parameters, which we use their defaults, i.e. β_n=2 and β_p=1. The low-field

mobilities μ_{n0} and μ_{p0} are obtained from the previously described low-field mobility model.

2.2.4.3 Energy dependent mobility model

For the employed energy balance transport model, the carrier mobility is required to be related to the carrier energy. This can be achieved through the homogeneous steady state energy balance relationship. The effective electric fields, $E_{eff,n}$ and $E_{eff,p}$, need to be calculated, according to the following equations derived from the energy balance equations [30].

$$q\mu_n(E_{eff,n})E_{eff,n}^2 = \frac{3}{2}\frac{k(T_n - T_L)}{\tau_{mob,n}}, \tag{2.19}$$

$$q\mu_p(E_{eff,p})E_{eff,p}^2 = \frac{3}{2}\frac{k(T_p - T_L)}{\tau_{mob,p}}. \tag{2.20}$$

Here, T_L is the lattice temperature, k is Boltzmann's constant and $\tau_{mob,n}$ and $\tau_{mob,p}$ are user-definable parameters, which we use their defaults, $\tau_{mob,n}=\tau_{mob,p}=2.5\text{x}10^{-13}$ s. Then, these effective electric fields are introduced into the relevant field dependent mobility model.

In the above mentioned FLDMOB model, the carrier mobility is not dependent on temperature. While, in energy balance transport model, the carrier mobility is treated as function of the carrier temperature rather than function of the local electric field. Thus,

the standard saturation model is chosen by setting EVSATMOD=0 on the MODELS statement. In this model, the carrier mobility, which depends on the carrier temperature, can be expressed as follows [30],

$$\mu_n = \frac{\mu_{n0}}{(1+X_n^{\beta_n})^{\frac{1}{\beta_n}}}, \tag{2.21}$$

$$\mu_p = \frac{\mu_{p0}}{(1+X_p^{\beta_p})^{\frac{1}{\beta_p}}}, \tag{2.22}$$

in which,

$$X_n^{\beta_n} = \frac{1}{2}(\alpha_n^{\beta_n}(T_n - T_L)^{\beta_n} + \sqrt{\alpha_n^{2\beta_n}(T_n - T_L)^{2\beta_n} - 4\alpha_n^{\beta_n}(T_n - T_L)^{\beta_n}}), \tag{2.23}$$

$$X_p^{\beta_p} = \frac{1}{2}(\alpha_p^{\beta_p}(T_p - T_L)^{\beta_p} + \sqrt{\alpha_p^{2\beta_p}(T_p - T_L)^{2\beta_p} - 4\alpha_p^{\beta_p}(T_p - T_L)^{\beta_p}}), \tag{2.24}$$

$$\alpha_n = \frac{3}{2}\frac{k_B \mu_{n0}}{q v_{satn}^2 \tau_{el,n}}, \tag{2.25}$$

$$\alpha_p = \frac{3}{2}\frac{k_B \mu_{p0}}{q v_{satp}^2 \tau_{el,p}}. \tag{2.26}$$

Here, $\tau_{el,n}$ and $\tau_{el,p}$ are the energy relaxation times for electrons and holes.

2.2.5 Recombination models

For the studied UTC-PD, in order to return to equilibrium after the generation of electron-hole pairs, the carrier recombination occurs in the device. According to the form of the lost energy of electron, the generation-recombination mechanisms can be divided

into several types, such as phonon transitions and Auger transitions. Thus, in ATLAS, we need to specify the suitable models to simulate these processes.

2.2.5.1 Shockley-Read-Hall (SRH) concentration dependent lifetime model

One of the generation-recombination process that we considered is phonon transitions. Phonon transitions occur in the presence of a trap or defect within the forbidden gap of the semiconductor [30]. This is a two step process. An carrier is trapped by an energy state in the forbidden region, recombination occurs when another carrier of the opposite conductivity type interacts with the same energy state. This process is called Shockley-Read-Hall (SRH) recombination. Moreover, the carrier lifetime is an important parameter in the modeled SRH recombination equations. The carrier lifetime depends on the impurity concentration. It decreases as the impurity concentration increases. Thereby, in the simulator, we modeled this recombination process by using SRH concentration dependent lifetime model CONSRH. By using this model, the net generation-recombination rate is given as [30]

$$R_{SRH} = \frac{pn - n_{ie}^2}{\tau_n[p + n_{ie}\exp(\frac{-ETRAP}{kT_L})] + \tau_p[n + n_{ie}\exp(\frac{ETRAP}{kT_L})]}, \quad (2.27)$$

in which,

$$\tau_n = \frac{\tau_{n0}}{1+(\frac{N}{NSRHN})}, \quad (2.28)$$

$$\tau_p = \frac{\tau_{p0}}{1+(\frac{N}{NSRHP})}. \quad (2.29)$$

Here, ETRAP is the difference between the trap energy level and the intrinsic Fermi level, τ_{n0} and τ_{p0} are the user-definable electron and hole lifetimes, N is the total impurity concentration and NSRHN and NSRHP are user-definable parameters.

For the studied UTC-PD, the p-type InGaAs absorption layer is very important. In order to ensure the accuracy of the simulation, the carrier lifetime in p-type InGaAs need to be specified according to the the literature as follows. First of all, for p-type material under low injection condition, the recombination rate Eq. (2.27) can be reduced to

$$R_{SRH} = \frac{n-n_0}{\tau_n}, \quad (2.30)$$

where n is the total minority electron concentration, n_0 is the thermal equilibrium electron concentration and τ_n is the minority carrier electron lifetime. Thus, we only need to consider the minority carrier electron lifetime in p-type InGaAs absorption layer. Then, according to the experimental data reported by Tashima et al. [42], it is found that the electron lifetime in p-type InGaAs is a function of the doping level. The electron lifetime decreases as the doping concentration increases. Furthermore, Conklin et al. [43] proposed an exponential empirical model to fit the experimental data. This empirical model can be written as [43]

$$\tau_n(n\sec) = 10^{\beta-\gamma\log N_A}, \tag{2.31}$$

where N_A is the base doping concentration and the fit parameters are β=12.6, γ=0.73 for N_A>8x10^{17} cm^{-3}. For the doping concentration smaller than 8x10^{17} cm^{-3}, a constant lifetime of 0.3 ns was assumed. Subsequently, we need to fit the concentration dependent lifetime model, which is employed in ATLAS, to the data of this empirical model. For the studied UTC-PD, the p-type InGaAs absorption layer is highly doped to 1x10^{18} cm^{-3}. Thus, for the empirical model, we consider the case of N_A>8x10^{17} cm^{-3}. Thereby, the corresponding parameters used in the CONSRH model can be specified as τ_{n0}=0.7 ns and NSRHN=7.134x10^{17} cm^{-3}. The fitting result is shown in Fig. 2.4.

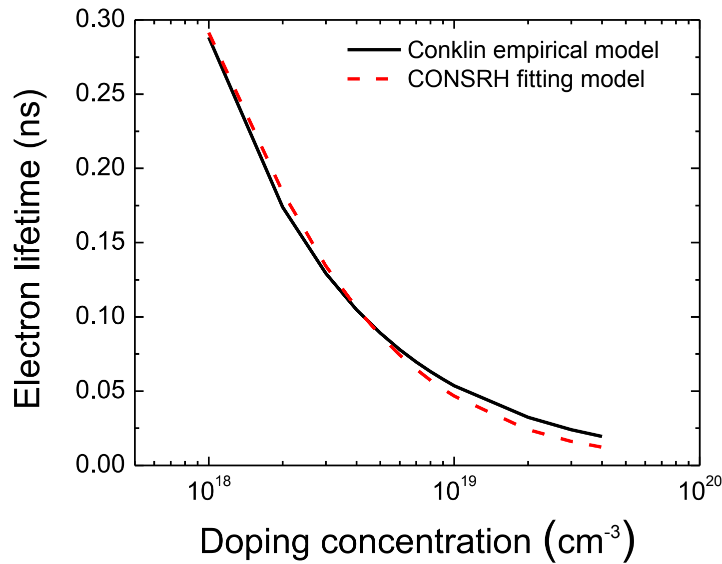

Figure 2.4 Electron lifetime in p-type InGaAs as a function of doping concentration. The solid line is calculated by using Conklin's empirical model [43]. The dashed line is the fitting result of CONSRH model.

2.2.5.2 Standard Auger model

The SHR recombination is dominant under conditions of low carrier concentration or low level injection. However, at high carrier concentration or high level injection, electrons and holes are more likely to directly interact, which leads to Auger recombination. Therefore, Auger transitions need to be considered. Auger recombination occurs through a three particle transition whereby a mobile carrier is either captured or emitted [30]. The excess energy given off by this recombination process is absorbed by another carrier. In ATLAS, the standard Auger model AUGER is employed to model this process as follows [44],

$$R_{Auger} = AUGN(pn^2 - nn_{ie}^2) + AUGP(np^2 - pn_{ie}^2)\,, \tag{2.32}$$

where the model parameters AUGN and AUGP are user-definable Auger coefficients. We specified these parameters according to the website [32].

2.3 Basic equations

Semiconductor device operation is modeled in ATLAS by a set of anywhere from one to six coupled, non-linear, partial differential equations [30]. For different models, we can obtain the solution of the corresponding equations by using the powerful numerical methods. In the following, several fundamental equations, which are solved

inside the simulator, are described, for instance, Poisson's equation, the continuity equations and the transport equations. Poisson's equation relates variations in electrostatic potential to local charge densities. The continuity and the transport equations describe the way that the electron and hole densities evolve as a result of transport processes, generation processes, and recombination processes [30].

2.3.1 Poisson's equation

Poisson's equation is given by [30]

$$div(\varepsilon \nabla \psi) = -\rho \, , \tag{2.33}$$

where ψ is the electrostatic potential, ε is the local permittivity and ρ is the local space charge density. For ATLAS, the intrinsic Fermi potential is defined as the reference potential. The local space charge density takes into account all the mobile and fixed charge. Moreover, the electric field E can be obtained from the gradient of the potential [30], by using Eq. (2.34).

$$E = -\nabla \psi \, . \tag{2.34}$$

Thereby, Poisson's equation relates local space charge density to electric field.

2.3.2 Carrier continuity equations

The carrier continuity equations consider the impact of the various mechanisms on the carrier concentration. They describe how the carrier concentration varies with time and space. The continuity equations for electrons and holes are defined as [30]

$$\frac{\partial n}{\partial t} = \frac{1}{q}\nabla \cdot J_n + G_n - R_n, \tag{2.35}$$

$$\frac{\partial p}{\partial t} = -\frac{1}{q}\nabla \cdot J_p + G_p - R_p, \tag{2.36}$$

where n and p are the electron and hole concentration, J_n and J_p are the electron and hole current densities, G_n and G_p are the generation rates for electrons and holes, R_n and R_p are the recombination rates for electrons and holes, and q is the magnitude of the charge on an electron.

2.3.3 The transport equations

The charge transport models, or the current density equations, are usually obtained by applying approximations and simplifications to the Boltzmann transport equation [30]. For the simulation of the submicron UTC-PD in this work, the energy balance transport model is employed. It uses a higher order approximation to the Boltzmann transport equation. Compared with conventional drift-diffusion model, it introduces new independent variables for electron and hole temperatures, adds continuity equations for

the carrier temperatures, and treats the carrier mobilities as functions of the carrier temperatures rather than functions of the local electric field. As described above, the current and energy flux densities can be expressed by Eq. (2.12)-Eq. (2.15).

2.4 Physical modeling verification

The accuracy of the modeling is verified by simulating the UTC-PD structure reported in [6], which has been described above. The UTC-PDs with active region area of 20 μm^2 and 80 μm^2 are considered, labeled here as device PD_{20} and PD_{80} respectively. The simulation results are compared with the reported results in [6] and [31]. In order to obtain the 3-dB bandwidth, the AC small-signal simulation is performed. As shown in Fig. 2.5 for PD_{20}, the 3-dB bandwidth at low illumination power and -2 V bias is 58.88 GHz, which is in good agreement with the experimental result 63 GHz in [6] and the simulation result 52 GHz in [31]. Moreover, the experimental results in [6] showed that there is a significant enhancement of bandwidth at high optical injection power, which has been explained by the self-induced field in the absorption layer. It is obvious that, this effect is also predicted. As can be seen from Fig. 2.5, for PD_{20}, the simulated 3-dB bandwidth at high optical injection level is 90.89 GHz and the corresponding measured result is 94 GHz. The simulated 3-dB bandwidth for PD_{80} at low optical injection level

and -2 V bias is 46.25 GHz, which is also comparable with the simulation result 42 GHz reported in [31]. It can be seen that there is a good agreement between all these simulation results and the reported results. And the physical modeling successfully predicted that the bandwidth varies with the change in the device active area, as well as the change in optical injection level. Consequently, the physics-based simulation is reliable. In chapter 3 and chapter 4, we will focus on the study of PD_{80}. Additionally, in all the simulations, the device is biased at -2 V .

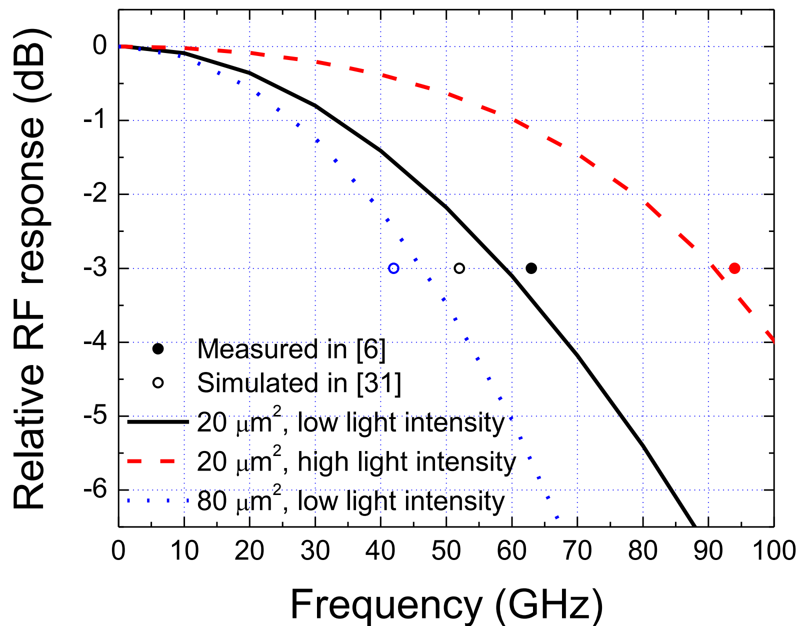

Figure 2.5 Simulated modulation response of device with active area of 20 and 80 μm^2 at -2 V bias voltage and the reported bandwidth in [6] and [31].

2.5 Summary

In this chapter, the physics-based modeling of UTC-PD is described in detail. The primary properties of InGaAs, InGaAsP and InP, which are the key materials employed in the studied UTC-PD, are presented. We also introduced the mathematical models which are implemented in the simulator ATLAS and are used for modeling UTC-PDs in this work. Furthermore, the accuracy of the modeling is verified by comparing the simulation results with experimental results. It is demonstrated that the performance of UTC-PDs can be successfully predicted by using the physics-based modeling method.

Chapter 3 Graded Absorption Layer Design

The 3-dB bandwidth of UTC-PD is mainly limited by the carrier transit time τ_{tr} and RC-time constant τ_{RC}. If the device performance is not RC-limited, the 3-dB bandwidth can be improved by decreasing the carrier transit time τ_{tr}. For a typical UTC-PD with uniformly doped absorption layer, the electric field in heavily doped absorption layer is nearly zero. The minority electrons can only diffuse from absorption layer to the collection layer. For the UTC-PD with similar absorption layer and collection layer thickness, the carrier transit time τ_{tr} is dominated by the electron transport time τ_A in the absorption layer. This is due to the fact that the electron diffusion velocity in the absorption layer is much smaller than the electron drift velocity in the high electric field collection layer, and thus the electron drift time in the collection layer is negligible. Therefore, in order to decrease the carrier transit time, we need to accelerate the minority electrons in the absorption layer. One approach is to introduce an appropriate built-in electric field in the absorption layer. Then the electron transport velocity in the absorption layer can be enhanced effectively. The built-in electric field can be introduced by using the graded absorption layer structure. This includes two aspects, graded doping structure and graded bandgap structure. In the following, they will be considered respectively.

3.1 Investigation of graded doping effects in absorption layer

The graded doping method is widely used in absorption layer. It can introduce a built-in electric field to accelerate the minority electrons, and thus reduce the carrier transit time. For example, the UTC-PD reported by Z. Li et al. [16], a step doping profile is adopted in the absorption layer. Similarly, a large slope of linearly graded doping profile is used in the absorption layer of the UTC-PD reported by J.-W. Shi et al., which can construct a built-in electric field from 2.1 kV/cm to 84 kV/cm [28].

For the studied UTC-PD, PD_{80}, the absorption layer is uniformly doped to $1x10^{18}$ cm^{-3}. In order to investigate the effect of the graded doping method, a linearly graded doping profile, which replaces the original uniform doping profile in [6], is employed in the absorption layer. We assume that the doping concentration in the absorption layer changes linearly from $1.75x10^{18}$ cm^{-3} to $2.5x10^{17}$ cm^{-3}, corresponding to the blocking layer side and the space layer side respectively. It is noted that the average doping concentration of linear doping is equal to the uniform doping concentration, which is $1.0x10^{18}$ cm^{-3} in the original absorption layer [6]. As shown in Fig. 3.1 and Fig. 3.2, the effects of the graded doping method can be observed from the electric field distribution in the 0.22-μm-thickness absorption layer (from 0.07 to 0.29 μm) and the modulation

response. The simulation results of the device with linearly doped absorption layer are compared with the results of the original device, which employs an uniformly doped absorption layer [6].

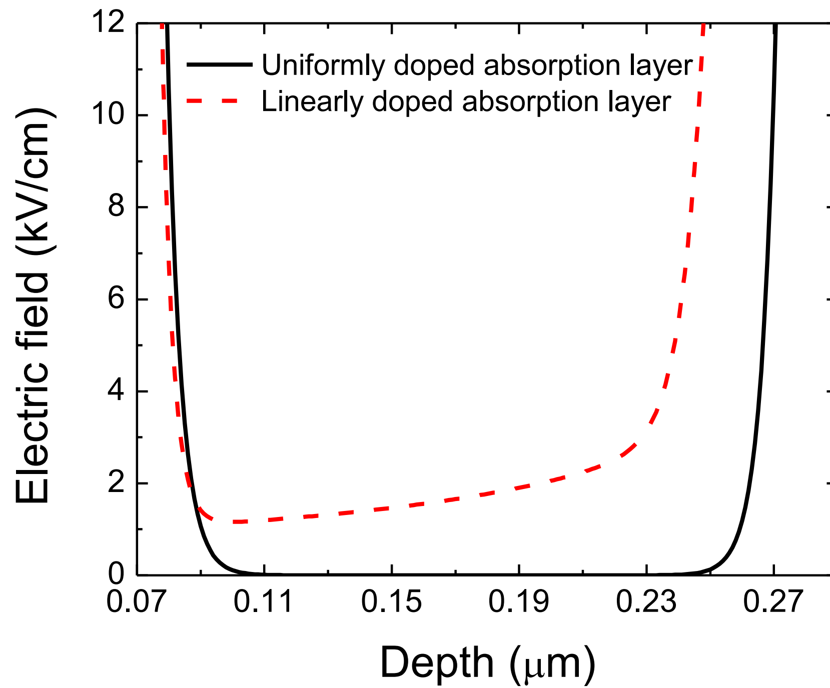

Figure 3.1 Distribution of electric field in the absorption layer of PD_{80} with uniformly and linearly doped absorption layer.

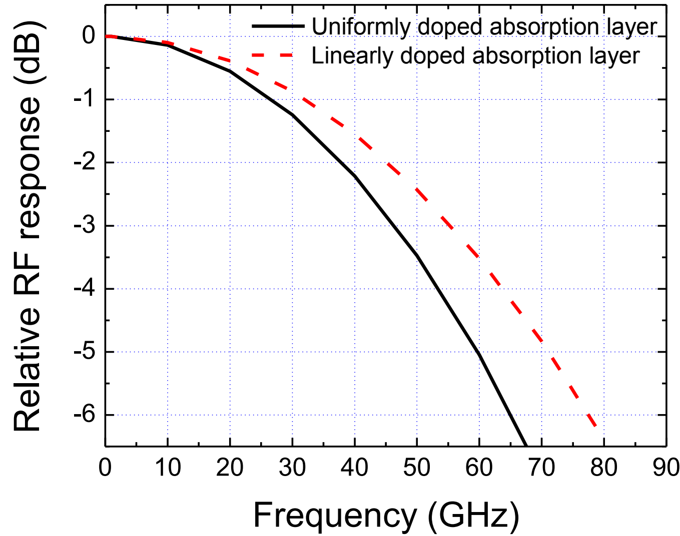

Figure 3.2 Simulated modulation response for PD_{80} with uniformly and linearly doped absorption layer.

As can be seen from Fig. 3.1, by using the linearly graded doping profile, the built-in electric field, which is introduced in the absorption layer, is greater than ~1 kV/cm. This built-in electric field can help the minority electrons move faster, and thus reduce the electrons transport time in the absorption layer. Therefore, the 3-dB bandwidth can be enhanced effectively. As plotted in Fig. 3.2 for PD_{80}, the 3-dB bandwidth is increased from 46.25 GHz to 55.25 GHz, an improvement of 19.5%.

3.2 Design of graded bandgap absorption layer structure

In this study, we propose a new method to construct a built-in electric field in the absorption layer and to further improve the bandwidth performance. That is, we employ a

graded bandgap structure in the absorption layer. The introduced potential gradient can accelerate the minority electrons in the absorption layer to transport from the diffusion barrier side to the collection layer side. For the InP and InGaAs material system, $In_{1-x}Ga_xAs_yP_{1-y}$ or $In_{1-x-y}Al_xGa_yAs$ with lattice matched to InP can provide a range of bandgaps, which can be used to construct a continuous compositionally-graded bandgap structure [45]. In this study, the graded bandgap absorption layer is designed by using $In_{1-x}Ga_xAs_yP_{1-y}$.

The design of the $In_{1-x}Ga_xAs_yP_{1-y}$ graded bandgap absorption layer is required to satisfy two conditions. Firstly, we need to ensure that the $In_{1-x}Ga_xAs_yP_{1-y}$ is lattice matched to InP. Thus, the composition fractions x and y should satisfy the relation given by Eq. (2.2). Secondly, since we assume the UTC-PD is operated at an optical wavelength of 1.5 μm, namely the photon energy of the light is 0.82 eV, the energy gap of the graded absorption region should be no more than 0.82 eV to excite an electron from the valence band to the conduction band. Thereby, the energy bandgap of $In_{1-x}Ga_xAs_yP_{1-y}$ should satisfy the following relation, $E_g(\mathrm{In_{1-x}Ga_xAs_yP_{1-y}}) \leq 0.82\mathrm{eV}$. As mentioned above, the energy bandgap of $In_{1-x}Ga_xAs_yP_{1-y}$, which is lattice matched to InP, is given by Eq. (2.1).

In order to satisfy the above two conditions, the range of the composition fraction x is found to be from 0.38 to 0.47. Correspondingly, the range of y is from 0.82 to 1. Thus, the maximum potential gradient in the absorption region can be formed by adopting linear compositionally-graded from $In_{0.62}Ga_{0.38}As_{0.82}P_{0.18}$ to $In_{0.53}Ga_{0.47}As$.

Accordingly, for PD_{80}, the corresponding graded bandgap absorption layer is constructed by replacing the original $In_{0.53}Ga_{0.47}As$ absorption layer [6] with a linear compositionally-graded $In_{0.62}Ga_{0.38}As_{0.82}P_{0.18} \rightarrow In_{0.53}Ga_{0.47}As$ absorption layer. We assume that the depth d (in μm) is the distance from a specified point in absorption layer to the surface of the p-contact layer. Then for PD_{80}, the relation between the composition fraction x and d can be expressed as $x = 0.409d + 0.351, d \in [0.07, 0.29]$ μm. The corresponding composition fraction y can be calculated according to Eq. (2.2). To investigate the effect of the graded bandgap absorption structure, we simulated the energy band diagram and the electric field distribution in the absorption layer. Moreover, the modulation response is also performed. As illustrated in the following, the simulation results of the device which employs a graded bandgap absorption layer structure are compared with the corresponding results of the original device, for which the bandgap of the InGaAs absorption layer is non-graded [6].

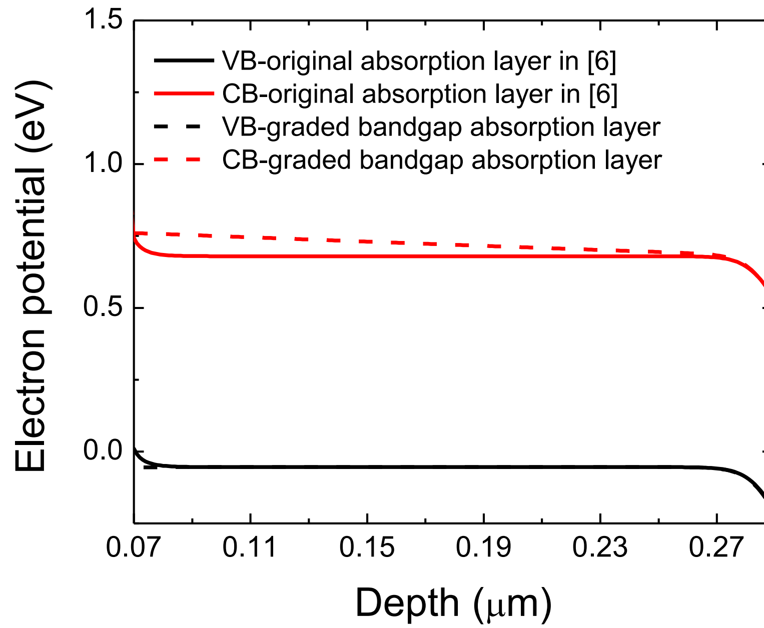

Figure 3.3 Band diagram of the absorption layer of PD_{80} with original design [6] and with graded bandgap design.

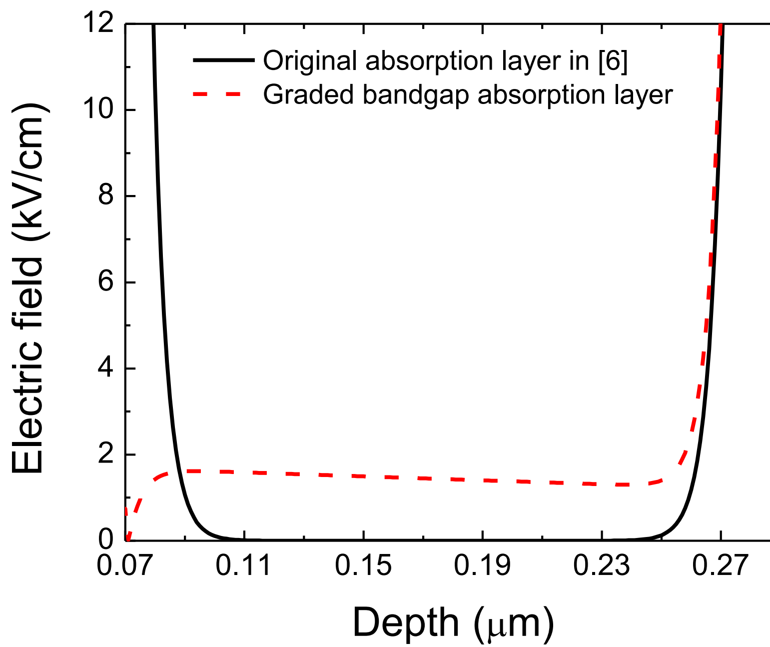

Figure 3.4 Distribution of electric field in the absorption layer of PD_{80} with original design [6] and with graded bandgap design.

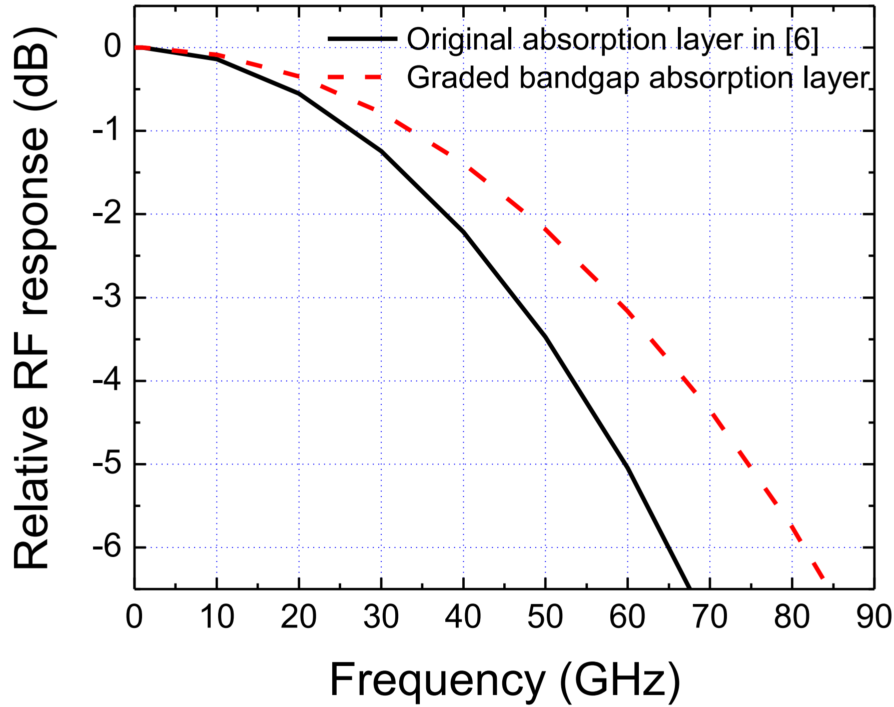

Figure 3.5 Simulated modulation response for PD_{80} with original design [6] and with graded bandgap design.

According to Fig. 3.3, showing the energy band diagram of the absorption layer (from 0.07 to 0.29 μm), we can obviously observe that a potential gradient is constructed in the conduction band by using the designed compositionally-graded $In_{0.62}Ga_{0.38}As_{0.82}P_{0.18} \rightarrow In_{0.53}Ga_{0.47}As$ absorption layer structure. Moreover, it is worth noting that there is almost no change in the valence band. Almost all of the energy gap difference ΔE_g of the designed $In_{1-x}Ga_xAs_yP_{1-y}$ absorption layer is distributed to the conduction band offset ΔE_c, which is more favorable to the electrons in absorption layer to transport from diffusion barrier side to the collection layer side. It can be seen from Fig.

3.4, as expected, the built-in electric field is enhanced when the graded bandgap absorption layer structure is introduced. For the considered UTC-PD, the electric field in the absorption layer near the blocking layer side (from ~0.08 to ~0.11 μm) is enhanced to around ~1.5 kV/cm. It is higher than the ~1 kV/cm built-in electric field which is introduced by the graded doping effect as described above. This proves that the graded bandgap structure can further accelerate the minority electrons in the absorption layer. Thereby, the electron transport time in the absorption layer can be reduced, and thus the bandwidth performance is enhanced. As can be seen from Fig. 3.5, which shows the simulated modulation responses, the 3-dB bandwidth performance is improved by using graded bandgap structure. For PD_{80}, the 3-dB bandwidth is increased from 46.25 GHz to 58.33 GHz, which leads to an improvement of 26.1%. It is higher than the improvement achieved by using graded doping absorption layer. This is due to the higher introduced electric field in the front part of absorption layer.

3.3 Optimization of graded structure

If the electric field is introduced in absorption layer, carrier drift, as well as diffusion, occurs. It is well known that, at low electric field, the carriers move at the drift velocity v_d, which can be expressed as $v_d = \mu E$, where E is the electric field, μ is the carrier

mobility. While, at higher electric field, the carrier energy obtained from electric field is transferred to lattice rather than increasing the velocity. As can been seen from Fig. 2.3 [40], for InGaAs and InP, the electron velocity no longer increases proportionally with increasing electric field. And after a peak value, drift velocity decreases as the electric field goes higher. Finally, drift velocity tends to saturation. On the other hand, for carrier diffusion, the diffusion coefficient D indicates how well the carrier moves due to the density gradient. The relation between diffusion coefficient and carrier mobility is given by $D = \frac{kT}{q}\mu$. Consequently, the optimum performance can be obtained if appropriate electric field E and carrier mobility μ are found.

As discussed in the previous section, the graded structure, including graded doping and graded bandgap structure, mainly contributes to increase the built-in electric field E in the absorption layer. In addition, the graded structure also has impacts on carrier mobility μ. This can be explained as follows. For the graded doping method, the doping concentration will be affected, and the carrier mobility is the function of the doping concentration. As the doping concentration increases, the ionized impurity scattering mechanism will lead to the carrier mobility μ decrease. On the other hand, the carrier mobility can be expressed as $\mu = \frac{q\tau}{m^*}$, where q is the elementary charge, τ is the mean time between collisions and m* is the carrier effective mass. In the $In_{1-x}Ga_xAs_yP_{1-y}$

system, the effective mass of carrier depends on the composition fractions x and y. Thereby, for the graded bandgap method, the variation of the composition fractions has influence on the effective mass m*, and thus the carrier mobility is affected. As the composition fraction y increases, both the hole and electron effective masses decrease [33][46], which implies that the carrier mobility will increase. According to the above analysis, we can optimize the graded structure to find the optimal electric field E and carrier mobility μ to enhance the carrier transport velocity.

It is found that, as the doping concentration gradient or energy bandgap gradient becomes larger, the introduced built-in electric field increases. Thus, in order to create higher built-in electric field which leads to higher drift velocity, we need to construct larger slope of the gradient. The slope can be increased if we shorten the absorption layer or construct larger potential and doping difference. However, shortening the absorption layer leads to lower responsivity. This is because, for the studied UTC-PD, the absorption layer thickness is much shorter than the penetration depth [47], and the responsivity scales down with reduced absorption thickness. On the other hand, the potential difference can not be improved due to the limitation of the second condition as mentioned above. The doping difference can be enhanced by increasing the doping concentration near the diffusion barrier side or decreasing the doping concentration near collector side.

While, higher doping concentration results in lower carrier mobility and lower carrier lifetime, which lead to the responsivity and bandwidth drop. Reducing the doping concentration near the collector side does not have much impact on the slope, due to its small order of magnitude. Therefore, these methods are inappropriate. As can be seen from Fig. 3.1 and Fig. 3.4, the improvement of the built-in electric field in the absorption layer near the space layer side (from 0.26 to 0.29 μm) is not significant by using the graded structure. Moreover, according to the comparison between Fig. 3.1 and Fig. 3.4, as well as the corresponding 3-dB bandwidth, it is found that higher electric field in the front part of absorption layer leads to better 3-dB bandwidth performance. Thus, as indicated in Fig. 3.6, a feasible way to enhance the built-in electric field is to use a partially graded structure. The absorption layer thickness W_A is maintained unchanged, and only the graded structure thickness W_G is shortened (In the following sections, W_{GD} is the thickness of graded doping region, W_{GB} is the thickness of graded bandgap region). Thereby, the slope of the gradient can be enlarged to create a high electric field in the front part of absorption layer. Meanwhile, the required conditions, for the design of energy band, can be satisfied. In the following, we will investigate the modified graded doping and graded bandgap structure respectively. For PD_{80}, the absorption layer

thickness W_A is 0.22 μm, which starts from 0.07 to 0.29 μm, since we set the top of the p-contact layer as the origin of the depth.

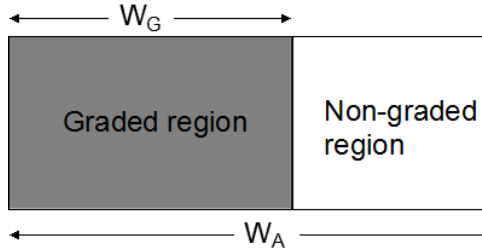

Figure 3.6 Schematic diagram of the graded structure optimization method. The left side is the blocking layer side.

3.3.1 Optimization of graded doping structure

In order to find the optimum graded doping structure, we keep the absorption layer thickness and other structure parameters unchanged, and only shrink the thickness of the graded doping region W_{GD}. As plotted in Fig. 3.7, to investigate the effect of the modified graded doping structure, the relation between the 3-dB bandwidth and the thickness of graded doping region W_{GD} is simulated. In addition, as shown in Fig. 3.8 and Fig. 3.9, we compared the electric field distributions and energy band diagrams in the absorption layer (from 0.07 to 0.29 μm) between four cases, P1 (W_{GD}=0.22 μm, initial graded doping structure), P2 (W_{GD}=0.18 μm), P3 (W_{GD}=0.128 μm) and P4 (W_{GD}=0.06 μm). We can see that the 3-dB bandwidth first increases and then decreases as W_{GD} shrinks from 0.22 μm. The maximum 3-dB bandwidth occurs at P3, where W_{GD} is ~0.128 μm. This result can be

explained as follows. The slope of the doping concentration gradient increases as W_{GD} shrinks from 0.22 μm. At first, as can be seen from Fig. 3.8, the built-in electric field in the graded doping region is enhanced, such as case P2. At the same time, the average doping concentration in the absorption layer decreases as W_{GD} shrinks. It implies that the carrier mobility is improved. Thereby, the carrier drift velocity increases. Additionally, as shown in Fig. 3.9, the depletion region in the absorption layer becomes wider since the doping concentration drops. In this depletion region, the carriers drift rather than diffusion. Besides, the junction capacitor is reduced as a result of the wider depletion region. Because of all these reasons, the carrier transit time and RC-time constant will be reduced. Therefore, the 3-dB bandwidth performance is improved. However, as the graded doping region further shrinks, the interface between the graded and non-graded region will be gradually away from the high electric field region near the space layer side, which in fact is the depletion region in the absorption layer. When this interface is out of the depletion region, the electric field in the non-graded doping region near this interface likely to be low, since the built-in electric field enhancement only occurs in the graded doping region. Thus, as can be observed in Fig. 3.8, due to the trade-off between the increased carrier mobility and the decreased electric field, the 3-dB bandwidth first increases to the maximum case P3, in which the built-in electric field in the non-graded

region near the interface (from ~0.198 to ~0.24 μm) is lower than that in case P2. Then, the bandwidth starts to drop. On the other hand, as illustrated in Fig. 2.3 [40], when the built-in electric field in the graded doping region becomes further higher, the carrier drift velocity in this region may decrease from the peak value to saturation, due to the reduction of carrier mobility. Consequently, the 3-dB bandwidth performance becomes worse. For example, case P4, although the built-in electric field near the blocking layer side (from 0.07 to ~0.135 μm), which is generated by large doping gradient, is the highest, the bandwidth performance is limited by the low electric field in the non-graded doping region. For PD_{80}, as can be seen from Fig. 3.7, the optimal thickness of graded doping region is found to be ~0.128 μm. The 3-dB bandwidth improvement, from P1 55.25 GHz to P3 60.67 GHz, is 9.8%.

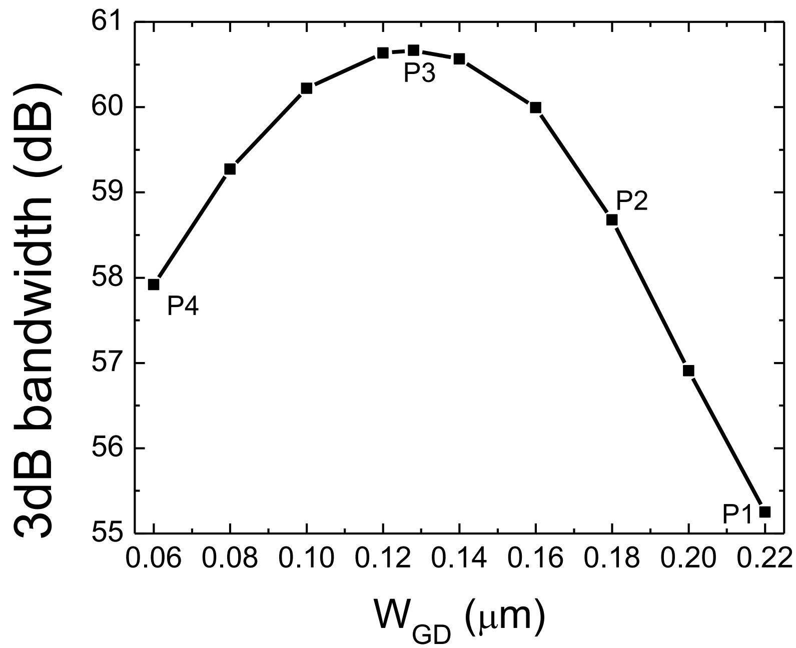

Figure 3.7 Simulated 3-dB bandwidth versus W_{GD}.

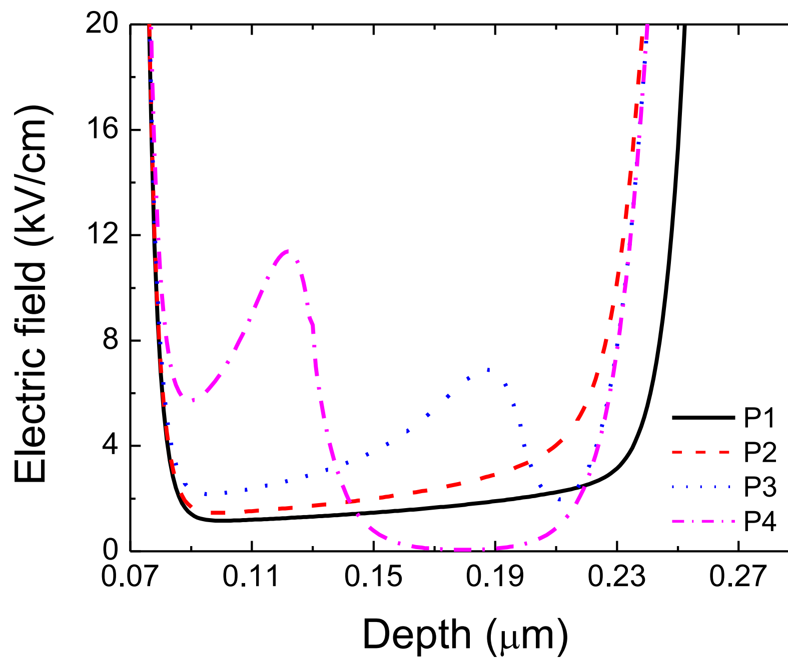

Figure 3.8 Distribution of electric field in the absorption layer versus depth for the four cases marked in Fig. 3.7.

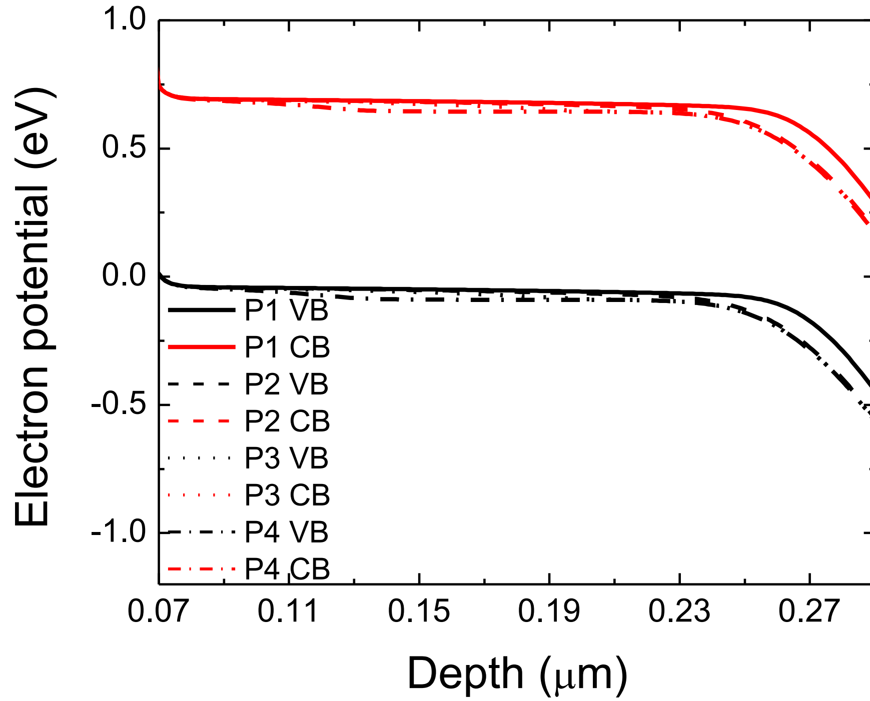

Figure 3.9 Band diagram of the absorption layer versus depth for the four cases.

3.3.2 Optimization of graded bandgap structure

Similarly, to optimize the graded bandgap structure, we keep the absorption layer thickness and other structure parameters unchanged, and only shrink the thickness of the graded bandgap region W_{GB}. As illustrated in Fig. 3.10, the effect of the modified graded bandgap structure is investigated by simulating the relation between the 3-dB bandwidth and the thickness of graded doping region W_{GB}. Moreover, as shown in Fig. 3.11 and Fig. 3.12, we compared the electric field distributions and energy band diagrams in the absorption layer (from 0.07 to 0.29 μm) between four cases, P1 (W_{GB}=0.22 μm, initial

graded bandgap structure), P2 (W_{GB}=0.20 μm), P3 (W_{GB}=0.18 μm) and P4 (W_{GB}=0.14 μm). According to Fig. 3.10, as expected, the 3-dB bandwidth first increases and then decreases as W_{GB} shrinks from 0.22 μm. The maximum 3-dB bandwidth occurs at P3, where W_{GB} is ~0.18 μm. This result can be understood as follows. As the graded bandgap region shrinks from 0.22 μm, the slope of the potential gradient in conduction band increases, which can be seen from Fig. 3.12. Correspondingly, such as the case P2 plotted in Fig. 3.11, the built-in electric field in the graded bandgap region is enhanced. On the other hand, the average composition fraction y of the $In_{1-x}Ga_xAs_yP_{1-y}$ system in absorption layer becomes larger as W_{GB} shrinks. Thus, both the effective masses of hole and electron decrease [33], which implies that the carrier mobility is improved, since the carrier mobility is inversely proportional to the carrier effective mass. Thereby, the carrier drift velocity increases, which leads to less carrier transit time. Consequently, the 3-dB bandwidth is enhanced. However, as the built-in electric field becomes further higher, the carrier drift velocity may decrease from the peak value, and the carrier mobility starts to drop. In addition, as the graded bandgap region shrinks, similar to the case of graded doping, the interface between the graded and non-graded region will be gradually away from the high electric field depletion region in the absorption layer near space layer side. Because the built-in electric field can be only constructed in the graded

bandgap region, when the interface is out of the depletion region, the electric field in the non-graded bandgap region near this interface drops significantly. Such as case P4, although the built-in electric field near the blocking layer side (from 0.07 to ~0.20 μm), which is created by the large bandgap gradient, is the highest, the carrier cannot be accelerated effectively due to the low electric field (from ~0.21 to ~0.25 μm) in the non-graded bandgap region. Therefore, the performance of 3-dB bandwidth declines. It is noted that, as can be seen from Fig. 3.11, although the maximum improvement of 3-dB bandwidth occurs at P3, its built-in electric field in the non-graded region near the interface (from 0.24 to 0.26 μm) is lower than that in case P2. This is due to the trade-off between the increased carrier mobility and the decreased electric field. For PD_{80}, as shown in Fig. 3.10, the optimal thickness of graded bandgap region is ~0.18 μm. The 3-dB bandwidth is improved from P1 58.33 GHz to P3 59.07 GHz, an improvement of 1.3%, which is not as significant as the improvement of optimized graded doping structure. This is because the optimized graded doping structure leads to a wider depletion region in the absorption layer.

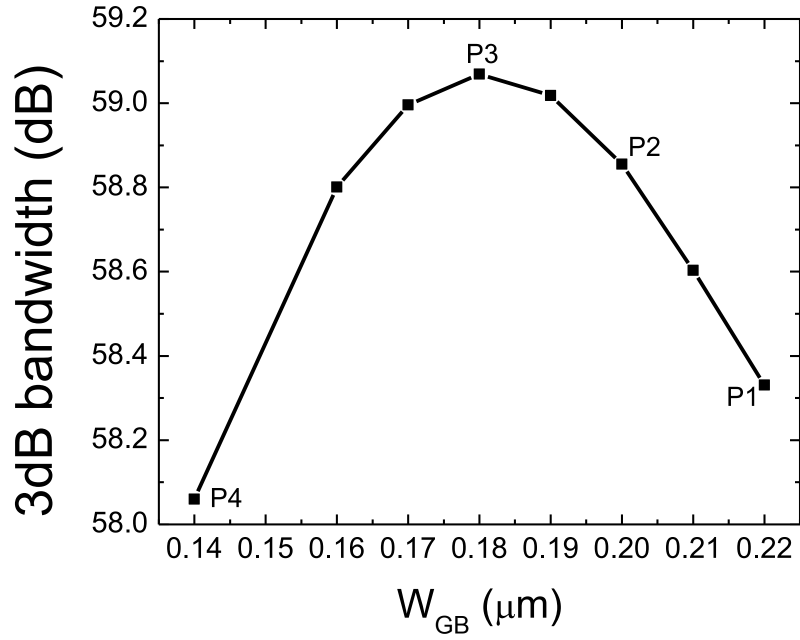

Figure 3.10 Simulated 3-dB bandwidth versus W_{GB}.

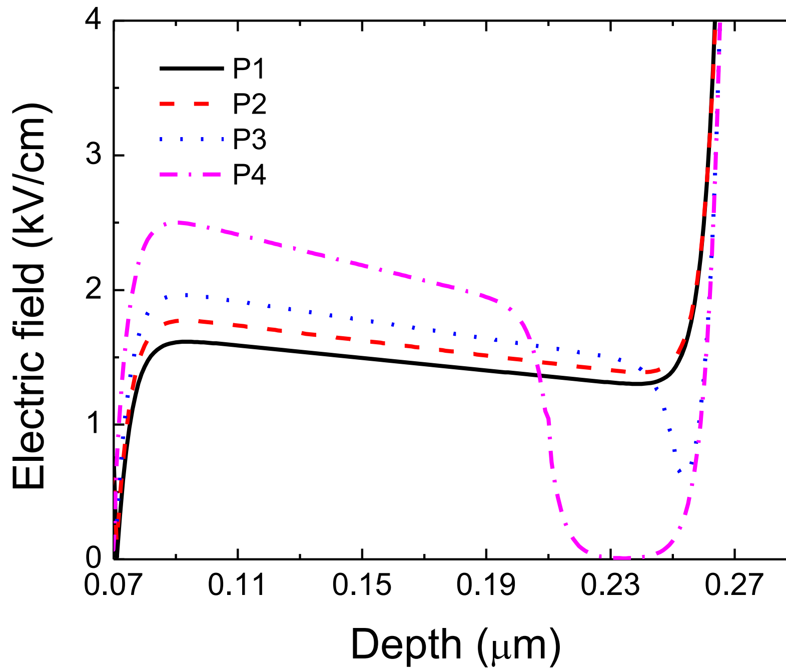

Figure 3.11 Distribution of electric field in the absorption layer versus depth for the four cases marked in Fig. 3.10.

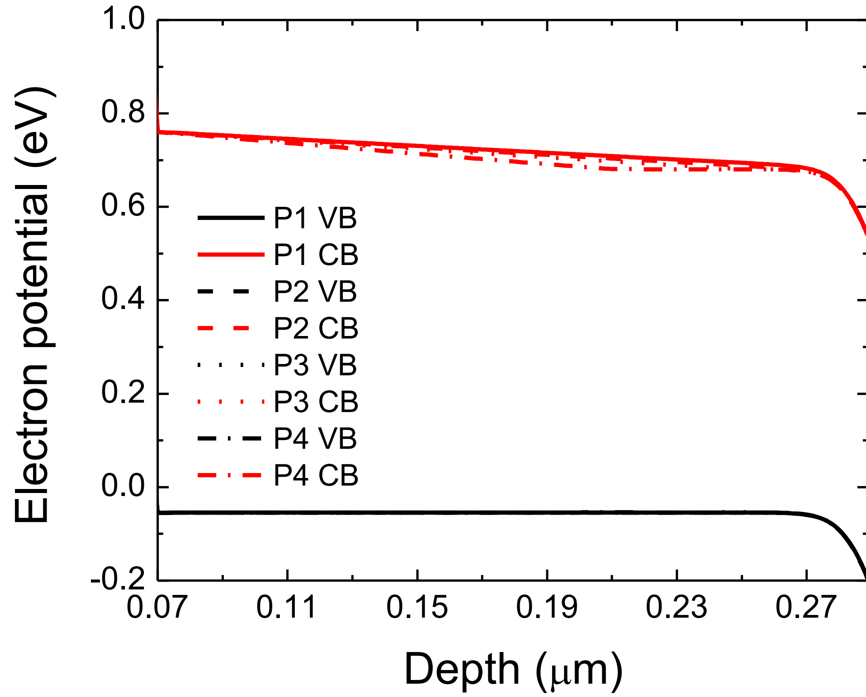

Figure 3.12 Band diagram of the absorption layer versus depth for the four cases.

3.4 Combined graded absorption layer structure

As described above, both the graded doping and graded bandgap structure can construct a built-in electric field and the performance can be further improved by structure optimization. In the following, we investigate the combined effect by using both optimized graded doping and optimized graded bandgap structure simultaneously. As can be seen from Fig. 3.13, the combined built-in electric field introduced by the combined graded absorption layer structure is further enhanced. The combined built-in electric field is larger than ~4 kV/cm, which is nearly the sum of the built-in electric fields introduced

by graded doping structure and graded bandgap structure. Compared to the original absorption layer structure (uniformly doped and non-graded bandgap InGaAs absorption layer [6]), we can see that the built-in electric field is significantly increased by the graded structure. Specially, the enormous growth of the built-in electric field near the space layer side, from 0.23 to 0.27 μm, is caused by the depletion region in the absorption layer. As plotted in Fig. 3.14, we compared the modulation responses of devices for the four absorption layer structures. We can observe that, compared to the original structure [6], the 3-dB bandwidth is successfully increased from 46.25 GHz to 64.48 GHz by using combined graded absorption layer structure, and the improvement is 39.4%.

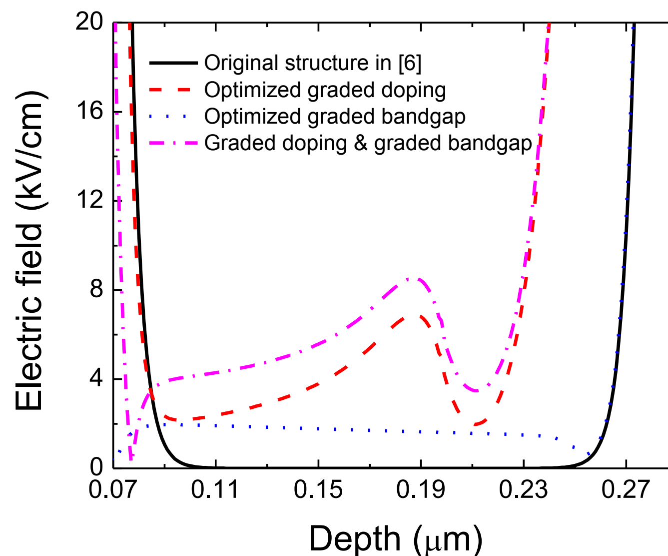

Figure 3.13 Distribution of electric field in the absorption layer for PD_{80} with different absorption layer structure.

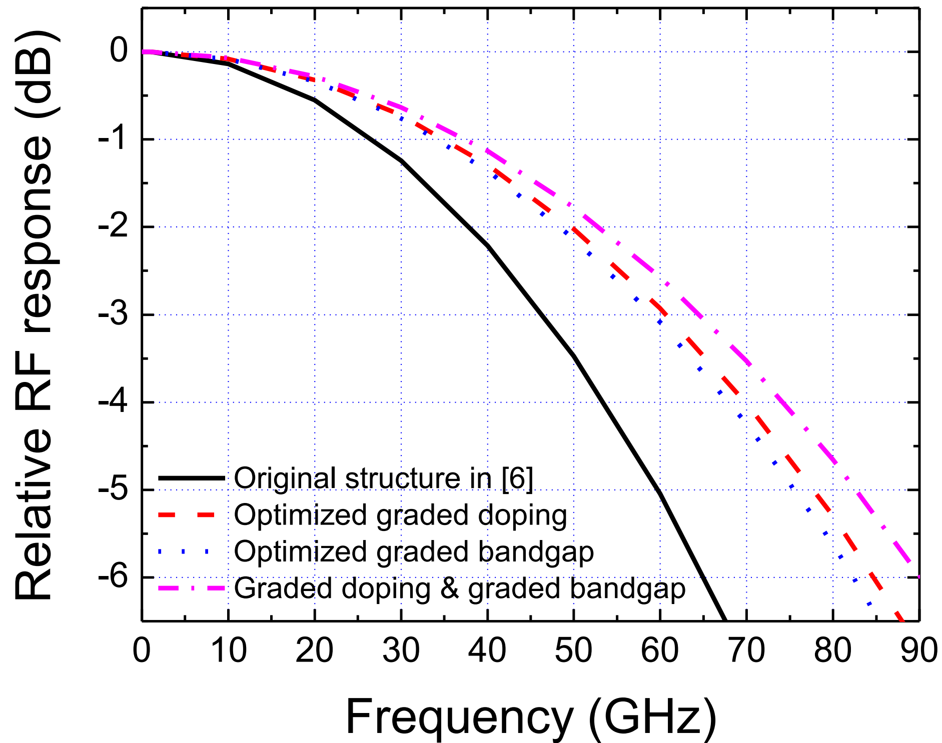

Figure 3.14 Simulated modulation response of PD_{80} with different absorption layer structure.

3.5 Summary

The high-speed performance can be improved by introducing an appropriate built-in electric field in the absorption layer. In this chapter, we first confirmed that, by incorporating a linearly graded doping profile in the absorption layer, which has been a widely used method, the bandwidth can be enhanced. The 3-dB bandwidth increases from original 46.25 GHz to 55.25 GHz. Then, we proposed a graded bandgap absorption layer. According to the simulation results, it is found that a built-in electric field in the

absorption layer can be constructed by applying the graded bandgap structure. This method leads to a 3-dB bandwidth of 58.33 GHz. The better performance is caused by the higher introduced built-in electric field in the front part of absorption layer. Furthermore, by using partially graded absorption layer structure, these two methods are optimized respectively. By the optimization of graded doping structure, the 3-dB bandwidth raised to 60.67 GHz. On the other hand, the bandwidth performance of the optimum graded bandgap structure is 59.07 GHz. Since the optimized graded doping structure leads to a wider depletion region in the absorption layer, the bandwidth performance improvement is greater. Finally, the bandwidth performance of the UTC-PD with combined graded absorption layer structure is investigated. A 3-dB bandwidth of 64.48 GHz is predicted, the improvement is 39.4%. And it is found that, the combined introduced built-in electric field is nearly the sum of the built-in electric fields created by graded doping structure and graded bandgap structure.

Chapter 4 Investigation and Design of Collection Layer Doping Profile

It is well known that the space-charge effect is the primary mechanism which causes saturation at high current level in photodiodes [48]. At high optical injection level, the electric field in the depletion region will redistribute due to the space-charge effect, which may result in reduced electron velocity and degradation of the bandwidth and output power. It has been suggested that the space-charge suppression of the electric field could be compensated by a fixed distribution of background dopants [49]. Thus, the doping concentration in the depleted InP collection layer is very important, since it is directly relevant to the saturation performance. By appropriately doping the depletion region, the electric field distribution can be adjusted. Thereby, the space-charge effect can be reduced, and the saturation performance can be improved effectively. In addition, there is another advantage by using the technique of charge compensation. Unlike the method, which relieves the space-charge effect by increasing the bias voltage, charge compensation method will not lead to thermal effect. In the following, the space-charge effect in the collector and the technique of charge compensation with various doping levels are first investigated by analyzing the energy band profile and the distribution of

the electric field. According to the analysis, we proposed a new collection layer design based on linear doping profile. Furthermore, it is found that the saturation performance can be further improved by using Gaussian doping profile in the collection layer.

4.1 Space-charge effect in UTC-PDs

In order to analyze the space-charge effect, we investigated electron concentration profiles, the distributions of electric field in the collection layer, and also the energy band structures at different optical injection levels. As shown in Fig. 4.1, at high light intensity, the distribution of electron concentration in the absorption layer (from 0.07 to 0.29 μm) is different from the cases of low optical injection levels. There is a significant difference in the electron concentration profile when the light intensity is higher than $2x10^6$ W/cm^2. The electron concentration near the absorption layer and space layer interface (from ~0.25 to 0.29 μm) is higher than that near the blocking layer and absorption layer interface (from 0.07 to ~0.11 μm). This implies that, as the optical power goes higher, the electron starts to accumulate near the absorption layer and space layer interface. Then, as the light intensity further increases, more electrons will be accumulated in the absorption layer due to the fact that the electron cannot effectively transport from the absorption layer to the collection layer. This can be seen from the case in Fig. 4.1, in which the light

intensity is 2.25×10^6 W/cm^2. The accumulation of electrons in the absorption layer greatly increases the carrier recombination probability, which leads to the responsivity reduction. Moreover, the higher concentration of electrons in the absorption layer near the space layer end hinders the diffusion of electrons from the absorption layer to the collection layer to some extent and shows a tendency toward saturation. In addition, the accumulated electrons will introduce an electric field which is reverse to the applied electric field. This will cause adverse effect on the internal electric field. It can be seen from the distribution of electric field in Fig. 4.2, as the optical power raises, the electric field drops in the space layer (from 0.30 to 0.32 μm), cliff layer (from 0.32 to 0.327 μm), and also the input end of collection layer (from 0.327 to ~0.437 μm). On the other hand, it is illustrated in Fig. 4.3, as the light intensity increases, the excess carrier bends the energy bands. The energy bands in the collection layer near the absorption end (from 0.327 to ~0.437 μm) become flatter and those near the subcollection end (from ~0.437 to 0.59 μm) become steeper. This indicates the corresponding changes of the electric field in the collection layer (from 0.327 to 0.59 μm). As shown in Fig. 4.2, when the optical injection level increases, the electric field near the absorption end (from 0.327 to ~0.437 μm) is reduced and it increases near the subcollection end (from ~0.437 to 0.59 μm). These simulation results are in agreement with the report of T. Ishibashi et al. [6]. If the

electric field at the collection layer input end becomes smaller than a critical value, the electrons drift velocity will be considerably reduced, which affects the device's modulation response and leads to saturation. The critical value of electric field for InP is about 10 kV/cm [50]. Accordingly, we can conclude that the space-charge effect mainly occurs in the collection layer near the absorption layer end. The corresponding reduction of electric field at this side leads to output current saturation.

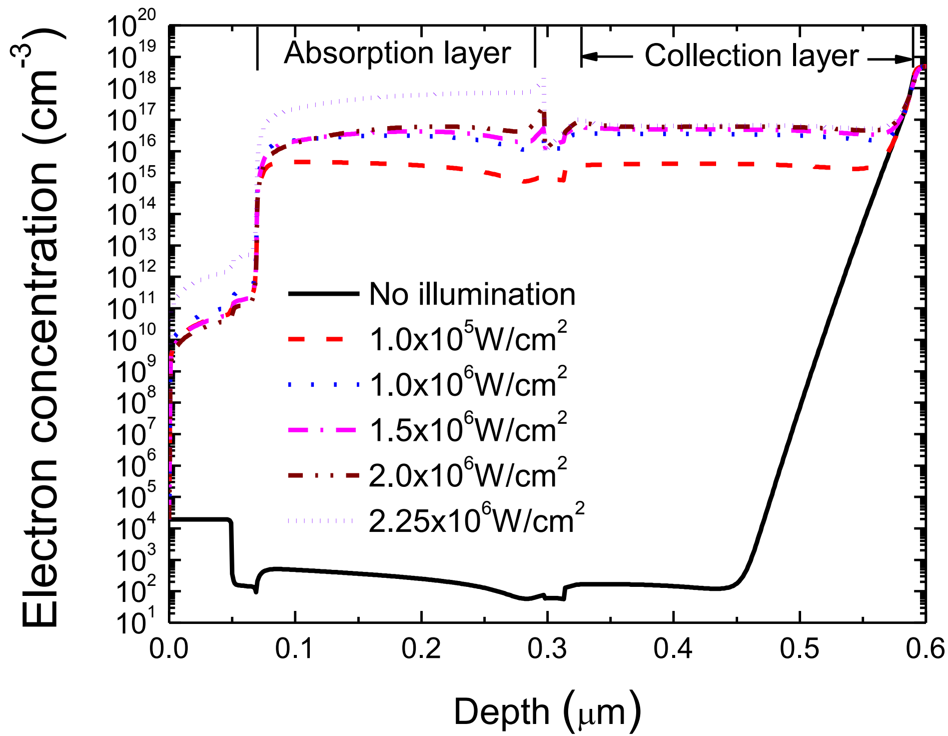

Figure 4.1 Electron concentration profiles of PD_{80} at various light intensity levels.

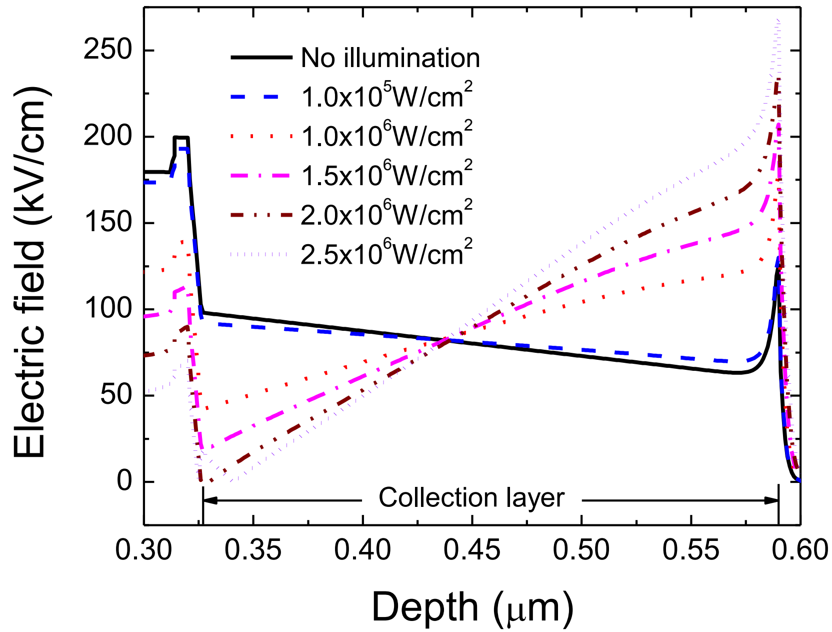

Figure 4.2 Distribution of electric field in the depletion region of PD_{80} at various light intensity levels.

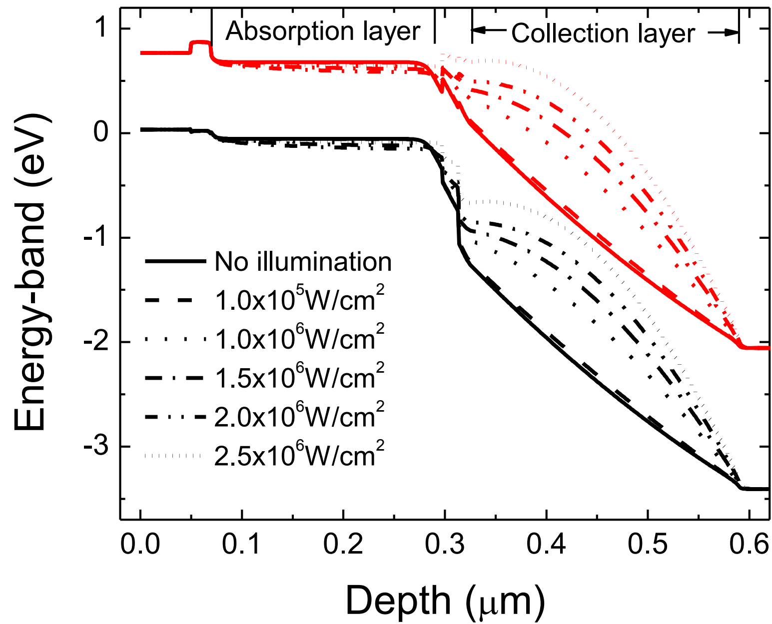

Figure 4.3 Band diagram of PD_{80} at various light intensity levels.

4.2 Charge compensation by using uniform doping profile in the collector

As mentioned above, the space-charge effect can be reduced by using the technique of charge compensation. N. Li et al. [51] have demonstrated that by using a uniformly n-doped collection layer, the space-charge effect is reduced, and thus the saturation performance is improved. We will analyze how this method works. First of all, we study the effect of different collection layer doping concentration on photocurrent. As has been reported in [52]-[53], for n-type InP, when the doping concentration is below $1x10^{17}$ cm^{-3}, the electron mobility and the overshoot velocity are almost the same as those in un-doped material. Thus, the photocurrent is simulated under DC illumination with various collection layer doping concentrations from 0 (non-intentionally doping (n.i.d.)) to $5x10^{16}$ cm^{-3}, in which $1x10^{16}$ cm^{-3} is used in the original design [6] (as shown in Table 2.1) for charge compensation. It can be seen from Fig. 4.4, for different collection layer doping concentration, the photocurrent first increases linearly, then tends to saturation at high optical injection levels as the light intensity increases. The slope indicates the optical responsivity. We can see that, due to the space-charge effect, the responsivity decreases when the optical power is high enough. Moreover, it is shown that, as the collection layer

doping concentration goes higher, the DC saturation current increases. This implies that higher average doping level in the collection layer may lead to better saturation performance. According to the distribution of electric field in the collection layer (from 0.327 to 0.59 μm) without optical injection and at high optical injection level (the light intensity is $2x10^6$ W/cm^2), which is shown in Fig. 4.5 and Fig. 4.6, we can see that the saturation current is improved because of the increased electric field in the collection layer near the absorption layer end (from 0.327 to ~0.437 μm). However, as seen in Fig. 4.7, when the doping concentration is high enough, the energy bands in the collection layer near the subcollection end (from ~0.52 to 0.59 μm) become flatter. This implies that the collection layer cannot be completely depleted at normal device operation bias voltage. As the depletion region shrinks, it cannot extend to the InP subcollection layer, which leads to higher junction capacitance and series resistance. The electrons in the collection layer cannot be rapidly swept into the subcollection layer to form the photocurrent. Therefore, the bandwidth performance degradation occurs at high collection layer doping concentration. Although we can adopt a higher bias voltage to fully deplete the collection layer and also reduce the space-charge effect, the heat power will increase and thus leads to device thermal failure. Consequently, for the considered UTC-PD, there is a proper uniform doping concentration range to obtain better

performance. It is found to be around $2x10^{16}$ cm^{-3} to $3x10^{16}$ cm^{-3}. As plotted in Fig. 4.8, which is obtained from the modulation response, we investigated the variation of 3-dB bandwidth performance with increasing average photocurrent for different uniform doping levels. Among them, the uniform doping level of $1x10^{16}$ cm^{-3} is the original design [6]. We can observe that, for each case, 3-dB bandwidth first increases with the injection power, then decreases due to output saturation. The self-induced electric field in the absorption layer has explained the increase of bandwidth [6]. Moreover, it is shown that, as analyzed above, bandwidth decreases with increasing doping concentration. While, since the saturation performance is improved by increasing doping concentration, the degradation of 3-dB bandwidth occurs at higher photocurrent. We found that, for PD_{80}, the appropriate uniform doping concentration in the collection layer is $2x10^{16}$ cm^{-3}. Comparing this case with the case of $1x10^{16}$ cm^{-3}, which is the original design [6], the saturation current is enhanced and the bandwidth is slightly reduced. In the following sections, the UTC-PD, in which the collection layer is uniformly doped to $2x10^{16}$ cm^{-3}, is used for comparison.

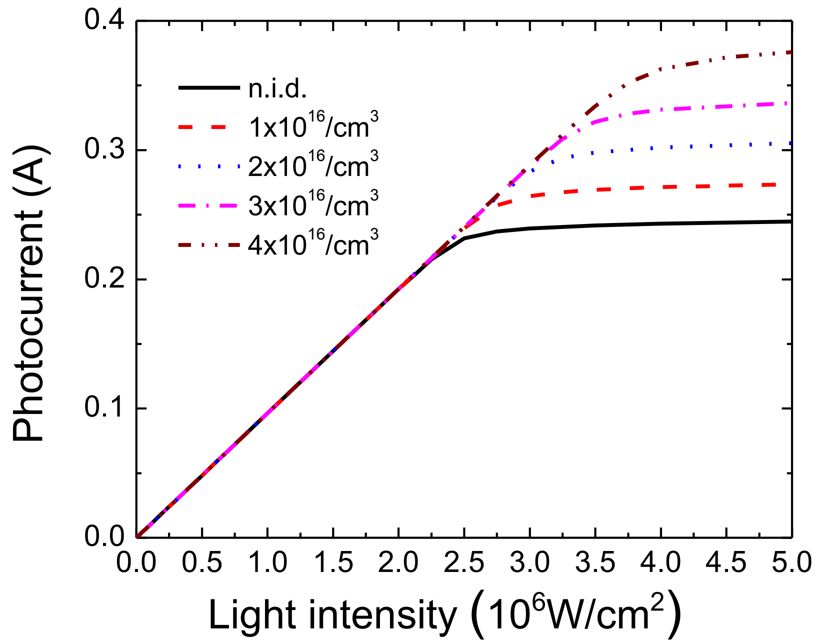

Figure 4.4 Simulated DC photocurrent versus light intensity for PD_{80} at various collector doping levels.

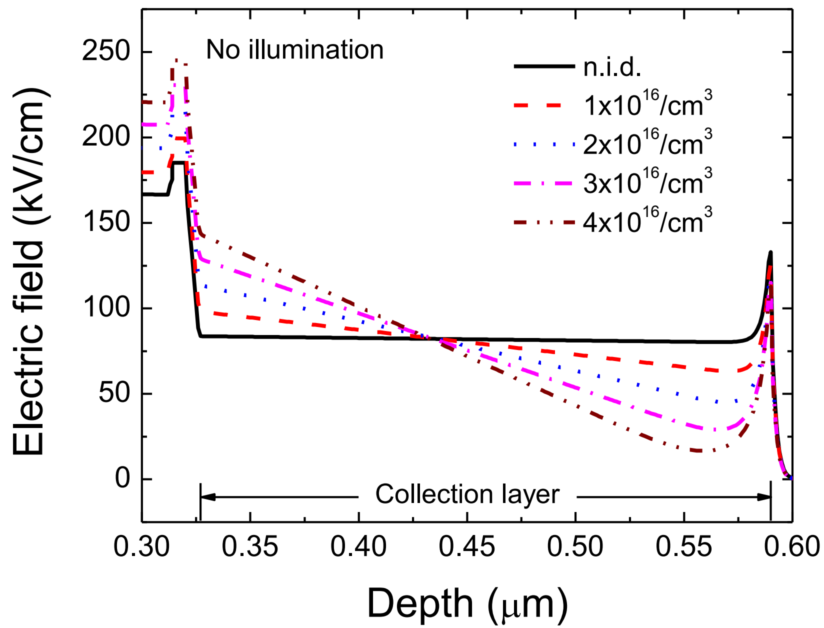

Figure 4.5 Distribution of electric field in the depletion region of PD_{80} at various collector doping levels without light injection.

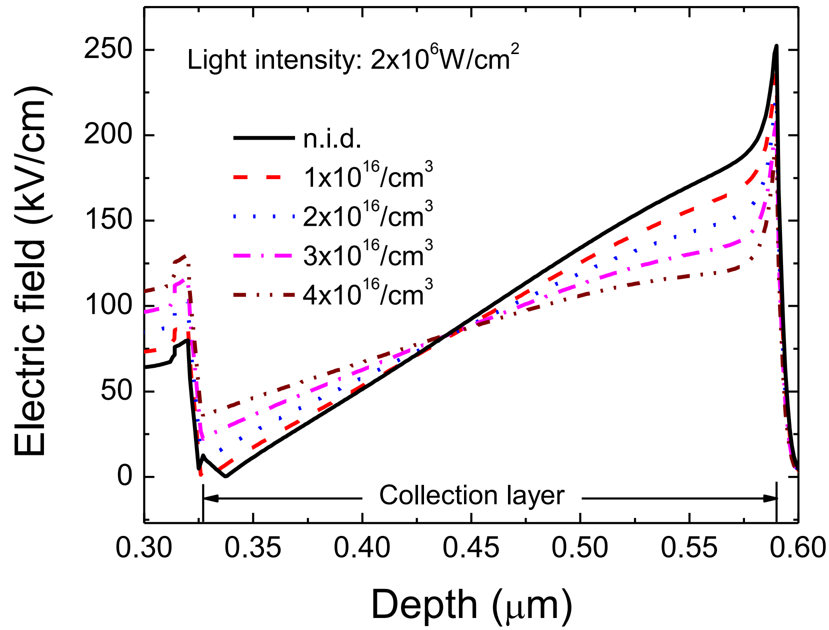

Figure 4.6 Distribution of electric field in the depletion region of PD_{80} at various collector doping levels under $2x10^6$ W/cm^2 light injection.

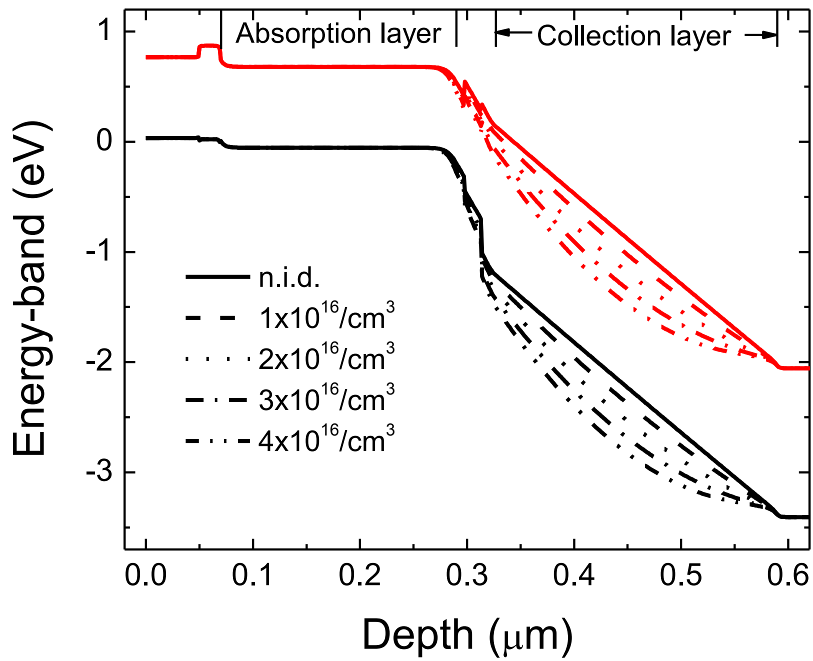

Figure 4.7 Band diagram of PD_{80} at various collector doping levels.

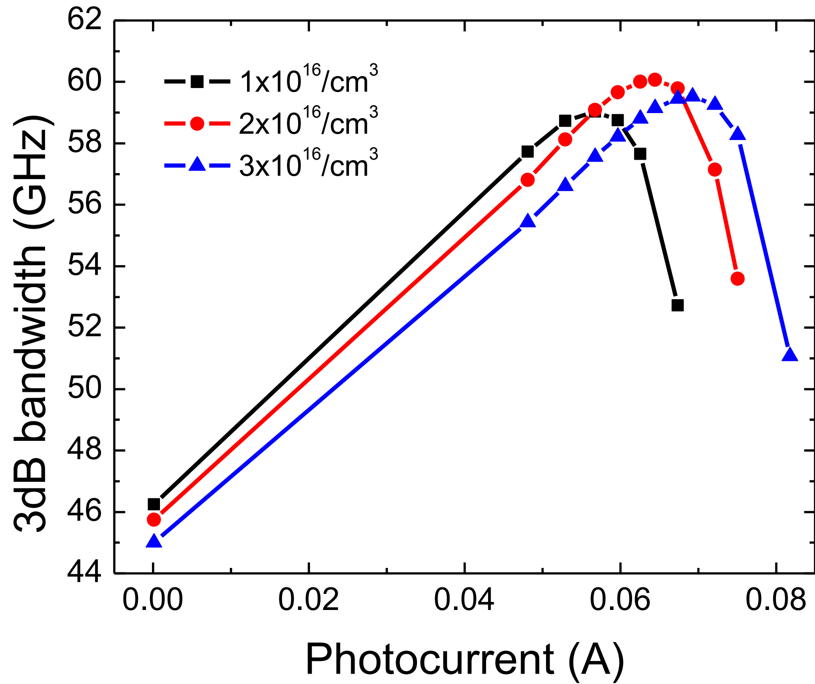

Figure 4.8 Simulated 3-dB bandwidth versus photocurrent for PD_{80} with different uniform doping level in the collection layer.

4.3 Design of collection layer based on linear doping profile

According to the above analysis, the space-charge effect mainly occurs in the collection layer near the absorption layer end. The saturation performance is primarily limited by the low electric field near this end under high optical injection. Thus, we need to focus on increasing the electric field in this region. The electric field distribution in the collection layer can be adjusted by using the technique of charge compensation. Therefore, the electric field in that region can be improved if the collection layer is doped

appropriately. And also the saturation performance can be further improved. As shown in Fig. 4.5 and Fig. 4.6, the electric field in the collection layer near the absorption end (from 0.327 to ~0.437 μm) is enhanced as the doping concentration increases. While the electric field in the collection layer near the subcollection layer end (from ~0.437 to 0.59 μm) is opposite, it decreases as the doping concentration increases. Thereby, in the collection layer, we need to highly dope the absorption layer side and lightly dope the subcollection side to improve the distribution of electric field. Consequently, we prefer to use a linear doping profile instead of the uniform doping profile.

4.3.1 Linearly doped collection layer design

We assume that the doping concentration in the collection layer changes linearly from N_1 to N_2, corresponding to the absorption layer side and the subcollection layer side respectively. In order to reasonably compare the saturation performance between the device with linearly doped collection layer and the device with uniformly doped collection layer, other conditions should keep the same. Moreover, the average doping concentration of linear doping, which is $(N_1+N_2)/2$, should be the same as the uniform doping concentration N_0. This is because, as analyzed previously, different average doping concentration in the collection layer leads to different saturation performance.

Normally, the saturation current increases with higher average doping concentration. As mentioned above, for the considered UTC-PD, which is used for comparison, the uniform doping concentration in the collection layer is $N_0=2\text{x}10^{16}$ cm^{-3}. In order to construct a large gradient and dope the collection input end as high as possible, we assume that $N_2=0$. Then, the corresponding concentration in the linearly doped collection layer should change from $N_1=4\text{x}10^{16}$ cm^{-3} to 0. The effect of changing the doping profile in the collection layer is to modify the distribution of electric field. It can be seen from Fig. 4.9, under high light intensity, the electric field in the space layer (from 0.3 to 0.32 μm), cliff layer (from 0.32 to 0.327 μm) and the input end of collection layer (from 0.327 to ~0.36 μm) is improved by using linear doping profile. Consequently, the light intensity can be further increased until the electric field reaches the critical value, at which the saturation occurs. On the other hand, the higher electric field in these regions helps to accelerate the electrons. Thus, there are less electrons trapped in the interface barriers between these regions. As shown in Fig. 4.10, at the light intensity of $2.4\text{x}10^6$ W/cm^2, for the device with uniformly doped collection layer, the electron is accumulated in the absorption layer (from 0.07 to 0.29 μm), since the electron concentration in the absorption layer is higher than that in the space layer (from 0.29 to 0.32 μm). While, the electron is hardly accumulated in the absorption layer when the linear doping profile is employed in the

collection layer. This implies that, for the device with linearly doped collection layer, there are more electrons swept to the subcollection layer to contribute to the photocurrent. As the light intensity further increases, more electron-hole pairs are generated and more electrons can transport to the collection layer until the electrons start to accumulate in the absorption layer, which indicates the saturation happening. Hence, the saturation performance is improved. By using physics-based modeling, the DC photocurrent as a function of the light intensity is obtained, as plotted in Fig. 4.11. Moreover, in order to facilitate the comparison, we define the current at the inflection point of the linear fitting polyline as the saturation current. We can see that, by using linear doping method in the collection layer, the DC saturation current is successfully increased from 296.92 mA to 314.10 mA, and the improvement is 5.8%.

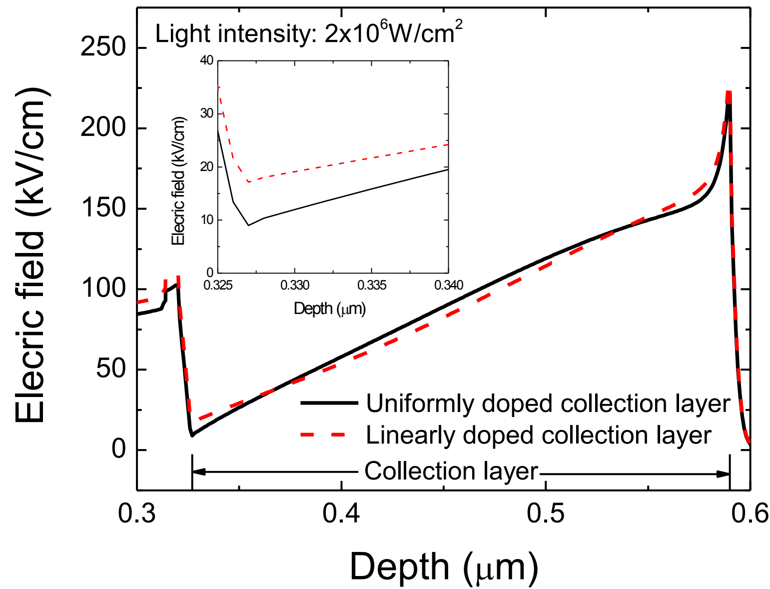

Figure 4.9 Distribution of electric field in the depletion region of the device with different collection layer structure under 2x10^{6} W/cm^{2} light injection. Inset is the enlarged view at the input end of collector.

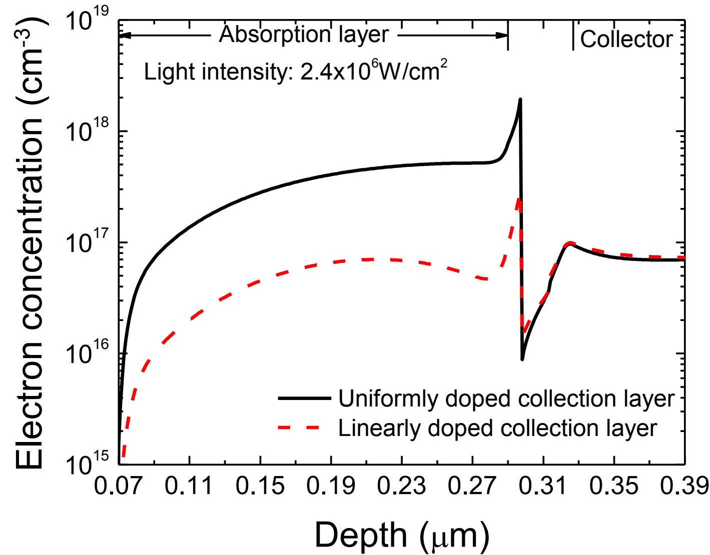

Figure 4.10 Electron concentration profiles in the absorption layer for the device with different collection layer structure under 2.4x10^{6} W/cm^{2} light injection.

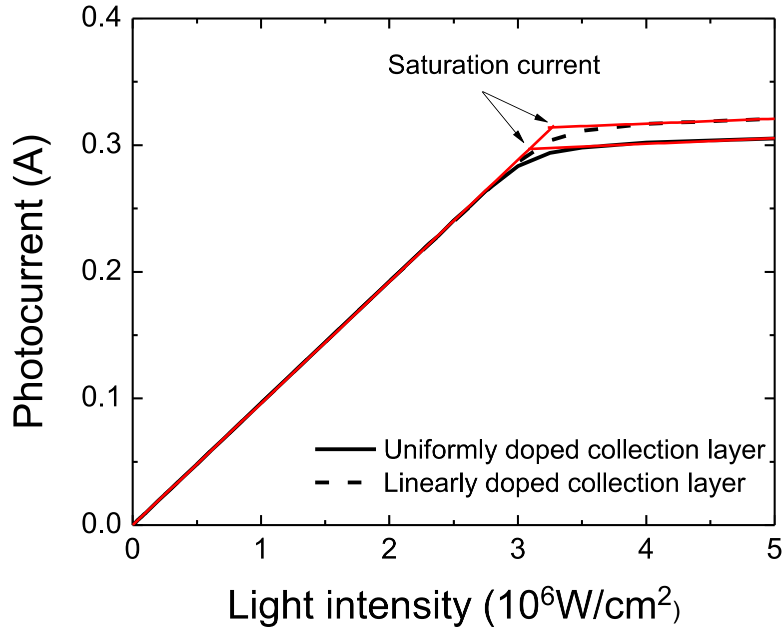

Figure 4.11 Simulated DC photocurrent versus light intensity for the device with different collection layer structure.

4.3.2 Optimization of linearly doped collection layer

As introduced previously, the saturation performance is mainly limited by the low electric field in the collection layer near the absorption layer end under high optical levels. The electric field near this end can be raised by increasing the doping concentration. Thus, the saturation performance can be further improved by increasing the doping concentration near this end. For the linear doping profile as we mentioned above, we should increase the value of N_1. However, if we only increase the value of N_1 and do not decrease the value of N_2, the average doping concentration will become higher. Then, the

comparison with the considered UTC-PD is not reasonable. Moreover, this may cause the collection layer that cannot be fully depleted, which results in the bandwidth degradation as explained before. Therefore, in order to maintain the average doping concentration unchanged and enhance the electric field at that side simultaneously, an effective method is to use a partially doped collection layer structure. As illustrated in Fig. 4.12, we divide the collection layer into a doped region and an undoped region. W_C is the thickness of the collection layer, W_{CD} is the thickness of the doped region. As defined above, the average doping concentration in the linearly doped region is $N_1/2$, since we assumed the value of N_2 is zero. We also define the average doping concentration in the collection layer as D. According to the definition, $D = \frac{N_1}{2} \cdot \frac{W_{CD}}{W_C}$. For the initial case, W_{CD}=W_C=263 nm and N_1=4x10^{16} cm^{-3}. Thus, D=2x10^{16} cm^{-3}. In order to find the optimized linear doping structure, we maintain the average doping concentration D unchanged, only shrink the thickness of the linear doping region W_{CD}. Since the electron mobility and the overshoot velocity may be affected by high doping concentration, the maximum value of N_1 is limited to 1x10^{17} cm^{-3}. Thereby, the ratio of W_{CD}/W_C can range from 0.4 to 1. Fig. 4.13 shows the DC saturation current, which is obtained from the DC photocurrent response to light intensity, with varying the value of W_{CD}/W_C. It can be seen that the DC saturation current first increases and then decreases as W_{CD} shrinks. We found the maximum DC

saturation current occurs at case P2, where W_{CD}/W_C is ~0.64. In addition, as shown in Fig. 4.14, we compared the distributions of electric field at the input end of collector (from 0.327 to 0.38 μm) at high light intensity ($2x10^6$ W/cm^2) between four cases, P1 (W_{CD}/W_C=1.0, N_1=$4x10^{16}$ cm^{-3}, initial linear doping profile), P2 (W_{CD}/W_C=0.64, N_1=$6.25x10^{16}$ cm^{-3}), P3 (W_{CD}/W_C=0.5, N_1=$8x10^{16}$ cm^{-3}) and P4 (W_{CD}/W_C=0.4, N_1=$1x10^{17}$ cm^{-3}). The simulation results can be explained as follows. Firstly, the value of N_1 increases as W_{CD} shrinks. Thus, there are more dopants in the collection layer near the absorption layer end for space-charge compensation. As can be seen in Fig. 4.14, the electric field at this end (~0.332 μm) is enhanced. According to the previous analysis, higher electric field at this end leads to higher saturation current, such as case P2. Then, as W_{CD} further shrinks, the electric field at this end still increases. However, for case P3, the distribution of electric field near this end (from 0.327 to 0.38 μm) becomes flatter and the average electric field in this region (from 0.327 to 0.38 μm) becomes lower. This is unfavorable to efficiently accelerate the electrons to transport through the depletion region. Therefore, the DC saturation current drops. Furthermore, when W_{CD} becomes too short, the minimum electric field appears inside the collection layer. For case P4, although the electric field in the collection layer at the absorption layer end (~0.332 μm) is the highest, the saturation performance is limited by the low electric field inside the

collection layer (~0.353 μm). Consequently, the saturation performance becomes even worse. As can be seen from Fig. 4.13, for the considered UTC-PD, the optimal thickness of linear doping region is ~168.3 μm (W_{CD}/W_C is ~0.64). After the optimization, the improvement in DC saturation current, from P1 314.10 mA to P2 318.90 mA, is 1.53%, which is not significant.

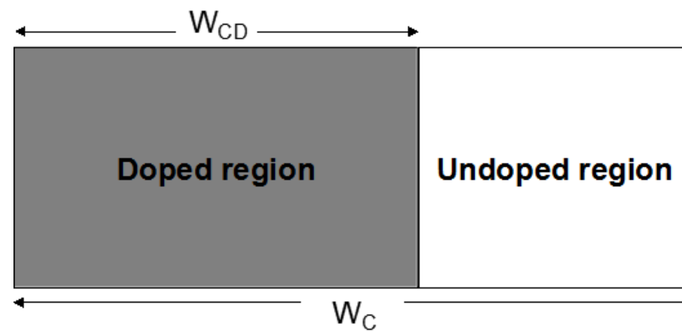

Figure 4.12 Schematic diagram of the linear doping profile optimization method. The left side is the cliff layer side.

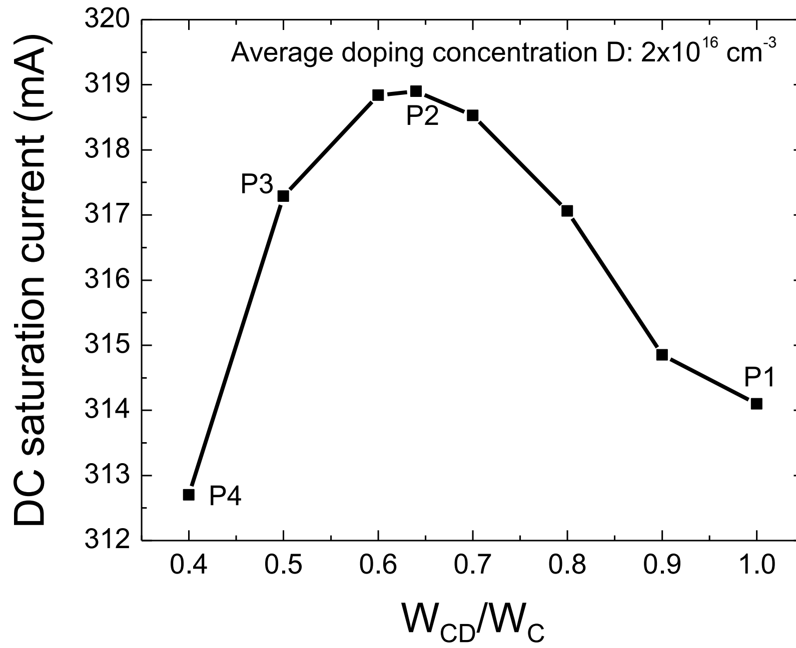

Figure 4.13 Simulated DC saturation current versus W_{CD}/W_C at D=2x10^{16} cm^{-3}.

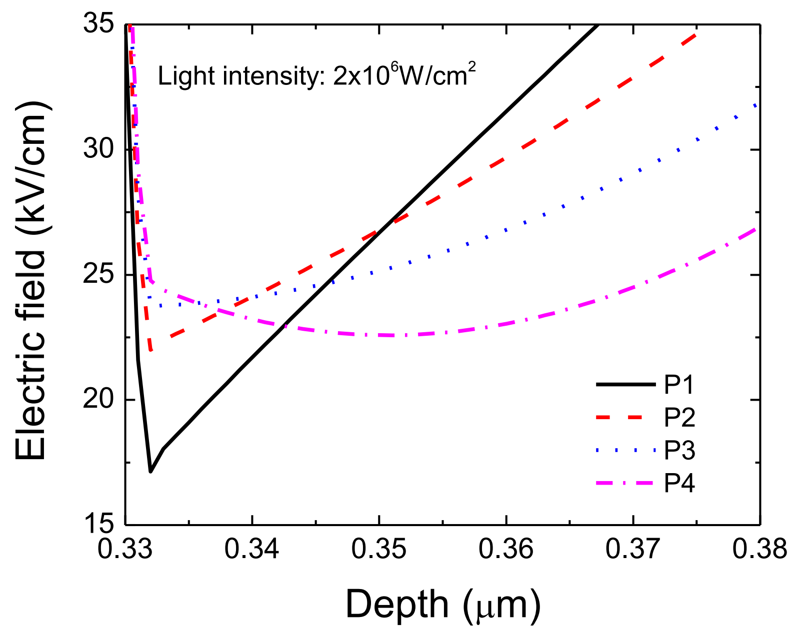

Figure 4.14 Distribution of electric field at the input end of collector under 2x10^6 W/cm^2 light intensity for the four cases marked in Fig. 4.13.

4.4 Design of collection layer based on Gaussian doping profile

According to the previous analysis, the DC saturation current is not enhanced significantly by the optimization of linearly doped collection layer. On the other hand, as can be seen from Fig. 4.14, althought the maximum saturation current occurs at case P2, its electric field in the collection layer near the absorption layer end (from 0.327 to ~0.34 μm) is lower than that of case P3. Thus, at high optical injection level, the minimum electric field in the collection layer may not be the only factor that limits the saturation performance. It is found that, the electric field gradient also has influence on the saturation performance. When the minimum values of the electric field are similar, if the electric field gradient at the input side of collection layer is larger, the saturation performance will be better.

As mentioned above, near the input side of the collection layer, higher doping concentration leads to higher electric field. While, for the output side of the collection layer, the electric field decreases as the doping concentration increases. Thereby, in order to enhance the electric field gradient near the collector input end and ensure a high electric field near the output end, we need to first increase the doping concentration from the collector input end and then decrease it from the peak value. This can be achieved by

using Gaussian doping profile. In the following, the design of collection layer based on Gaussian doping profile is investigated.

In ATLAS, the Gaussian doping profile is given by [30]

$$N(Y) = \text{N.PEAK} \cdot \exp\left[-\left(\frac{\text{Y - PEAK}}{\text{Y.CHAR}} \right)^2 \right], \tag{4.1}$$

where N.PEAK is the peak concentration of the Gaussian distribution, PEAK is the depth location of the peak doping in the Gaussian profile, and Y.CHAR is the principal characteristic length of the implant, which describes the spatial spread of the distribution. Different Gaussian doping profiles can be obtained by changing these parameters. Accordingly, different electric field distributions in the collection layer can be achieved. We can optimize the saturation performance by adjusting N.PEAK, PEAK and Y.CHAR. In addition, there is another condition that should be satisfied. In order to reasonably compare with the considered UTC-PD, we should maintain the same average doping concentration in the collection layer as mentioned above. Namely, the average doping concentration in the collection layer should be 2×10^{16} cm^{-3}. Here, we define the average doping concentration D in the collection layer by $D = \frac{Q}{W_C}$, where Q is the implant dose contained within the collection layer, and W_C is the thickness of the collection layer, which is 263 nm for the studied UTC-PD. It can be calculated that, the implant dose Q in

the collection layer is $5.26\text{x}10^{11}$ cm^{-2}. For Gaussian profile, the total dose can be calculated by integrating N(Y) over the collection layer region, which can be expressed as follows,

$$
\begin{aligned}
Q &= \int_{y_1}^{y_2} N(Y)dY \\
&= \frac{\sqrt{\pi}}{2} \cdot \text{N.PEAK} \cdot \text{Y.CHAR}\left[erf\left(\frac{\text{y}_2 - PEAK}{\text{Y.CHAR}}\right) - erf\left(\frac{y_1 - PEAK}{\text{Y.CHAR}}\right)\right]
\end{aligned}
\quad (4.2)
$$

where y_1 and y_2 are the depth location of the input side and output side of the collection layer respectively. For the studied UTC-PD, y_1=0.327 μm and y_2=0.59 μm. According to Eq. (4.2), for a given set of values of PEAK and Y.CHAR, a certain value of N.PEAK can be obtained to satisfy the condition. Therefore, we only need to vary the values of PEAK and Y.CHAR to find the suitable Gaussian doping profile, and thus achieve the optimal saturation performance. The effects of these two parameters will be investigated.

Firstly, the impact of different locations of the peak doping concentration on the saturation performance is studied. We assume the value of the principal characteristic length Y.CHAR is 0.05 μm, and the location of the peak doping concentration PEAK moves from the collector input end to the middle of the collection layer. When the peak doping concentration of the Gaussian profile is at the input end of the collection layer, it is similar to the case of linear doping profile. As shown in Table 4.1, the corresponding peak concentration of the Gaussian distribution can be calculated by using Eq. (4.2).

Table 4.1 N.PEAK at various values of PEAK, when Y.CHAR=0.05 μm.

	Y.CHAR=0.05 μm					
PEAK (μm)	0.327	0.35	0.38	0.39	0.4	0.4585
N.PEAK (cm^{-3})	1.19×10^{17}	8.00×10^{16}	6.36×10^{16}	6.17×10^{16}	6.05×10^{16}	5.94×10^{16}

Thus, different Gaussian doping profiles in the collection layer can be determined. The relation between the DC saturation current and the depth location of the peak doping is plotted in Fig. 4.15. As mentioned above, when the doping concentration is higher than 1×10^{17} cm^{-3}, the electron mobility and velocity overshoot may be affected. Thus, the case that the location of the peak doping is at the collector input end (PEAK=0.327 μm) is not considered. It can be seen that the DC saturation current first increases and then decreases as the location of the peak doping moves from the input end to the middle of the collection layer. The maximum DC saturation current occurs at P2, where the depth location of the peak doping is ~0.39 μm. In addition, the Gaussian doping profiles in the collection layer of three cases, P1 (PEAK=0.35 μm), P2 (PEAK=0.39 μm) and P3 (PEAK=0.4585 μm, the middle of collection layer), are shown in Fig. 4.16. The comparison of the distributions of electric field at the input end of collection layer at high light intensity (2×10^6 W/cm^2) between these three cases is plotted in Fig. 4.17. According to Fig. 4.16, we can see that, as the location of the peak doping moves from the input end to the middle of the collection layer, there are less dopants near the collector input end

(from 0.327 to ~0.38 μm) for space-charge compensation. Consequently, as shown in Fig. 4.17, the electric field near this end (from 0.325 to ~0.332 μm) drops. On the other hand, the difference of the doping concentration from the input end to the peak location becomes larger, which leads to the electric field gradient becomes larger. According to the previous analysis, lowering electric field near the input side of the collection layer results in poorer saturation performance. However, if the electric field gradient increases, the electron can be efficiently accelerated, which leads to better saturation performance. Thus, there is a trade-off between the minimum electric field and the electric field gradient. The change of saturation current, as plotted in Fig. 4.15, can be explained as follows. When the location of the peak doping moves from case P1 to case P2, the saturation performance is enhanced since the electric field gradient plays a dominant role. After P2, the saturation current drops since it is mainly limited by the minimum electric field. For the optimal case P2, in which the depth location of the peak doping of Gaussian distribution is ~0.39 μm, the corresponding DC saturation current is 333.47 mA.

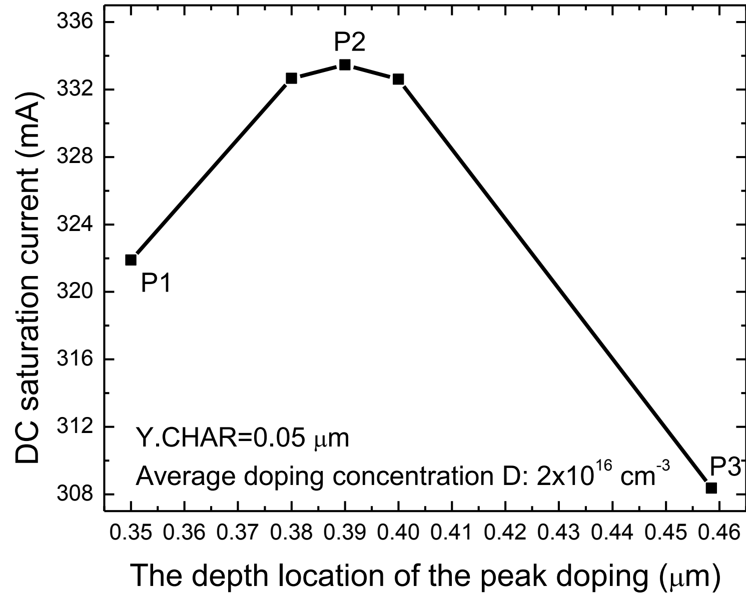

Figure 4.15 Simulated DC saturation current versus the depth location of the peak doping at Y.CHAR=0.05 μm and D=2x10^{16} cm^{-3}.

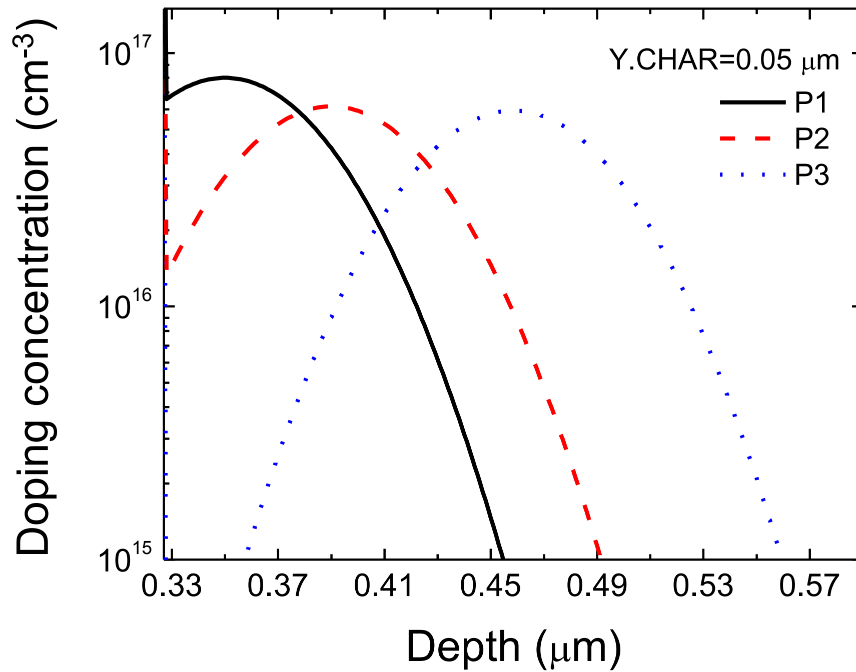

Figure 4.16 Gaussian doping profile in the collection layer for the cases marked in Fig. 4.15.

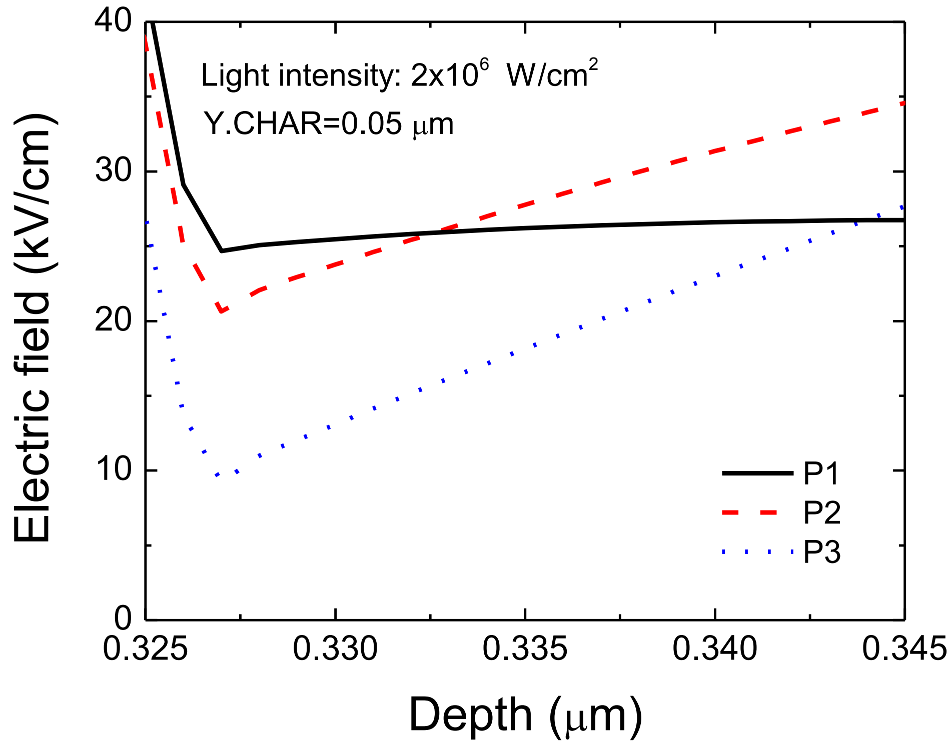

Figure 4.17 Distribution of electric field at the input end of collector under $2\text{x}10^6$ W/cm^2 light intensity for the three cases marked in Fig. 4.15.

Then, we set the peak doping position to 0.39 μm and investigate the effect of characteristic length on the saturation performance. The characteristic length Y.CHAR determines the spatial broadening of distribution. When the characteristic length becomes larger, Gaussian distribution will be more flat. If the characteristic length is large enough, it will be similar to the case of uniform doping profile. As shown in Table 4.2, the peak concentrations of the Gaussian distribution at several values of characteristic length can be calculated by using Eq. (4.2).

Table 4.2 N.PEAK at various values of Y.CHAR, when PEAK=0.39 μm.

	PEAK=0.39 μm				
Y.CHAR (μm)	0.029	0.03	0.04	0.05	0.06
N.PEAK (cm^{-3})	$1.02 x 10^{17}$	$9.91 x 10^{16}$	$7.52 x 10^{16}$	$6.17 x 10^{16}$	$5.31 x 10^{16}$

Thus, different Gaussian doping profiles in the collection layer can be obtained. Fig. 4.18 shows the DC saturation current with varying the value of characteristic length Y.CHAR. We can see that the DC saturation current increases as the characteristic length Y.CHAR decreases. However, since the electron mobility and velocity overshoot may be affected by the doping concentration higher than $1 x 10^{17}$ cm^{-3}, the case that the characteristic length is less than 0.03 μm is not considered. Thus, the maximum DC saturation current occurs at P3, where the characteristic length is ~0.03 μm. Moreover, Fig. 4.19 shows the Gaussian doping profiles in the collection layer of the three cases, P1 (Y.CHAR=0.06 μm), P2 (Y.CHAR=0.05 μm) and P3 (Y.CHAR=0.03 μm). The comparison of the distributions of electric field at the input end of the collection layer at high light intensity ($2 x 10^6$ W/cm^2) between these three cases are plotted in Fig. 4.20. According to Fig. 4.19, we can see that, as the characteristic length decreases, Gaussian distribution becomes steeper, and thus the difference of the doping concentration from the collector input end to the peak location becomes larger. Consequently, as shown in Fig. 4.20, the electric field increases more rapidly. In addition, it can be seen that the minimum value of the

electric field in each case is very close, namely the limitation of low electric field for each case is almost the same. Therefore, according to the previous analysis, the electric field which rises faster leads to a better saturation performance. This is verified by the simulation results shown in Fig. 4.18. For the considered UTC-PD, the optimal Gaussian doping profile can be obtained by specifying the peak concentration N.PEAK to 9.91×10^{16} cm^{-3}, the peak doping location PEAK to 0.39 μm, and the characteristic length Y.CHAR to 0.03 μm. The DC saturation current is significantly improved to 337.94 mA. Compared to the corresponding UTC-PD with optimized linearly doped collection layer, the improvement is 6.0%.

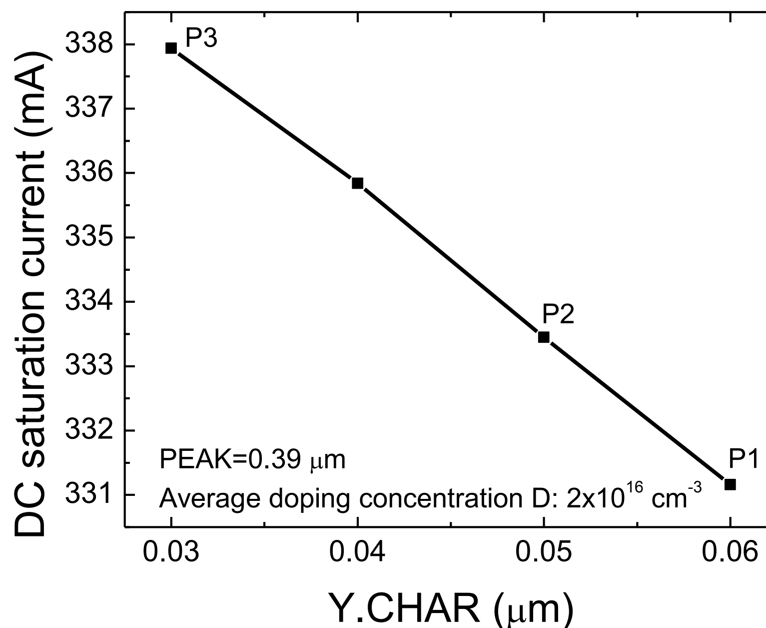

Figure 4.18 Simulated DC saturation current versus Y.CHAR at PEAK=0.39 μm and $D=2 \times 10^{16}$ cm^{-3}.

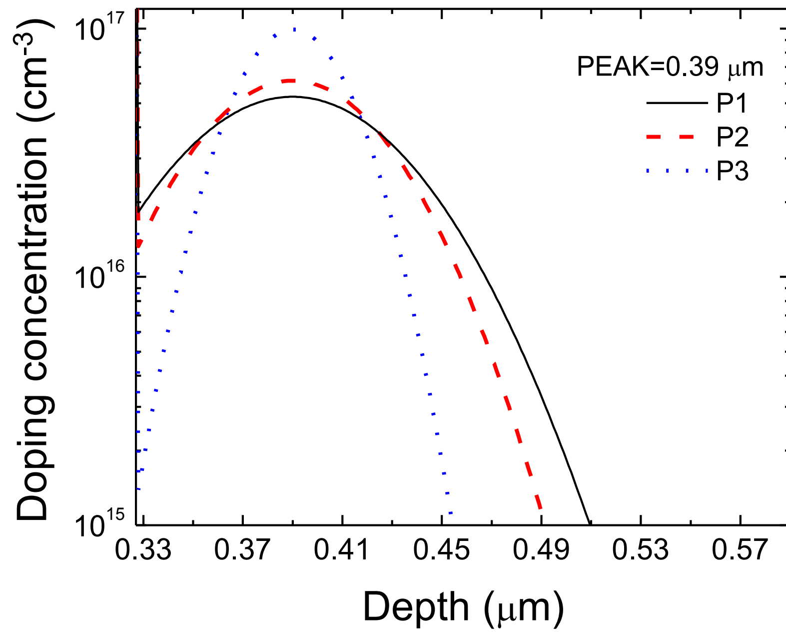

Figure 4.19 Gaussian doping profile in the collection layer for the cases marked in Fig. 4.18.

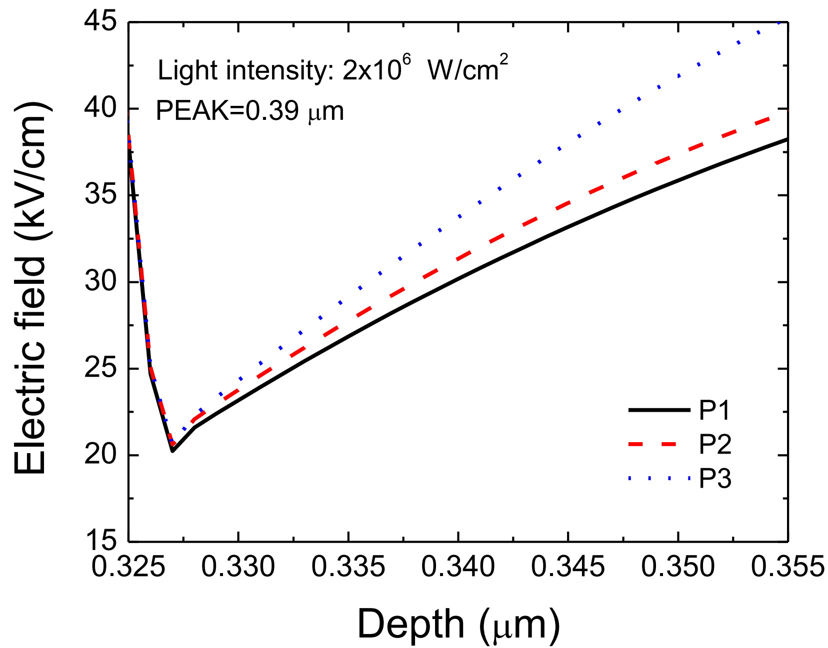

Figure 4.20 Distribution of electric field at the input end of collector under $2x10^6$ W/cm^2 light intensity for the three cases marked in Fig. 4.18.

4.5 Discussion and summary

In this chapter, the doping effect in the collection layer is investigated. First of all, it is verified that, as described in [54], the space-charge effect can be characterized by the electric field reduction at the collector input under high current injection. And the space-charge effect can be relieved by using the technique of charge compensation. It is verified that the saturation current can be enhanced by employing a uniformly doped collector layer. Then, in order to further improve the saturation perforance, a collection layer with linear doping profile and a collection layer with Gaussian doping profile are proposed. Moreover, all the methods are optimized. In the following, Fig. 4.21 shows the different doping profiles in the collection layer, the corresponding distributions of electric field near the input end of the collection layer are illustrated in Fig. 4.22, and the DC photocurrent response to the optical source is plotted in Fig. 4.23. Firstly, according to the optimization of uniform doping profile, it is found that, higher collector doping level leads to better saturation performance. This is because the electric field in the space layer, cliff layer and the collector input side is enhanced. However, 3-dB bandwidth drops at high doping concentration, since the collection layer cannot be completely depleted at normal device operation bias voltage. For PD_{80}, the appropriate uniform doping

concentration is found to be $2x10^{16}$ cm^{-3}. Compared to the original structure in [6], the DC saturation current increases from 268.67 mA to 296.92 mA, an improvement of 10.5%. Then, the average doping concentration in the collection layer is maintained the same, while the uniform doping profile is replaced by linear doping profile and Gaussian doping profile. We can see that, the electric field is further enhanced, which further reduces the space-charge effect, and thus leads to better saturation performance. By employing the optimized linear doping profile, the saturation current can be increased to 318.90 mA. Compared to the original structure [6], the improvement is 18.7%. While, a saturation current of 337.94 mA is achieved by using optimized Gaussian doping profile. Compared to the original structure [6], the improvement is 25.8%. As can be seen from Fig. 4.22, comparing the Gaussian doping method with the linear doping method, although the electric field in the space layer (from 0.31 to 0.32 μm), cliff layer (from 0.32 to 0.327 μm) and the collector input end (from 0.327 to ~0.329 μm) is a little bit lower, the rapidly rising electric field in the collection layer leads to the better saturation performance.

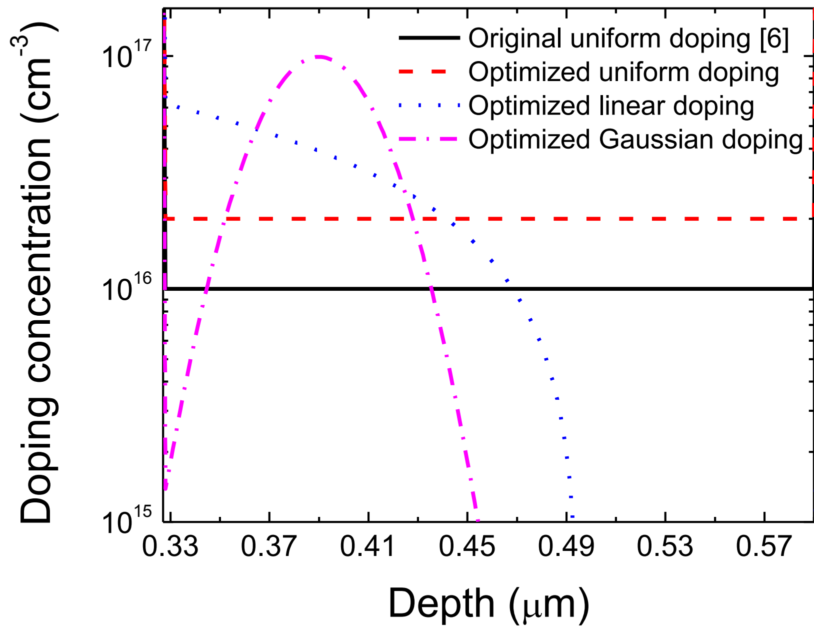

Figure 4.21 Different doping profile in the collection layer. Noted: the y-axis scale is log10.

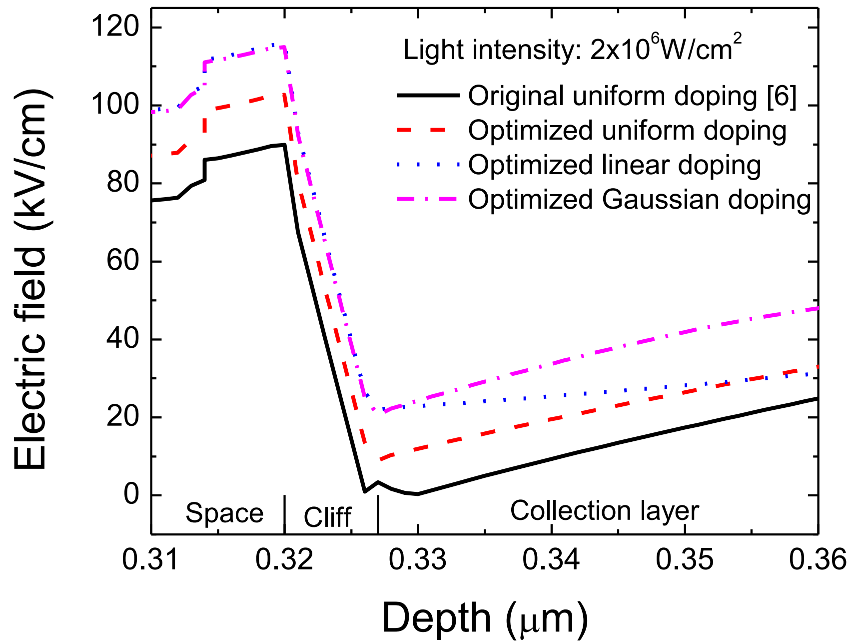

Figure 4.22 Distribution of electric field near the input end of collector under $2x10^6$ W/cm^2 light intensity for PD_{80} with different collector doping profile.

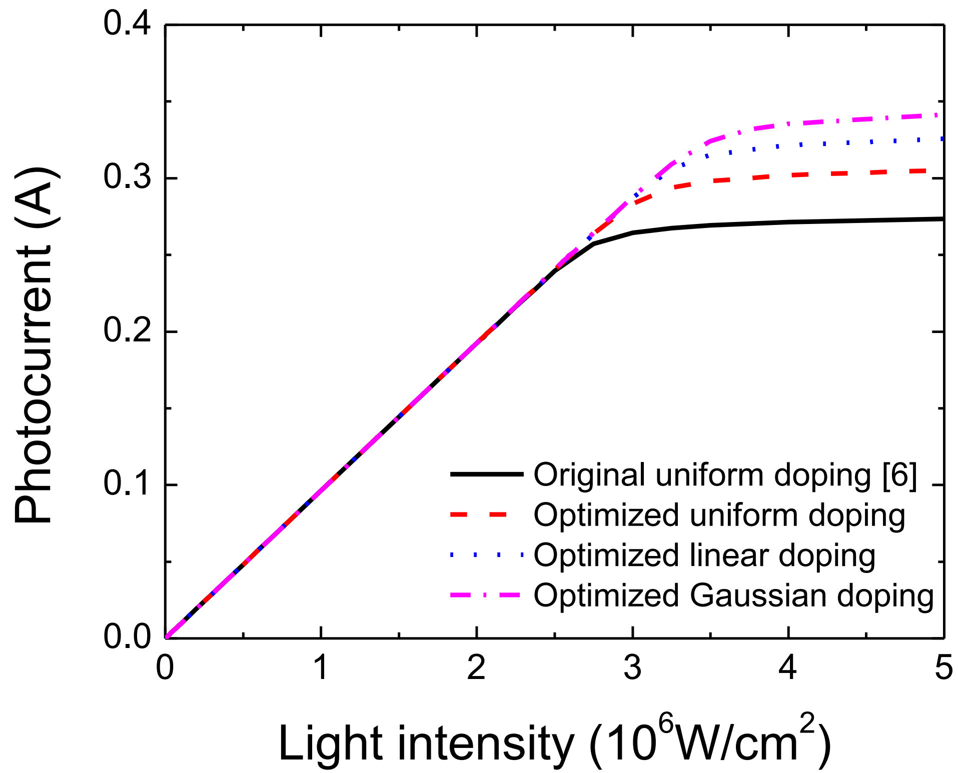

Figure 4.23 Simulated DC photocurrent versus light intensity for PD_{80} with different collector doping profile.

Chapter 5 Design and Fabrication of High-Speed and High-Power UTC-PDs

As described in chapter 3, we proposed a novel graded bandgap absorption layer structure to improve the speed performance. In this chapter, the epitaxial layer structures of two designed broadband and high-output power UTC-PDs are described. Different from the first UTC-PD (PD_A), the other UTC-PD (PD_B) employs a graded bandgap absorption layer to enhance the bandwidth performance. Moreover, a cliff layer, which can be used to improve saturation performance, is added in PD_B. Additionally, the design of fabrication process is introduced.

5.1 Device structure

The epitaxial layer structure of PD_A is designed according to the Near-ballistic UTC-PD (NBUTC-PD) reported by J.-W. Shi et al. [19]. Their NBUTC-PD shows superior performance. A 250 GHz bandwidth and a 17 mA saturation current under a 50 ohm load has been demonstrated [19]. Both the structures of PD_A and PD_B were grown on semi-insulating (S.I.) InP substrates by the chemical beam epitaxy (CBE) reactor. Table. 5.1 shows the epitaxial layer structure of our designed PD_A in detail. Compared with their NBUTC-PD, the major difference is that we employ $In_{1-x}Ga_xAs_yP_{1-y}$ system

instead of $In_{1-x-y}Al_xGa_yAs$ system. Starting from the substrate, the epitaxial layer growth begins sequentially with a 200 nm n^+ InP layer and a 20 nm n^+ $In_{0.53}Ga_{0.47}As$ etching stop layer. The 800 nm n^+ InP contact layer is highly doped to $4x10^{18}$ cm^{-3} to reduce the contact resistance. Followed is three thin charge layers, which consist of a 5 nm n^+ InP charge layer, a 5 nm p^- InP charge layer and a 10 nm p^+ InP charge layer. Charge layers are inserted to control the distribution of the electric field in the collector layer. Then, the 120 nm n^- InP collection layer is followed by a 20 nm lightly n-type doped $In_{0.53}Ga_{0.47}As$→InP transition layer. As mentioned in chapter 4, the collection layer is n-type doped to $2x10^{16}$ cm^{-3} for charge compensation. The transition layer is employed to form a smooth connection between the absorption layer and the collection layer. Here, the transition layer is achieved by changing the the composition fractions x and y of $In_{1-x}Ga_xAs_yP_{1-y}$. The composition fraction x varies linearly from 0.47 to 0, and y varies from 1 to 0 correspondingly. The 150 nm p-type $In_{0.53}Ga_{0.47}As$ absorption layer employs a linearly graded doping profile to introduce a built-in electric field which can assist electron to transport. The highest doping concentration in the absorption layer is located at the blocking layer side and the lowest concentration is located at the transition layer side. Above the absorption layer, the function of the 80 nm wide bandgap p^+ InP blocking layer is to prevent the diffusion of the electrons to the anode and promote the electrons

generated in the absorption layer to transport towards the InP collection layer. On top is a 100 nm p^+ $In_{0.53}Ga_{0.47}As$ contact layer, which is highly doped to form a good ohmic contact. The epitaxial layer structure of PD_B is shown in Table. 5.2. Compared to PD_A, a graded bandgap absorption layer is employed in PD_B to construct a built-in electric field and thus improve the speed performance. The $In_{0.53}Ga_{0.47}As$ absorption layer of PD_A is replaced by a linear compositionally-graded $In_{0.59}Ga_{0.41}As_{0.88}P_{0.16}\rightarrow In_{0.53}Ga_{0.47}As$ absorption layer. As a result, for PD_B, the energy gap of the absorption layer varies linearly from 0.786 eV to 0.737 eV. This linearly graded energy gap is suitable for the device operation at a optical wavelength of 1.55 μm, and can introduce a built-in electric field to accelerate the electrons. It is noted that, similar to the NBUTC-PD structure in [19], for both PD_A and PD_B, the charge layer is inserted between the collection layer and the n-contact layer. The charge layer is used to enhance the electric field near the output side of the collection layer. In addition, for PD_B, not only the charge layer, but also a 20 nm n^+ InP cliff layer is added between the transition layer and the collection layer. The function of the cliff layer is similar to that of the charge layer. It is used to sustain the high electric field near the input side of the collection layer. And thus the saturation performance can be further enhanced.

Table 5.1 Epitaxial layers of PD_A.

Layer	Thickness (nm)	Doping (cm^{-3})/Type	Band gap E_g (eV)
$In_{0.53}Ga_{0.47}As$ p-contact	100	$>1\times10^{19}$/P	0.737
InP blocking	80	1.5×10^{18}/P	1.35
$In_{0.53}Ga_{0.47}As$ absorption	150	1.5×10^{19} (T) - 2.5×10^{17} (B)/P	0.737
$In_{0.53}Ga_{0.47}As$ (T) - InP (B) transition	20	2×10^{16}/N	--
InP collection	120	2×10^{16}/N	1.35
InP charge 1	10	1.5×10^{18}/P	1.35
InP charge 2	5	2×10^{16}/P	1.35
InP charge 3	5	1×10^{18}/N	1.35
InP n-contact	800	4×10^{18}/N	1.35
$In_{0.53}Ga_{0.47}As$ etch stop	20	4×10^{18}/N	0.737
InP subcolleciton	200	4×10^{18}/N	1.35

(S. I. InP Sub)

Table 5.2 Epitaxial layers of PD_B.

Layer	Thickness (nm)	Doping (cm^{-3})/Type	Band gap E_g (eV)
$In_{0.53}Ga_{0.47}As$ p-contact	100	$>1\times10^{19}$/P	0.737
InP blocking	80	1.5×10^{18}/P	1.35
$In_{0.59}Ga_{0.41}As_{0.88}P_{0.16}$ (T) - $In_{0.53}Ga_{0.47}As$ (B) absorption	150	1.5×10^{19} (T) - 2.5×10^{17} (B)/P	0.786-0.737
$In_{0.53}Ga_{0.47}As$ (T) - InP (B) transition	20	2×10^{16}/N	--
InP cliff	20	2×10^{17}/N	1.35
InP collection	120	2×10^{16}/N	1.35
InP charge 1	10	1.5×10^{18}/P	1.35
InP charge 2	5	2×10^{16}/P	1.35
InP charge 3	5	1×10^{18}/N	1.35
InP n-contact	800	4×10^{18}/N	1.35
$In_{0.53}Ga_{0.47}As$ etch stop	20	4×10^{18}/N	0.737
InP subcolleciton	200	4×10^{18}/N	1.35

(S. I. InP Sub)

5.2 Device characterization

For PD_A and PD_B, the simulations of modulation response, the distribution of the electric field in the absorption layer and DC photocurrent are performed. According to Fig. 5.1, we can see that the 3-dB bandwidth of PD_A is 247.2 GHz, which is in good agreement with the reported bandwidth (250 GHz) in [19]. For PD_B, as expected, a higher 3-dB bandwidth of 295.3 GHz is achieved. Moreover, as can be seen from Fig. 5.2, in the 0.15-μm-thickness absorption layer (from 0.18 to 0.33 μm), the built-in electric field of PD_B is higher than that of PD_A. Therefore, the benefits of proposed graded bandgap absorption layer is further verified. Additionally, as obtained from Fig. 5.3, the DC saturation currents of PD_A and PD_B are predicted to be 101.6 mA and 113.4 mA respectively. The saturation performance improvement is due to the effect of cliff layer.

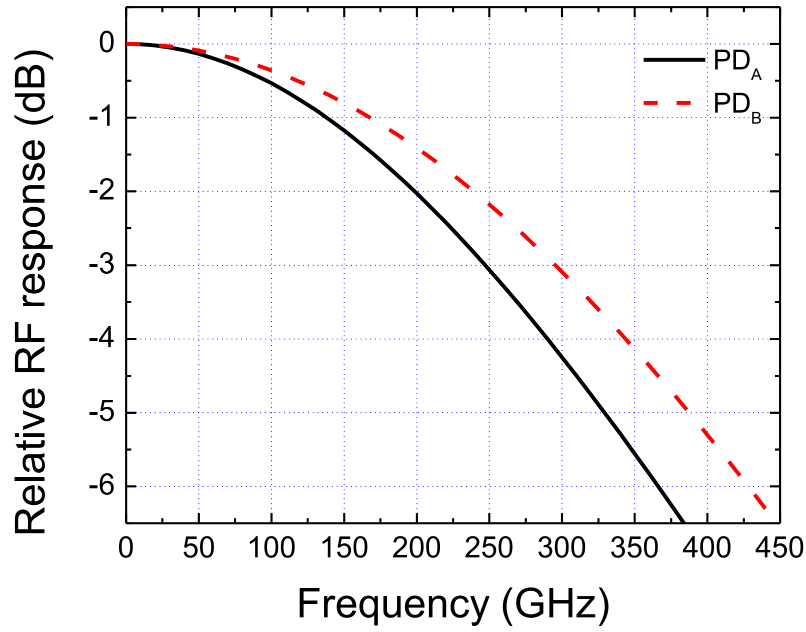

Figure 5.1 Simulated modulation response of PD_A and PD_B.

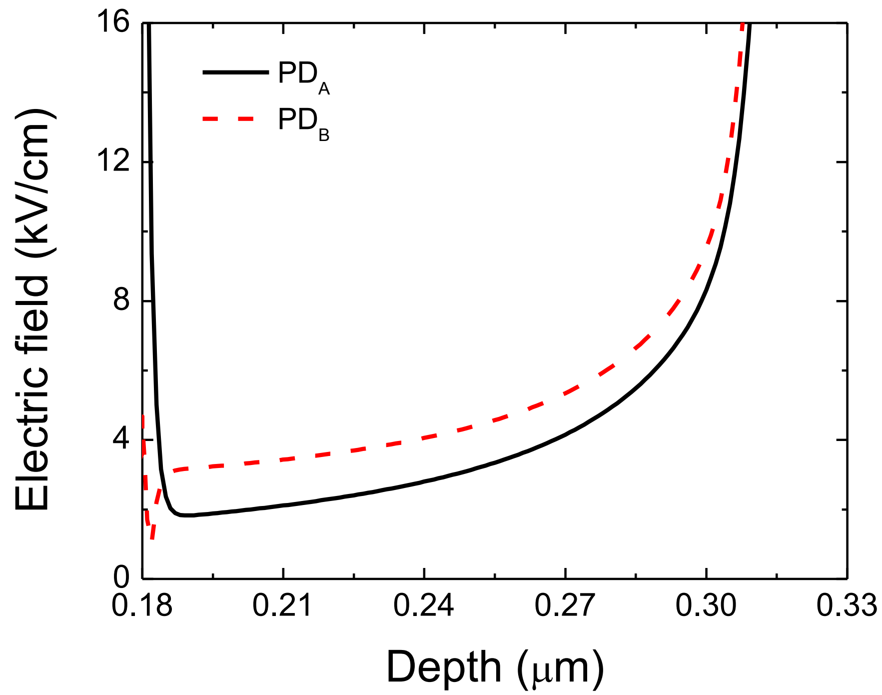

Figure 5.2 Distribution of electric field in the absorption layer of PD_A and PD_B.

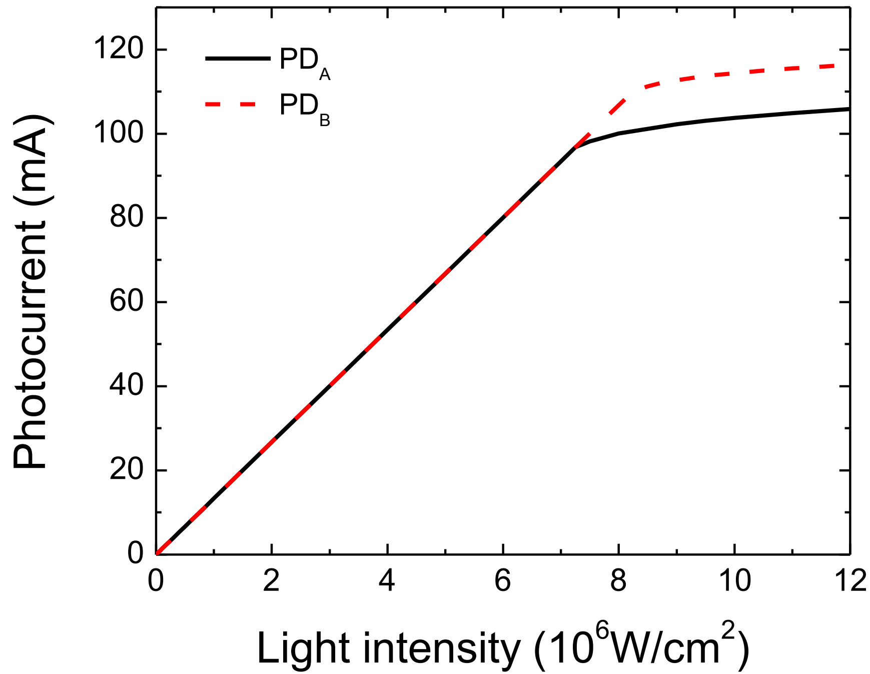

Figure 5.3 Simulated DC photocurrent versus light intensity of PD_A and PD_B.

5.3 Device fabrication

This section describes the design of fabrication process of the above mentioned UTC-PD PD_A and PD_B. In order to save time and to avoid device failure which may be caused by fabrication process, we need to minimize process steps and reduce process complexity as far as possible. Thus, we will fabricate the wafer into backside illuminated mesa structures by using conventional photolithography, dry and wet etching, passivation, and metal liftoff techniques. In the following, the important techniques and the major steps of fabrication flow will be described in sequence.

5.3.1 P-type contact metalization

In order to improve 3-dB bandwidth performance, the RC-time constant τ_{RC} need to be reduced. Thus, contact metalization is significant for broadband UTC-PD, because the contact resistance is the main part of the parasitic series resistance. The formation of good ohmic contact is required. The advantage of the ohmic contact is that the contact resistance is small. The contact resistance R_c is inversely proportional to the area of the contact [55], and it can be given by $R_c = r_c / A$. Here, r_c is the specific contact resistivity in ohm-cm^2 and A is the area of the contact. The specific contact resistivity is found to be [56] $r_c \propto \exp\left[\frac{2\sqrt{\varepsilon_s m^*}}{\hbar}\cdot\frac{\phi_B}{\sqrt{N}}\right]$, where ϵ_s is the permittivity of the semiconductor, m^* is the effective mass of carrier, ħ is the Planck's constant, N is the impurity doping concentration, and ϕ_B is the barrier height of the semiconductor contact. Moreover, for p-type contact, the barrier height can be expressed as $\phi_B = E_g - (\phi_M - \chi_S)$, where E_g is known as the bandgap energy of semiconductor, ϕ_M is the metal work function and χ_S is the electron affinity of semiconductor. The small specific contact resistivity r_c is desired. Therefore, we need to highly dope the contact layer of our device and construct a low barrier height of the semiconductor contact. As described above, the doping level in the InGaAs p-contact layer is more than $1\text{x}10^{19}$ cm^{-3}. The bandgap energy and the electron

affinity of InGaAs is 0.737 eV and 4.58 eV respectively. We use Au (gold, ϕ_M=5.1 eV) as the contact metal, since Au leads to a low barrier height and it has good electrical conductivity. However, Au may diffuse into semiconductor. The diffusion leads to the formation of spikes of Au, which may penetrate the contact region. To solve the spiking problem, we use Pt (platinum, ϕ_M=5.65 eV) as a barrier to prevent spiking. In addition, Ti (titanium, ϕ_M=4.33 eV) is added to provide good adhesion to the InGaAs p-contact layer.

The p-type contact metalization process starts from the wafer cleaning. Then, the lift-off resist (LOR), which is used for the liftoff process, can be deposited immediately. Followed by depositing a layer of photoresist. Thereby, the p-type contact metal window can be opened by using the corresponding mask after the photoresist exposure and development. Subsequently, in order to improve the ohmic contact, we need to remove the oxide over the surface. Then, as mentioned above, the metal sequence Ti/Pt/Au (30/50/300 nm) can be deposited by electron-beam evaporation. Finally, the wafer need to be immersed in acetone to dissolve the LOR. Thus, all the materials deposited above the LOR will be removed simultaneously, only leaving the patterned p-type contact metal on the top of the wafer. The schematic diagram of the wafer after p-type contact metalization is illustrated in Fig. 5.4(a). And Fig. 5.4(b) shows the corresponding cross-sectional view.

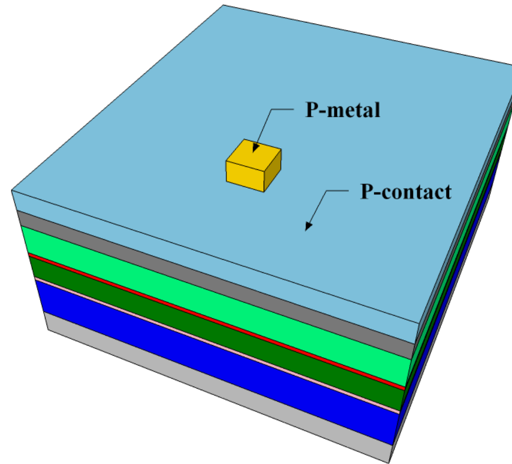

(a)

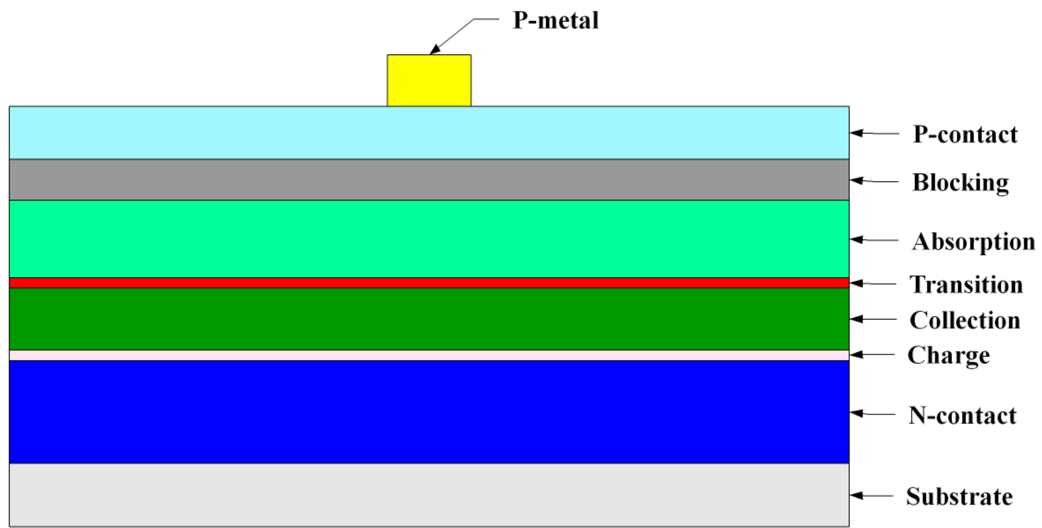

(b)

Figure 5.4 (a) Schematic diagram of the wafer after p-type contact metalization, (b) the cross-sectional view.

5.3.2 P-mesa formation

After p-contact metalization, p-mesa formation can be carried out. The p-type contact metal is used as the mask to define the pattern of the active region. In order to

avoid affecting the performance of the device and to minimize the dimension changes in vertical direction, reactive-ion etching (RIE) technology is used to expose the heavily doped n-type InP contact layer. The etching depth is about 0.5 μm. The drawback of dry etching process is that it may cause damage to the sidewalls of p-mesa, which results in the surface leakage current. Thus, after etching, we can dip the wafer in Br-methanol etchant for seconds to remove the damaged portion on the surface of the sidewalls. Then, as shown in Fig. 5.5(a), p-mesa, namely the active region is formed. Its cross-sectional view is also illustrated in Fig. 5.5(b).

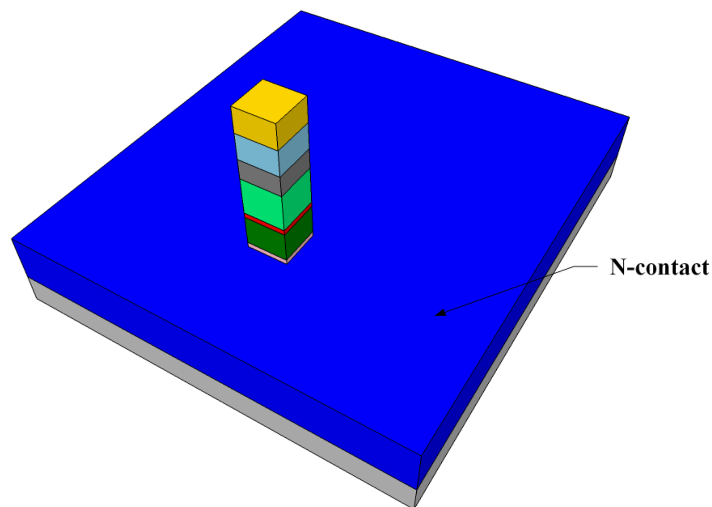

(a)

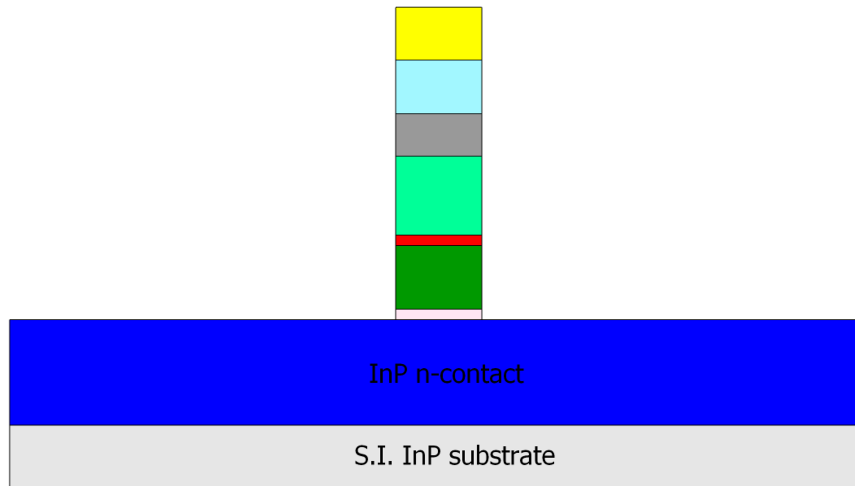

(b)

Figure 5.5 (a) Schematic diagram of the wafer after p-mesa formation, (b) the cross-sectional view.

5.3.3 N-type contact metalization

As described above, in order to form good ohmic contact, we need to highly dope the contact layer and build a low barrier height of the semiconductor contact. The InP n-contact layer of our devices is highly doped to $4x10^{18}$ cm^{-3}. For n-type contact, the barrier height is given by $\phi_B = \phi_M - \chi_S$. The electron affinity of InP is 4.38 eV [32]. N-type contact metal can be constituted by the following metal sequence, Ni/Ge/Au/Ni/Au (5/17/30/20/300 nm). Ni (nickel, ϕ_M=5.15 eV) is used for improving adhesion to the InP n-contact layer. The function of Ge (germanium, χ_S=4.13 eV) is to prevent Au penetrating the contact region. The fabrication steps of n-type contact

metalization are similar to p-type contact metalization. The pattern of n-type contact metal can be defined by the corresponding mask. After n-type contact metalization, the schematic diagram of the wafer and the cross-sectional view can be seen from Fig. 5.6.

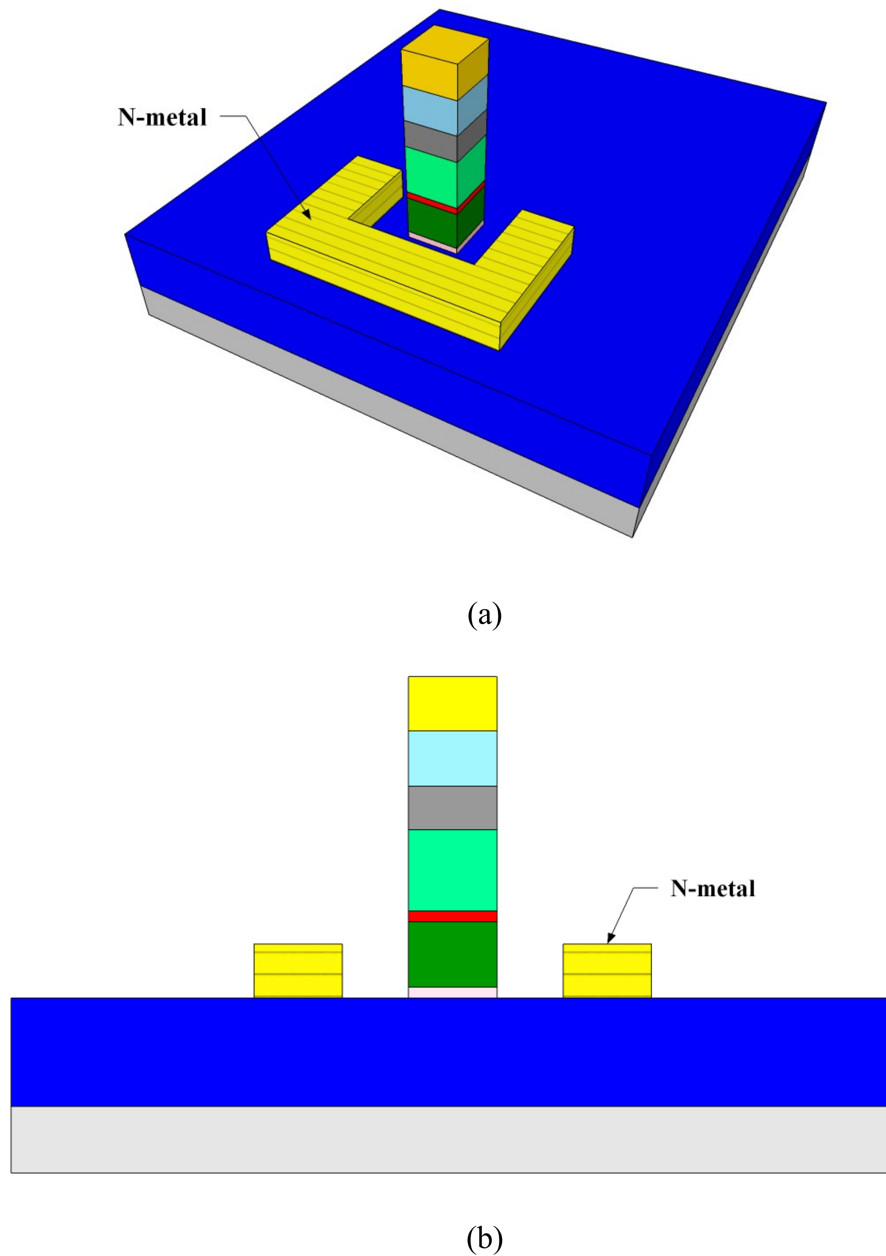

Figure 5.6 (a) Schematic diagram of the wafer after n-type contact metalization, (b) the cross-sectional view.

5.3.4 N-mesa formation

In order to make isolation between devices, and lower the parasitic effects such as the parasitic capacitance, n-mesa etching is required. Prior to etching, the surface of the wafer need to be coated with photoresist. Since there is about 0.5 μm height difference on the surface of the wafer after the p-mesa formation, we need a thick coating of photoresist. After photoresist exposure and development, the pattern of n-mesa region is transferred from the corresponding mask to the surface of the wafer. For n-mesa formation, wet etching is suitable to remove the excess n-contact layer and expose the semi-insulating substrate. After etching, the wafer need to be immersed in acetone to remove all the photoresist. Fig. 5.7(a) is the schematic diagram of the wafer after n-mesa formation. The cross-sectional view is shown in Fig. 5.7(b).

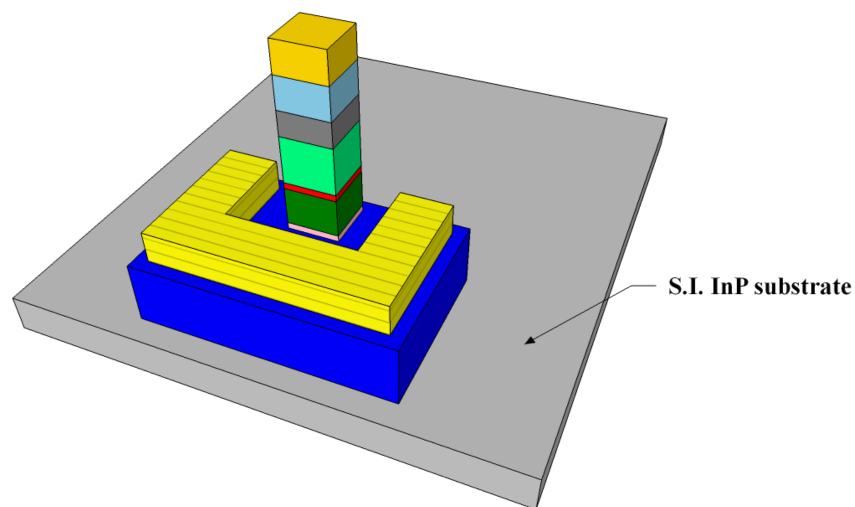

(a)

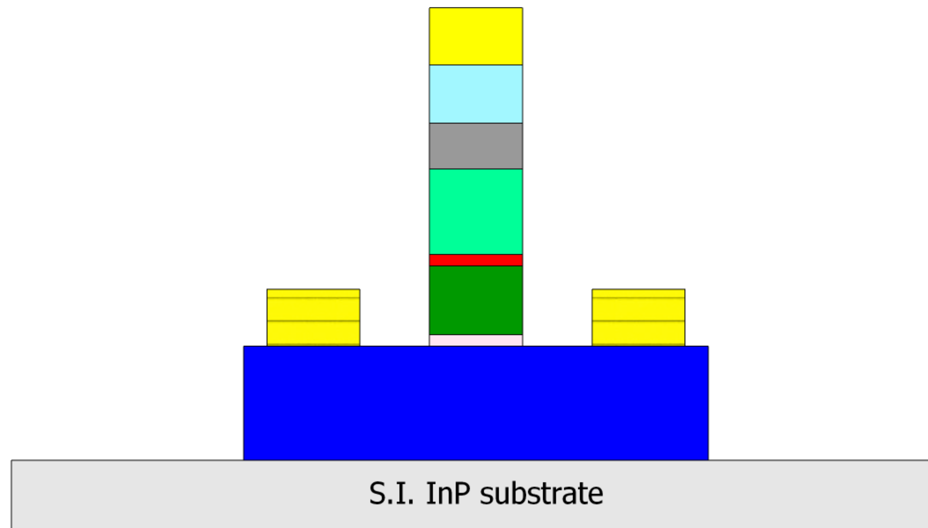

(b)

Figure 5.7 (a) Schematic diagram of the wafer after n-mesa formation, (b) the cross-sectional view.

5.3.5 Mesa passivation and via hole opening

In order to protect the sidewalls of the mesa and to reduce the surface leakage current, mesa passivation is an important step after etching. We can use Si_3N_4 as the passivation layer. One of the advantages of Si_3N_4 is that it is not easy to be permeated. Moreover, it can be uniformly deposited on the surface of the wafer. Furthermore, under the same dry etching condition, the etching rate of Si_3N_4 is much faster than that of photoresist. Thus, we don't need to coat a thick photoresist layer. Thereby, after the photoresist development, the pattern of the contact windows can be transferred more accurately from the mask to the surface of Si_3N_4. In addition, the Si_3N_4 passivation layer

will be removed partly by dry etching to form the contact windows. Consequently, the distortion of the via holes in the passivation layer is small. Therefore, after the subsequent planarization step, even if the distortion of the via holes in the poly methyl glutarimide (PMGI) planarization layer is more significant, the dark current will not become larger. The Si_3N_4 deposition can be done in the plasma-enhanced chemical vapor deposition (PECVD) system. Since there is height difference on the surface of the wafer, we need to deposit a thick layer of Si_3N_4 to avoid rupture of Si_3N_4.

After mesa passivation, both the P and n-type contact metals are covered by the Si_3N_4 passivation layer, it is necessary to open via holes in the passivation layer to connect these contact metals to the topmost CPW GSG contact pads. In order to prevent breakage between contact metals and CPW contact pads, the via holes should be large enough for metal deposition. After coating a layer of photoresist, the pattern of via holes can be transferred from the mask to the surface of passivation layer by photolithography. Then, we can use dry etching to expose the contact metals. Finally, the wafer is immersed in acetone to remove all the photoresist. The following Fig. 5.8 shows the schematic diagram and the corresponding cross-sectional view of the wafer after these steps.

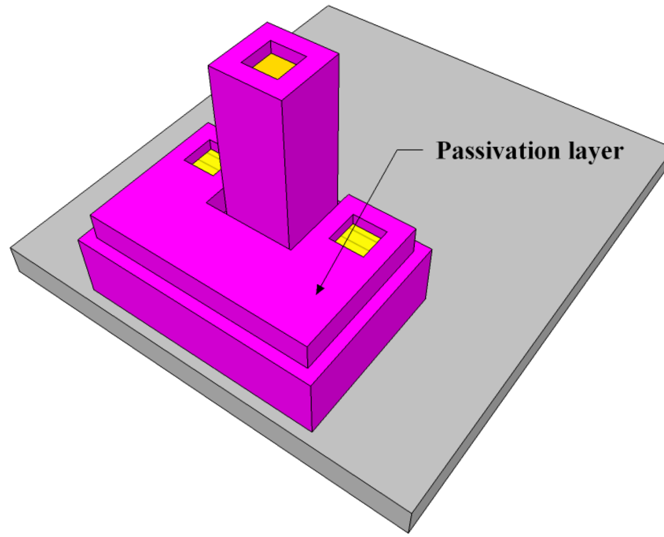

(a)

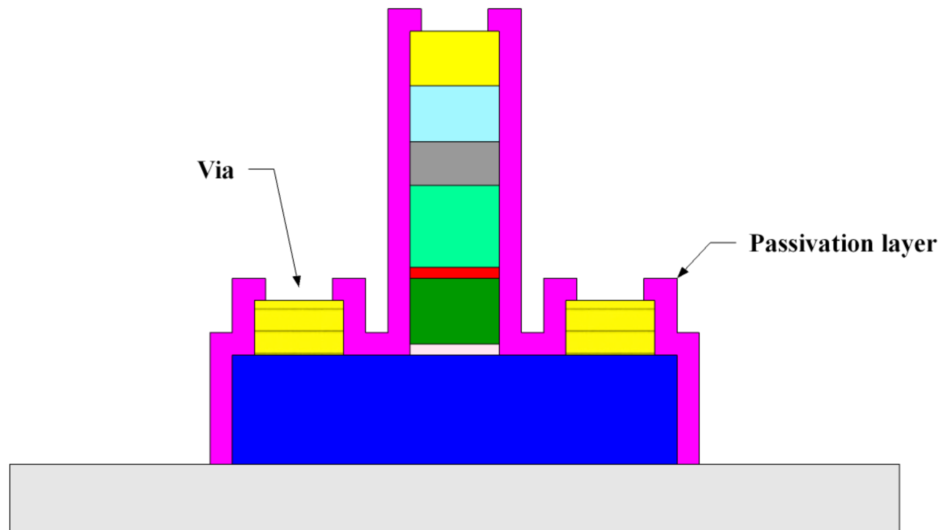

(b)

Figure 5.8 (a) Schematic diagram of the wafer after passivation, (b) the cross-sectional view.

5.3.6 Planarization and via hole opening

After the above steps, height difference still exists on the surface of the wafer. Taking into account the deposition of the topmost CPW-like GSG contact pads and the simplification of the fabrication process, we need to create a flat surface. In this way, we can directly deposit the GSG contact pads on the top of the wafer, and thus the following lithography step will be much easier. PMGI can be employed to achieve the highly planar layer, because it has several advantages as follows. First of all, the dielectric constant of PMGI is low, and thus the parasitic capacitance is small. Moreover, the performance of CPW contact pads can be improved by using a substrate with low dielectric constant. In addition, PMGI has a characteristic of reflow. Namely, when the temperature exceeds the critical temperature, the solid PMGI will liquefy. Because of this feature, PMGI is preferable to benzocyclobutene (BCB) to form the planarization layer. In order to cover the surface of the wafer, where exists a height difference of a few microns, we need to deposit a thick planarization layer. Then, similar to the passivation layer, via holes need to be opened in the planarization layer to make connections between the contact metals and the topmost CPW GSG contact pads. If BCB is used for planarization, after the opening of the via holes by dry etching, the sidewalls will be too steep, almost vertical.

This may result in breakage in the subsequently deposited metal in the via hole. Thus, there may be disconnection between the contact metals and the GSG contact pads. This problem can be solved by using PMGI to form the planarization layer. Due to the characteristic of reflow, if the temperature and time are controlled appropriately, a smooth tapered sidewall can be formed, which facilitates the deposition of metal. Accordingly, the breakage between contact metals and GSG contact pads can be avoided.

Similar to the mesa passivation step, when there is sufficient PMGI coated on the surface of the wafer to form a highly planar layer, the opening of via hole is required. Moreover, the process steps of the definition of the pattern of via holes are the same as those of mesa passivation. However, as mentioned above, we need to pay attention to the distortion problem. Since both the PMGI and photoresist belong to the polymer, under the same dry etching condition, the etching rate of PMGI is similar to that of photoresist. Thus, we need to use a thick photoresist layer as the barrier. The problem of the thick photoresist layer is that it may be overdeveloped, which results in the actual opening of the via hole is too large. Particularly, for the small devices, the size of the via hole opening is very important. On the one hand, in order to prevent breakage between contact metals and CPW contact pads, the opening should be large enough so that the metal deposition is facilitated. On the other hand, the opening should not be too large. It is

because that, if the photoresist is overdeveloped, the area of the metal cover becomes larger, which may lead to the connection between the electrode metals and thus causes a short circuit. Therefore, the dimensions of the mask, which defines the pattern of the contact windows, should be carefully designed. The via holes can be opened by dry etching, which will stop when the contact metals are exposed. The dry etching recipe, which does not react with the previously deposited Si_3N_4 passivation layer, can be employed. Finally, after removing all the photoresist, the wafer is baked to make PMGI reflow. As can be seen from Fig. 5.9(a), a plane is formed to deposit the contact pads. Fig. 5.9(b) illustrates the cross-sectional view.

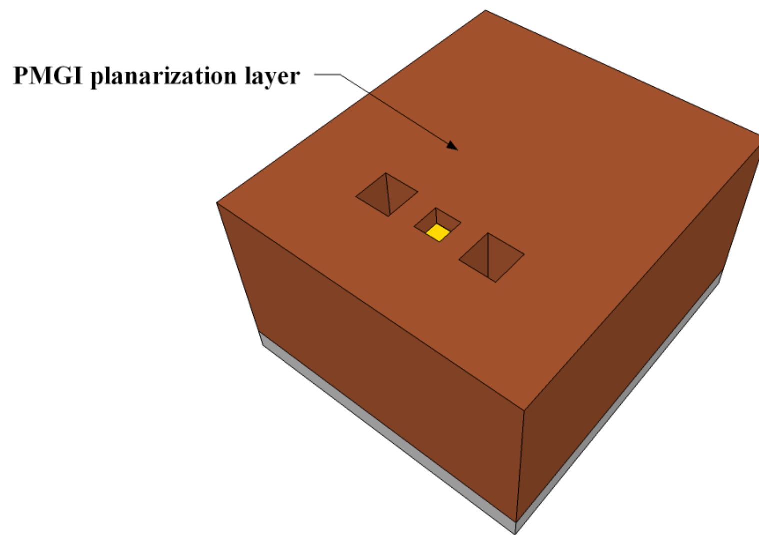

(a)

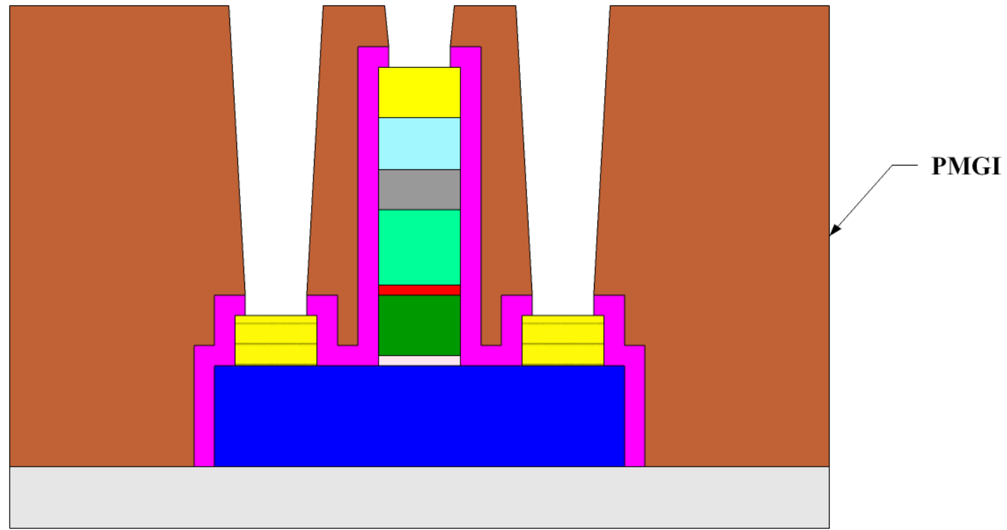

(b)

Figure 5.9 (a) Schematic diagram of the wafer after planarization, (b) the cross-sectional view.

5.3.7 Deposition of GSG contact pads

The steps of GSG contact pads fabrication process are similar to the steps of contact metalization. By using electron-beam evaporation, the metal sequence Ti/Au (30/400 nm) can be deposited directly on top of the PMGI planarization layer. The function of Ti is to provide good adhesion to the PMGI surface, and Au has good electrical conductivity to reduce the loss. By photolithography, the pattern of the topmost GSG contact pads can be defined by the corresponding mask. Finally, the GSG contact pads can be formed after the liftoff process. The schematic diagram of the finished device and the cross-sectional

view are illustrated in Fig. 5.10. Moreover, for the designed UTC-PD with 16 μm^2 active region, the suggested dimension parameters are stated in Fig. 5.11.

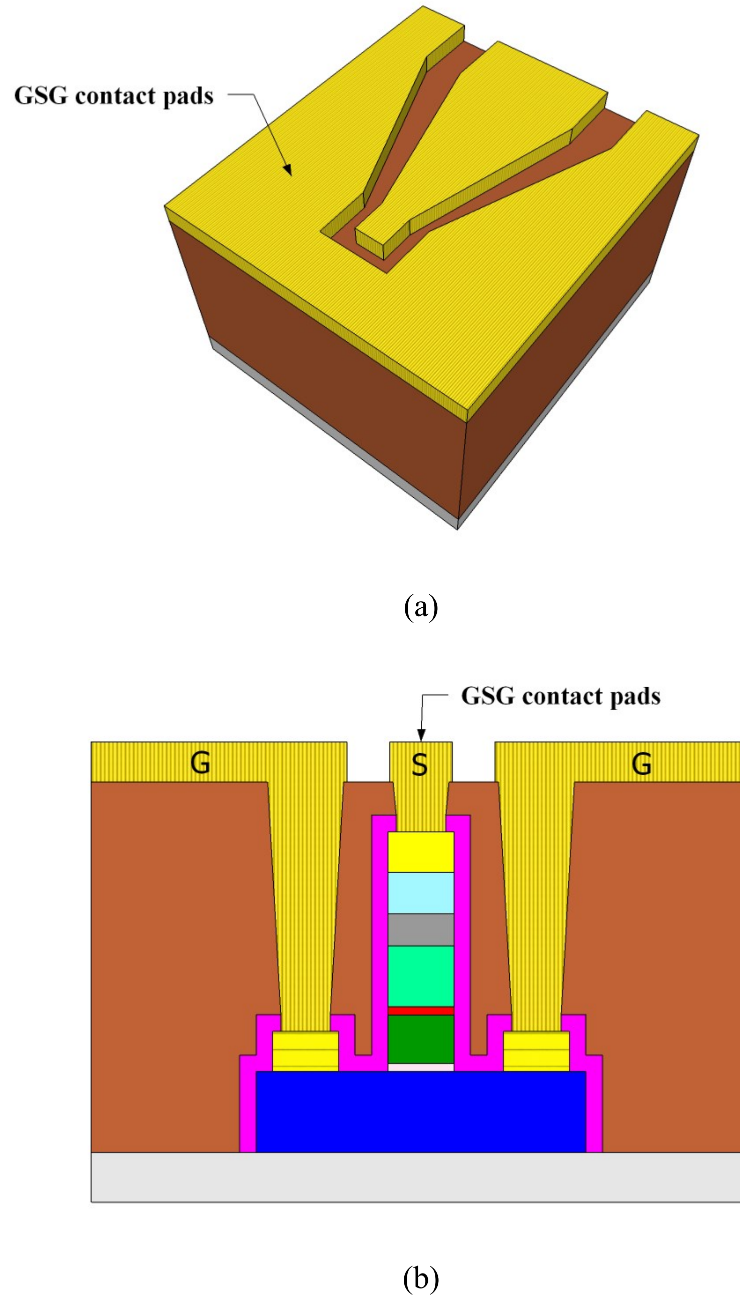

Figure 5.10 (a) Schematic diagram of finished device, (b) the cross-sectional view.

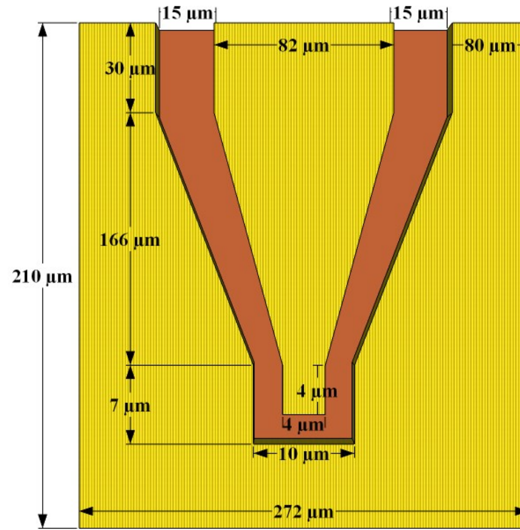

Figure 5.11 Suggested device dimensions.

5.4 Summary

In this chapter, two types of designed back-illuminated high-speed and high-power UTC-PD are presented. The simulation results predict that, for PD_A, a 3-dB bandwidth of 247.2 GHz and DC saturation current of 101.6 mA can be achieved. PD_B can achieve a 3-dB bandwidth of 295.3 GHz and DC saturation current of 113.4 mA. The functions of graded bandgap absorption layer and the cliff layer are verified. Moreover, the design of fabrication process is described in detail.

Chapter 6 Conclusions and Future Work

6.1 Conclusions

The main focus of this work is to improve the bandwidth and saturation performance of UTC-PD, since broadband and high-output-power PDs serve as the key component for future high-frequency and high-power fiber-optic systems. First of all, it is verified that the physics-based modeling of UTC-PDs can be used to predict the device performance, as long as appropriate models and parameters are specified. The energy balance transport model is employed, which includes the non-local effects such as velocity overshoot that has been observed experimentally in UTC-PDs. The simulation results show good agreement with the reported results. Consequently, the simulation results can be directly used for device design.

The bandwidth of PD is determined by the carrier transit time τ_{tr} and RC-time constant τ_{RC}. For UTC-PD, since the electron diffusion velocity in the absorption layer is much slower than the electron drift velocity in the depletion region, the carrier transit time τ_{tr} is mainly limited by the carrier traveling time τ_A in absorption layer. Therefore, in order to improve the bandwidth performance, a built-in electric field can be constructed in the absorption layer to accelerate the electrons. Using the physical modeling, it is

examined that, the 3-dB bandwidth can be enhanced by incorporating a linearly graded doping profile in the absorption layer. Then, the graded bandgap absorption layer has been further investigated. It is shown that a higher introduced built-in electric field in the front part of absorption layer leads to a better bandwidth performance. By using the optimized graded structure, the performance can be further improved. Moreover, the effects of the proposed combined graded absorption layer structure is studied. It is illustrated that, in the absorption layer, the combined introduced built-in electric field is nearly the sum of the built-in electric fields constructed by graded doping structure and graded bandgap structure. For PD_{80}, the simulation result shows an improvement of 39.4% in bandwidth.

The space-charge effect is the dominant saturation mechanism at the bias voltage considered in this work (-2V). Using the physical modeling, we analysed the space-charge effect. It is shown that, at high light intensity, electrons are accumulated in the absorption layer, and the electric field drops in the space layer, cliff layer, and also the input end of collection layer, which lead to saturation. We also examined that, the space-charge effect can be reduced by using the technique of charge compensation. The investigation of charge compensation by using uniform doping in the collector indicates that, higher collector doping level leads to better saturation performance. However, in

order to ensure the collection layer is completely depleted at normal device operation bias voltage, the collector doping level cannot be too high. Then, we investigated the effects of the proposed linearly doped collection layer, which can effectively compensate for the space charge. It is shown that, the distribution of electric field is improved. The electric field in the space layer, cliff layer and the collector input end is enhanced, which leads to the better saturation performance. In addition, by comparing the distribution of electric field of different linear doping cases, we found that, the saturation performance is not only limited by the minimum electric field in the collection layer at high optical injection level, but also is influenced by the electric field gradient. Accordingly, an optimized Gaussian doping profile in the collection layer is proposed. For PD_{80}, improvements of 18.7% and 25.8% in saturation current can be achieved by using optimized linear doping profile and Gaussian doping profile respectively.

Additionally, the epitaxial layers of PD_A and PD_B were grown. For PD_A, the predicted bandwidth and saturation performance are 247.2 GHz and 101.6 mA, respectively. For PD_B, the predicted bandwidth and saturation performance are 295.3 GHz and 113.4 mA, respectively. The benefit of the proposed graded bandgap absorption layer is further verified. The saturation current is enhanced due to the inserted cliff layer. Moreover, the major fabrication process includes p-type contact metalization, p-mesa

formation, n-type contact metalization, n-mesa formation, passivation, planarization and deposition of GSG contact pads.

6.2 Future work

Our future work is to complete the post process of the designed UTC-PDs. Then, the measurements aim at various figures of merit, such as bandwidth, output power and responsivity, will be carried out. Thereby, the effects of the proposed graded bandgap absorption layer can be further verified. Moreover, the packaging techniques, such as flip-chip bonding technology which can improve the thermal management capability, will be investigated. Furthermore, the CPW-like interconnection structure will be investigated and designed. Because, at such high operating frequency, the interconnection line may cause great loss.

References

[1] A. Beling, "Periodic Travelling Wave Photodetectors with Serial and Parallel Optical Feed Based on InP," Ph. D. Dissertation, 2006.

[2] G.-F. D. Betta, "Advances in Photodiodes," InTech, chap. 14, pp. 302, 2011.

[3] H. Yang, et al., "High-speed and high-power InGaAs/InP photodiode," 23rd Intern. Conf. On Indium Phosphide and Related Materials, Berlin, Germany, May 2011.

[4] K. Kato, S. Hata, K. Kawano, and A. Kozen, "Design of Ultrawide-Band, High-Sensitivity p-i-n Photodetectors," IEICE Trans. Electron., vol. E76-C, no. 2, pp. 214-221, Feb. 1993.

[5] X. Li, et al., "High-saturation-current InP-InGaAs photodiode with partially depleted absorber," IEEE Photon. Technol. Lett., vol. 15, no. 9, pp. 1276-1278, Sep. 2003.

[6] T. Ishibashi, et al., "InP/InGaAs Uni-traveling-carrier Photodiodes," IEICE Trans. Electron, vol. E83-C, pp. 938-949, Jun. 2000.

[7] T. Ishibashi, S. Kodoma, N. Shimizu, and T. Furuta, "High-speed response of uni-traveling-carrier photodiodes," Jpn. J. Appl. Phys. 36, part 1, no. 10, pp. 6263-6268, 1997.

[8] T. Ishibashi, et al., "Uni-traveling-carrier photodiodes," Ultrafast Electronics

Optoelectronics OSA Spring Topical Meeting, Technical Digest, pp. 166-168, 1997.

[9] H. Ito, et al., “High-speed and high-output InP-InGaAs unitraveling-carrier photodiodes,” IEEE J. Sel. Top. Quantum Electron. 10(4), 709-727, 2004.

[10] B. Banik, J. Vukusic, H. Hjelmgren and J. Stake, “Optimization of the UTC-PD Epitaxy for Photomixing at 340 GHz,” Int J Infrared Milli Waves, pp. 914-923, 2008.

[11] H. Ito, T. Furuta, S. Kodama, N. Watanabe, and T. Ishibashi, “InP/InGaAs uni-travelling-carrier photodiode with 310 GHz bandwidth,” Electron. Lett., vol. 36, no. 21, pp. 1809-1810, Oct. 2000.

[12] N. Shimizu, N. Watanabe, T. Furuta, and T. Ishibashi, “InP-InGaAs Uni-Traveling-Carrier Photodiode With Improved 3-dB Bandwidth of Over 150 GHz,” IEEE Photonics Technology Letters, vol. 10, no. 3, Mar. 1998.

[13] D.-H. Jun, J.-H. Jang, I. Adesida, and J.-I. Song, “Improved efficiency bandwidth product of modified unitraveling carrier photodiode structures using an undoped photo-absorption layer,” Jpn. J. Appl. Phys. 45(4B), pp. 3475-3478, 2006.

[14] X. Wang, N. Duan, H. Chen, and J. C. Campbell, “InGaAs-InP photodiodes with high responsivity and high saturation power,” IEEE Photon. Technol. Lett. 19(16), pp. 1272-1274, 2007.

[15] M. Chtioui, F. Lelarge, A. Enard, F. Pommereau, D. Carpentier, A. Marceaux, F.

van Dijk, and M. Achouche, “High responsivity and high power UTC and MUTC GaInAs-InP photodiodes,” IEEE Photon. Technol. Lett. 24(4), pp. 318-320, 2012.

[16] Z. Li, H. Pan, H. Chen, A. Beling, and J. C. Campbell, “High-saturation-current modified uni-traveling-carrier photodiode with cliff layer,” IEEE J. Quantum Electron. 46(5), pp. 626-632, 2010.

[17] M. Chtioui, A. Enard, D. Carpentier, S. Bernard, B. Rousseau, F. Lelarge, F. Pommereau, and M. Achouche, “High-performance uni-traveling-carrier photodiodes with a new collector design,” IEEE Photon. Technol. Lett. 20(13), pp. 1163-1165, 2008.

[18] J.-W. Shi, Y.-S. Wu, C.-Y. Wu, P.-H. Chiu, and C.-C. Hong, “High-speed, high-responsivity, and high-power performance of near-ballistic uni-traveling-carrier photodiode at 1.55-μm wavelength,” IEEE Photon. Technol. Lett. 17(9), pp. 1929-1931, 2005.

[19] J.-W. Shi, F.-M. Kuo, and J. E. Bowers, “Design and analysis of ultra-high-speed near-ballistic uni-travelingcarrier photodiodes under a 50-Ω load for high-power performance,” IEEE Photon. Technol. Lett. 24(7), pp. 533-535, 2012.

[20] H. Fukano, Y. Muramoto, K. Takahata, and Y. Matsuoka, “High efficiency edge-illuminated uni-travelling-carrier-structure refracting-facet photodiode,”

Electronics Letters 35(19), pp. 1664-1665, 1999.

[21] S. Demiguel, N. Li, X. Li, X. Zheng, J. Kim, J. C. Campbell, H. Lu, and A. Anselm, "Very high-responsivity evanescently coupled photodiodes integrating a short planar multimode waveguide for high-speed applications," IEEE Photon. Technol. Lett. 15(12), pp. 1761-1763, 2003.

[22] J. Klamkin, S. M. Madison, D. C. Oakley, A. Napoleone, F. J. O'Donnell, M. Sheehan, L. J. Missaggia, J. M. Caissie, J. J. Plant, and P. W. Juodawlkis, "Uni-traveling-carrier variable confinement waveguide photodiodes," Opt. Express 19(11), pp. 10199-10205, 2011.

[23] M. Hosseinifar, V. Ahmadi, and G. Abaeiani, "Microring-based unitraveling carrier photodiodes for high bandwidth-efficiency product photodetection in optical communication," J. Lightwave Technol. 29(9), pp. 1285-1292, 2011.

[24] Y. Muramoto, K. Kato, M. Mitsuhara, O. Nakajima, Y. Matsuoka, N. Shimizu and T. Ishibashi, "High-output-voltage, high speed, high efficiency uni-travelling-carrier waveguide photodiode," Electronics Letters, vol. 34, no. 1, 8th Jan. 1998.

[25] N. Duan, X. Wang, N. Li, H. D. Liu, and J. C. Campbell, "Thermal analysis of high-power InGaAs-InP photodiodes," IEEE J. Quantum Electron., vol. 42, no. 12, pp. 1255-1258, Dec. 2006.

[26] Z. Li, et al., "High-power high-linearity flip-chip bonded modified uni-traveling carrier photodiode," Opt. Express, vol. 19, no. 26, pp. B385-B390, 2011.

[27] Q. Zhou, A. Cross, Y. Fu, A. Beling, and J. C. Campbell, "High-power high-bandwidth flip-chip bonded modified uni-traveling carrier photodiodes," Proc. IEEE Photon. Conf., pp. 306-307, Sep. 2012.

[28] J.-W. Shi, F.-M. Kuo, C.-J. Wu, C. L. Chang, C.-Y. Liu, C. Y. Chen, and J.-I. Chyi, "Extremely high saturation current-bandwidth product performance of a near-ballistic uni-traveling-carrier photodiode with a flip-chip bonding structure," IEEE J. Quantum Electron. 46(1), pp. 80-86, 2010.

[29] H. Ito, T. Furuta, S. Kodama, N. Watanabe, and T. Ishibashi, "InP/InGaAs uni-travelling-carrier photodiode with 220 GHz bandwidth," Electron. Lett., vol. 35, pp. 1556-1557, Sep. 1999.

[30] "ATLAS User's Manual," SILVACO Inc., Santa Clara, Mar. 2012.

[31] S. M. Mahmudur Rahman, H. Hjelmgren, J. Vukusic, J. Stake, P. A. Andrekson, and H. Zirath, "Hydrodynamic simulations of unitraveling-carrier photodiodes," IEEE J. Quantum Electron., vol. 43, no. 11, pp. 1088-1094, Nov. 2007.

[32] http://www.ioffe.rssi.ru/SVA/NSM/.

[33] S. Adachi, "Physical Properties of III-V Semiconductor Compounds: InP, InAs,

GaAs, GaP, InGaAs and InGaAsP, Wiley Interscience," John Wiley and Sons, 1992.

[34] S. Srivastava, "Simulation study of InP-based uni-traveling carrier photodiode," Master Thesis, University of Cincinnati, 2003.

[35] http://en.wikipedia.org/wiki/Refractive_index.

[36] S. Adachi, "Optical Constants of Crystalline and Amorphous Semiconductors," Kluwer Academic Publishers, Boston, pp. 359-362, 1999.

[37] M. Levinshtein, S. Rumyantsev, M. Shur, "Handbook Series on Semiconductor Parameters," World Scientific, New Jersey, Chap. 7, pp. 156, 1999.

[38] R. Stratton, "Diffusion of hot and cold electrons in semiconductor barriers," Phys. Rev. 126(6), pp. 2002-2014, 1962.

[39] R. Stratton, "Semiconductor current-flow equations (diffusion and degeneracy)," IEEE Trans. Electron. Dev. 19(12), pp. 1288-1292, 1972.

[40] M. Shur, "Physics of Semiconductor Devices," Prentice Hall, New Jersey, pp. 74, 1990.

[41] Caughey, D.M., and R.E. Thomas, "Carrier Mobilities in Silicon Empirically Related to Doping and Field," Proc. IEEE 55, pp. 2192-2193, 1967.

[42] M. M Tashima, L.W Cook, and G.E Stillman, "Room temperature electron diffusion lengths in liquid phase epitaxial InGaAsP and InGaAs," Appl. Phys. Letters, vol. 39,

pp. 960-961, 1981.

[43] T. Conklin, S. Naugle, S. Shi, K.P. Roenker, S.M Frimel, T. Kumar, M.M Cahay, "Inclusion of tunneling and ballistic transport effects in an analytical approach to modeling of NPN InP based heterojunction bipolar transistors," Superlatt. Microstruct., vol. 18, pp. 1-12, 1996.

[44] Dziewior J. and W. Schmid, "Auger Coefficient for Highly Doped and Highly Excited Silicon," Appl. Phys. Lett. vol. 31, pp. 346-348, 1977.

[45] R. Zhang, B. Hraimel, X. Li, P. Zhang, and X.-P. Zhang, "Design of broadband and high-output power uni-traveling-carrier photodiodes," Optics Express, vol. 21, no. 6, 2013.

[46] T. P. Pearsall, "GaInAsP Alloy Semiconductors," John Wiley and Sons, 1982.

[47] S. O. Kasap, "Optoelectronics and Photonics: Principles and Practices," Prentice Hall, pp. 222, 2001.

[48] P. Liu, K. J. Willaims, M. Y. Frankel, and R. D. Esman, "Saturation Characteristics of Fast Photodetectors," IEEE Trans. on Microwave Theory and Tech., vol. 47, no. 7, pp. 1297-1303, 1999.

[49] K. J. Williams and R. D. Esman, "Design considerations for high-current photodetectors," J. Lightwave Technol., vol. 17, pp. 1443-1454, Aug. 1999.

[50] W. Fawcett and G. Hill, “Temperature dependence of the velocity/field characteristic of electrons in InP,” Electron. Lett., vol. 11, no. 4, pp. 80-81, Feb. 1975.

[51] N. Li, X. Li, S. Demiguel, X. Zheng, J. Campbell, D. Tulchinsky, J. Williams, T. Isshiki, G. Kinsey, and R. Sudharsansan, “High-saturation-current charge-compensated InGaAs-InP UTC photodiode,” IEEE Photon. Technol. Lett., vol. 16, no. 3, pp. 864-866, Mar. 2004.

[52] D. A. Anderson, N. Aspley, P. Davies, and P. L. Giles, “Compensation in heavily doped n-type InP and GaAs,” J. Appl. Phys., vol. 58, no. 8, pp. 3060-3067, 1985.

[53] T. J. Maloney and J. Frey, “Transient and steady-state electron transport properties of GaAs and InP,” J. Appl. Phys., vol. 48, no. 2, pp. 781-787, 1977.

[54] M. Chtioui, et al., “High Power UTC Photodiodes Design and Application for Analog Fiber Optic Links,” Proc. IEEE Int. Topical Meeting Microwave Photonics, pp. 1-4, 2009.

[55] R. C. Jaeger, “Introduction to Microelectronic Fabrication,” 2nd edition, Prentice Hall, pp. 156, 2002.

[56] D. A. Neamen, “Semiconductor Physics and Devices: Basic Principles,” 3rd edition, McGrdw-Hill, pp. 348, 2003.